Mesospheric winds above the South Island of New Zealand

A THESIS
SUBMITTED IN PARTIAL FULFILMENT
OF THE REQUIREMENTS FOR THE DEGREE
OF
DOCTOR OF PHILOSOPHY IN PHYSICS
IN THE
UNIVERSITY OF CANTERBURY

by
Manfred Plagmann

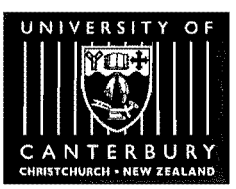

University of Canterbury
1999

To my mother
and my grandmother Taline

Abstract

This project involved the comparison of horizontal winds from three different techniques in the upper mesosphere, lower thermosphere region at 80-105 km and the characterization of the ability of the Fabry-Perot technique to observe gravity waves in the airlow layers. The wind measurements for the comparison were obtained by three independent ground-based techniques, a meteor radar (MR) , a medium frequency radar (MF) and an optical Fabry-Perot spectrometer (FPS). All three instruments are located on the South Island of New Zealand.

The optical winds were derived from night-time observations of the Doppler shifts in the mesospheric 840 nm hydroxyl emission near 87 km and the lower thermospheric 557.7 nm atomic oxygen emission at about 95 km height. The radar winds were obtained using a partial reflection medium frequency radar operating at 2.4 MHz and a meteor radar operating at 26.2 MHz with a pulse repetion rate of 379 Hz.

The initial comparisons were made for 5 consecutive nights during May 1997. As a consequence of the results obtained the comparison of the FPS/MR combination were extended to 80 nights in the period encompassing May 1997 to April 1998. Dates considered suitable were those exhibiting no cloud and low magnetic activity.

A very good correlation was observed between the FPS and MR winds for the 5 consecutive days and, albeit to a lesser degree, in the complete data set of 80 days. The good correlation between the FPS and the MR was used to determine the monthly mean height of the hydroxyl and the atomic oxygen layer over the period between May 1997 to April 1998. The result shows an annual variation in the height of the hydroxyl layer with the lower height during early summer and little variation in the height of the atomic oxygen layer.

The study of the detectability of the gravity waves in the FPS wind measurements reveals that waves from the part of the gravity wave spectrum which shows the most activity can only, if at all, be detected with a strongly attenuated amplitude. With knowledge of the gravity wave detectability of the FPS, signatures of very long wavelength gravity waves were sought in the available data set. On many nights signatures of wave activity which could be related to gravity waves were found. The attempt to use the MR data set to aid in the determination of the wavelength of those waves was of limited success.

Contents

List of Figures

Chapter 1

Introduction

The first few kilometers of the Earth's atmosphere to a height of approximately 10 km is called the troposphere. This part of the atmosphere enables us to experience the atmosphere's variability though the weather phenomena and has therefore a strong impact on our life. This impact makes many think that this region of the atmosphere is the most important. Recent research shows that due to transport mechanisms, the atmospheric layers can not be treated as independent entities which build the earth's atmosphere but the atmosphere has to be seen as a whole. Weather conditions, for example, in the troposphere can influence the temperature at a height of 100 km in the mesopause which in turn drives global circulation air masses to the other side of the Earth. It is therefore important to understand the whole atmosphere, that means parts which at first glance seem not to be connected.

Computer models which simulate the atmosphere to obtain an understanding of its behaviour rely on measured data obtained from various instruments. The reliability of these data sets is important and comparison between different measurement techniques can reveal biases of the instruments used. It is also important to know the observational limits of the instruments used to

measure various parameters of the atmosphere to decide whether the absence of a feature is due to its absence in the atmosphere or that it just can not be detected by the instrument in use.

This project involved the comparison of horizontal winds in the upper mesosphere, lower thermosphere region by means of three independent ground-based wind measurement techniques. All instruments are located in the South Island of New Zealand. The meteor radar and the medium frequency radar are operating at Birdlings Flat (43°49'S, 172°41'E) near Christchurch while the optical Fabry-Perot spectrometer operates at Mt.John observatory (43°59'S, 170°28'E) near Lake Tekapo.

The optical winds were simultaneously derived from night-time observations of the hydroxyl airglow emission at 840 nm in the mesopause (at about 87 km) and the atomic oxygen emission at 577.7 nm in the lower thermosphere near 95 km in height. Clear night data from days with low magnetic activity (low K_p) during the period encompassing May 1997 to April 1998 were used and compared with data simultaneously obtained from the medium frequency radar and the meteor radar. The comparison was restricted to the meridional wind component as the meteor radar can, in the current setup, only measure winds in this direction

Although the comparison between the meteor radar wind and the optical Fabry-Perot spectrometer wind was good the variability of the nightly data sets were remarkably different. The distinctiveness of the sampling volumes of both instruments could not account for the differences as the numerical variances would be expected to be about equal. Part of the differences must therefore arise from differences in the observation methods employed. This difference led to an investigation of its cause by establishing the observational limits of short period waves by the Fabry-Perot spectrometer. This

investigation comes to the conclusion that short period waves with vertical wavelengths less than about 22 km are not detectable due to the width of the airglow layers and the integration time of the Fabry-Perot spectrometer.

With the knowledge of the detectability of waves by the Fabry-perot spectrometer the data set was scanned to find signatures of waves which should be detectable. Many nights were found which revealed long periodic waves with horizontal wavelengths of about 2000 km and vertical wavelengths near 50 km.

This thesis will give in the following section a short introduction into the structure of the atmosphere. Thereafter the brief description of tides (Section 2.1) and gravity waves (Section 2.2) will introduce these two important aspects of the dynamics of the atmosphere. The chemical reactions behind the night-time airglow will be discussed in Section 2.3. Chapter 3 will introduce the theory of Fabry-Perot interferometry and describe the experimental setup of the Fabry-Perot spectrometer located at Mt. John Observatory. The Data reduction with two fitting techniques is described in Chapter 4. A brief introduction into the meteor radar and medium frequency radar technique (Chapter 5) will close the introductory part of this thesis. Chapter 6 will present the results of the intercomparision of wind measurements in the mesopause, lower thermosphere region using a meteor radar, a medium frequency radar, and an optical Fabry-Perot spectrometer. The gravity wave detectability using the Fabry-Perot spectromery is described in Chapter 7.

1.1 General Characteristic of the Atmosphere

The vertical structure of the atmosphere can be divided into layers using the different physical conditions of the atmosphere. Temperature structure is often used: At mid latitudes the positive lapse rate in the *troposphere* results in a local temperature minimum at the *tropopause*. In the *stratosphere* the temperature again increases with altitude and the stratosphere is therefore an inversion layer with a local temperature maximum at the *stratopause*. Such an inversion layer is very stable against vertical mixing as the cooler, denser air is below the warmer air. Above the stratopause is the *mesosphere*

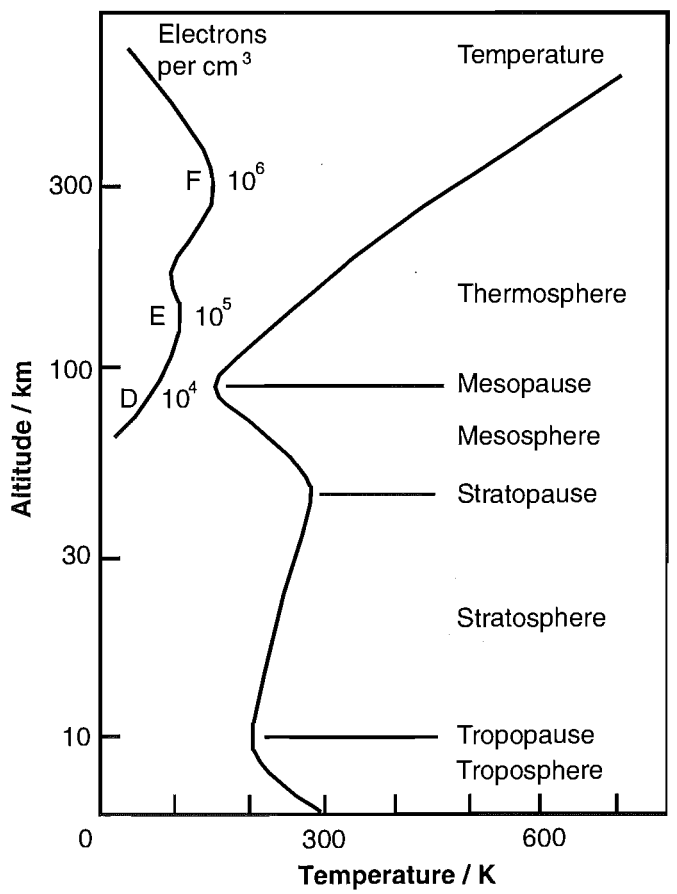

Figure 1.1: Temperature and electron density profile of the atmosphere. Adapted from (McEvan & Phillips 1975)

where the temperature decreases to a second minimum at the *mesopause*, the coldest area in the atmosphere. Above, in the *thermosphere*, the temperature increases and reaches kinetic temperatures of about 1500-2000 K.

Figure 1.1 shows the vertical temperature profile as well as the electron density, another property of the atmosphere which can be used for characterisation. The electron layer is called the ionosphere which is divided into the D, E and F regions according to the electron density. These layers obtain their ions from the photoionizing radiation of the sun. In particular the vacuum ultraviolet radiation ionizes the molecular oxygen and other minor particles above about 100 km.

According to another physical condition the atmosphere is divided into just two layers. The *homosphere*, where the bulk composition of the atmosphere is practically the same as at sea level and the layer above, the *heterosphere*. The composition of the homosphere is dominated by mixing rather than diffusion while in the heterosphere diffusion plays the more important role. The boundary between homosphere and heterosphere lies between about 80-110 km in height. This region contains reactive molecules due to photoionization such as OH, NO, and O_3 etc. which results in the production of the night-time airglow layers (see Section 2.3).

The temperature and electron density profiles shown in Fig. 1.1 reflect the global average situation, the actual structure might be very different due to winds and local and/or temporal temperature changes.

Chapter 2

The Dynamic Atmosphere

One of the most important properties of the atmosphere is its ability to support wave motions. Waves are excited when air is disturbed from equilibrium. Restoring forces drive the displaced air parcels back in the direction they came to restore equilibrium. Both excitation and restoring forces are necessary effects for the existence of waves. Such waves are usually characterised by their restoring mechanism. Other classifications distinguish *forced* and *free* waves, where the former must continually be maintained by an excitation mechanism while the later are not so maintained. Waves can also be separated into *stationary* waves, whose surfaces of constant phase are fixed with respect to the earth, and *travelling* waves, whose phase surfaces move. In this introduction only those waves which are of importance to this thesis will be considered.

At first an elementary introduction to atmospheric tides is given in section 2.1. Tides, especially the semi-diurnal tide at mid-latitudes, are the strongest wave components in the atmospheric motion at mesospheric heights. The Fabry-Perot spectrometer, which is used in this thesis as the main source of atmospheric data, is an excellent tool for studying atmospheric tides.

Gravity wave theory has been described by Hines (1960). They are driven by buoyancy and owe their existance to atmospheric stratification and are described in Section 2.2. These waves are ubiquitous in the atmosphere between the troposphere and mesopause. Their sources lie generally in the troposphere, for example frontal systems (Freund & Jacka 1979, Taylor & Hapgood 1988) or mountain ranges (Gerbier & Berenger 1961). These waves are important as they drive the general circulation of the middle atmosphere. This thesis investigates the detectability of those important waves with the technique of the optical Fabry-Perot spectrometry.

It is beyond the scope of this thesis to describe dynamics in full detail. For a detailed describtion of the atmospheric dynamics the reader may consult the primary literature written by authors such as Holton (1992), Andrews et al. (1987), or Salby (1996).

2.1 Tides

Atmospheric tides are global-scale daily oscillations, which are primarily forced by diurnal variations of the heating due to the absorption of solar ultraviolet radiation by atmospheric water vapor and ozone. Of particular interest here are the migrating tides which move with the sun. As the Earth rotates, the sun appears to move westwards and, as a consequence, so does the perturbation region of maximum heating. The period of the oscillation is the same as the forcing and as the perturbation moves the tides produced are called migrating tides.

The solar heating cycle is diurnal (see Figure 2.1) and the perturbation function has the form of a truncated sinusoid. As a result, harmonics with periods of 12, 8, 6 hours etc. also occur. The Fourier components of the perturbation

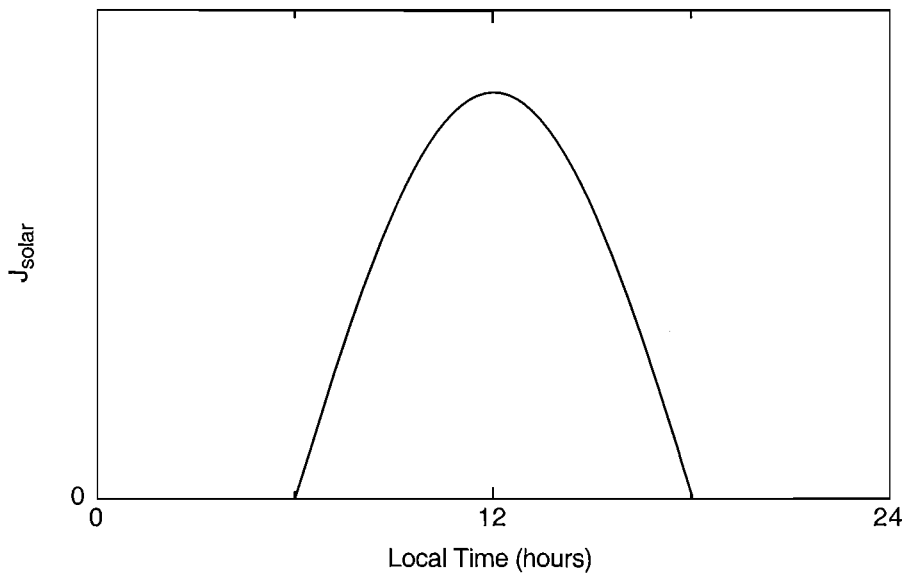

Figure 2.1: Schematic diagram of the typical daily variation of the solar heating J_{solar} (after Andrews et al. (1987))

function show that the semidiurnal component (12-hr period) has a somewhat smaller amplitude than the diurnal component (24-hr period). The response of the atmosphere to this heating reveals, however, a larger and more regular semidiurnal oscillation. This behaviour expresses the fact that only certain modes of oscillation are generated in preference. These are the modes with antinodes at the equator as the heating rate is the greatest here. The peak of the number density of the ozone layer is centered at about 30 km with a full width at half maximum (FWHM) of about 20 km. This broad height range of the ozone excitation region causes short vertical wavelength modes ($\lambda_z \sim 30 - 40$ km) to experience destructive interference. Tidal modes with large vertical wavelengths ($\lambda_z \sim 100$ km) are therefore excited preferentially. Forbes (1982) showed that these observed modes are associated with the majority of the ozone and water vapour heating.

In the mid-latitude mesopause, lower thermosphere region amplitudes of the semi-diurnal tide of typically 15-30 ms^{-1} were measured (Chapman &

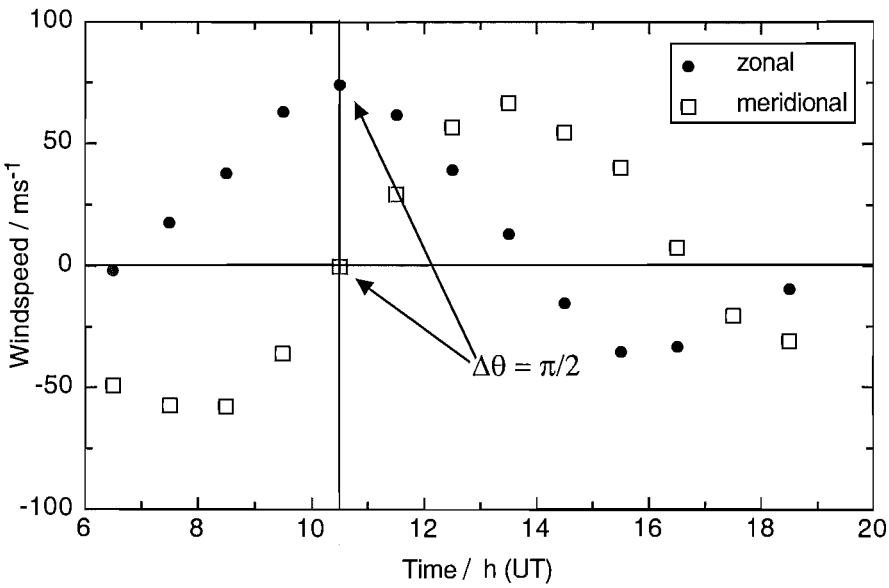

Figure 2.2: The zonal (dots) and meridional (open squares) Fabry Perot spectrometer wind data from the atomic oxygen emission for 2 May 1997. The phase difference between both directions is $\pi/2$, which indicates a semidiurnal tide.

Lindzen 1970, Smith 1981, Manson et al. 1985, Manney et al. 1989). Figure 2.2 shows as an example Fabry-Perot spectrometer wind data of the zonal (dots) and the meridional (open squares) component. It can be seen that maximum amplitude of the meridional component is three hours behind the maximum of the zonal component. This indicates a semi-diurnal wave which rotates by $\pi/2$ radians in three hours. The wind vector obtained by a combination of zonal and meridional wind rotates at a given height counterclockwise with increasing time. A single upwardly propagating semidiurnal tidal mode will exhibit a constant change in phase, with the time of maximum wind decreasing with increasing height. Viewed from above this results in a wind vector which rotates clockwise with height at a given time. However, with a number of modes present, each with a different vertical wavelength, the vertical tidal behaviour will be rather complicated and the sense of rotation with height may even reverse.

2.2 Gravity Waves

As mentioned earlier gravity waves are buoyancy oscillations in density, wind velocity and temperature, etc. that occur and propagate in the Earth's atmosphere. Gravity waves of comparatively small scale between tens to hundreds of kilometers in horizontal wavelength appear to be common in the upper mesopshere where they have been detected by radars and other instruments. The periods of these waves typically range from a few minutes to an hour or so (Andrews et al. 1987).

A parcel of air, vertically displaced in a horizontally stratified atmosphere will oscillate. The restoring forces are provided by the buoyancy of the parcel and the gravity. When the restoring forces are entirely due to buoyancy and gravity the waves are called pure internal gravity waves. The waves are called inertio-gravity waves in the case where the restoring force is a combination of buoyancy, gravity, and Coriolis force. The Coriolis force only affects gravity waves with horizontal scales greater than a few hunderd kilometers and periods greater than a few hours. In practice, the restoring force is a combination of buoyancy, the pressure change due to the compression of the medium and the Coriolis force due to the rotating Earth and the gravity due to the mass of the air parcel.

Since gravity waves involve motion transverse to the propagation vector $\vec{k}$, they require two dimensions to be described. The air motion in the x-z plane can be described by

$$\frac{Du}{Dt} = -\frac{1}{\rho}\frac{\partial p}{\partial x} \tag{2.1}$$

$$\frac{Dw}{Dt} = -\frac{1}{\rho}\frac{\partial p}{\partial z} - g \tag{2.2}$$

$$\frac{1}{\rho}\frac{D\rho}{Dt} + \frac{\partial u}{\partial x} + \frac{\partial w}{\partial z} = 0 \tag{2.3}$$

$$\frac{D \ln p}{Dt} - \gamma \frac{D \ln \rho}{Dt} = 0 \tag{2.4}$$

where $D/Dt = \partial/\partial t + u\partial/\partial x + w\partial/\partial z$ with u the wind speed in x direction (horizontal) and w the wind speed in z direction (vertical). Equations 2.1, 2.2 describe the acceleration of the wind due to the pressure gradient and the gravitational force g. ρ is the density of the air and p its pressure. These equations account for compressibility if $D\rho/Dt$ is not set to 0 in the continuity equation 2.3 and they will therefore also describe acoustic waves. Equation 2.4 is the thermodynamic energy equation for adiabatic motion. $\gamma = c_p/c_v$ is the ratio of the specific heat capacity at constant pressure c_p and the specific heat capacity at constant volume c_v.

Waves can be considered as perturbations of a constant basic state of the atmosphere. The dependent variables of the equation system such as (Equation 2.1-2.4) can then be divided into the constant basic state portions (in the following denoted by overbars) which are usually assumed to be independent of time and longitude, and the perturbation portions (denoted by primes), which are the local deviation of the field from the basic state. The zonal velocity u, for example, can then be divided into the time- and longitude-averaged zonal velocity $\bar{u}$ and u' the deviation from that average. The dependent variables of the equation system 2.1-2.4 can therefore be rewritten as

$$\begin{aligned} u(x,t) &= \bar{u} + u'(x,t) \\ w(x,t) &= \bar{w} + w'(x,t) \end{aligned} \tag{2.5}$$

$$
\begin{aligned}
p(x,t) &= \bar{p} + p'(x,t) \\
\rho(x,t) &= \bar{\rho} + \rho'(x,t)
\end{aligned}
\tag{2.6}
$$

Using this linear perturbation theory (see eg. Holton (1992)) and substituting Equation 2.6 into Equations 2.1-2.4, assuming an isothermal atmosphere with uniform motion and in hydrostatic equilibrium the perturbation equations become,

$$\frac{Du'}{Dt} = -gH\frac{\partial \hat{p}'}{\partial x} \tag{2.7}$$

$$\frac{Dw'}{Dt} = -gH\frac{\partial \hat{p}'}{\partial z} + g\hat{p}' - g\hat{\rho}' \tag{2.8}$$

$$\frac{D\hat{\rho}'}{Dt} + \frac{\partial u'}{\partial x} + \frac{\partial w'}{\partial z} - \frac{w'}{H} = 0 \tag{2.9}$$

$$\frac{D(\hat{p}' - \gamma\hat{\rho}')}{Dt} + \gamma\frac{N^2}{g}w' = 0 \tag{2.10}$$

where

$$\hat{p}' = \frac{p'}{\bar{p}}, \quad \hat{\rho}' = \frac{\rho'}{\bar{\rho}} \tag{2.11}$$

and H, the scale height is defined as

$$H = \frac{RT}{g} \tag{2.12}$$

with R the gas constant, T the temperature in Kelvin, and g the gravity force.

N defines the natural frequency of oscillation in the Earth's atmosphere which is the upper-frequency limit for buoyancy oscillations. It is called the Brunt-Vaisala frequency. This frequency is determined by

$$N^2 = g\frac{\partial \ln \theta}{\partial z} \tag{2.13}$$

where g the acceleration due to gravity and

$$\theta = T(p/p_s)^{R/c_p} \tag{2.14}$$

θ is the potential temperature which is the temperature that a parcel of dry air at a pressure p and a temperature T would have if it were expanded or compressed adiabatically to a standard pressure p_s, R is the gas constant, T is the temperature, and c_p is the specific heat at constant pressure. In the mesopause, lower thermosphere region the Brunt-Vaisala frequency corresponds to an oscillation period of about 5 minutes.

Equations 2.7-2.10 constitute a closed system for the four unknowns: u', w', $\hat{p}'$, and $\hat{\rho}'$. Because this equation system has constant coefficients, solutions can be expressed in terms of plane waves. However, due to the stratification of mass a wave which propagates vertically must essentially adjust its amplitude to conserve wave action. For quadratic quantities like the kinetic energy density $\bar{\rho}\bar{u'}$ to remain constant, u', w', $\hat{p}'$, and $\hat{\rho}'$ must amplify vertically like $\bar{\rho}^{-1/2} = exp[z/2H]$.

Solutions to the Equation system 2.7-2.10 can be written in the form

$$u' = u_0 exp(\frac{z}{2H}) exp[i(\omega t - kx - mz)] \tag{2.15}$$

where u_0 is a constant with dimension of velocity, z is the height in kilometers, H is the scale height in kilometers, and m and k are the vertical and horizontal components of the wavevector. Consolidating the equation system 2.7-2.10 yields the dispersion relation

$$m^2 = k^2 \left(\frac{N^2}{\omega^2} - 1 \right) + \frac{\omega^2 - \omega_a^2}{c_s^2} \tag{2.16}$$

where

$$c_s^2 = \gamma R \bar{T} \tag{2.17}$$

is the square of the speed of sound and ω_a is the acoustic cutoff frequency for vertical propagation and is given by

$$\omega_a = \frac{c_s}{2H} \tag{2.18}$$

Equation 2.16 describes acoustic-gravity waves, which involve buoyancy as well as compression. In the frame of this thesis, which deals with data obtained from an optical Fabry-Perot spectrometer, the acoustic branch of the dispersion relation can be neglected as the resulting waves have periods smaller than the integration time of the spectrometer. By letting $c_s \to 0$, which renders air motion incompressible, the dispersion relation reduces to

$$k^2 + m^2 + \frac{1}{4H^2} \cong \frac{N^2}{\omega^2} k^2 \tag{2.19}$$

and describes low-frequency gravity waves. As mentioned earlier internal gravity waves have a high-frequency cutoff for vertical propagation, the Brunt-Vaisala frequency N. In the short wave limit $k \to \infty$, the maximum ω for vertical propagation approaches N, while in the longwave limit $k \to 0$ the

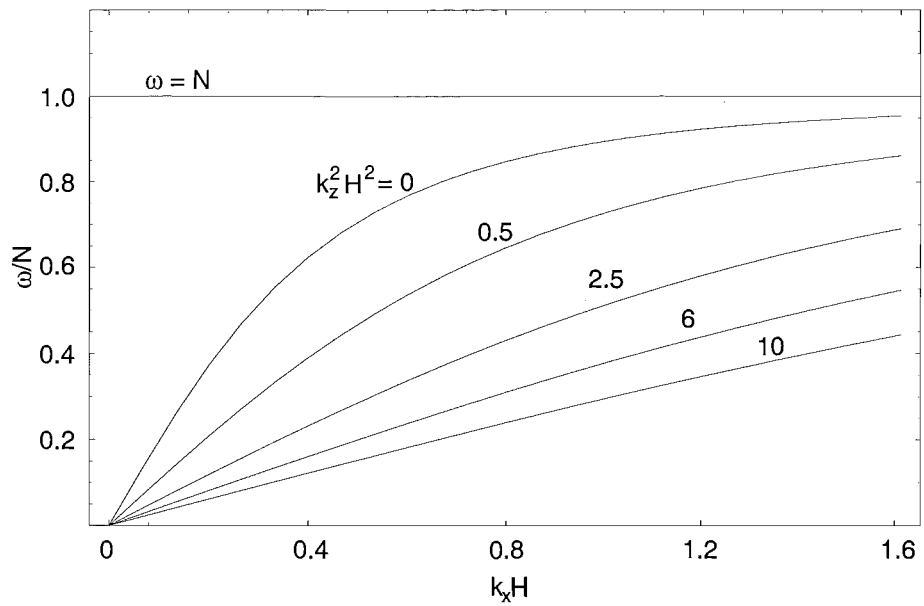

Figure 2.3: Nondimensional plot of the vertical wavenumber contoured as a function of horizontal wavenumber and intrinsic frequency. In the short wave limit $k \to \infty$, the maximum ω for vertical propagation approaches N, while in the longwave limit $k \to 0$ the maximum ω for vertical propagation approaches zero.

maximum ω for vertical propagation approaches zero. The latter waves have horizontal phase speeds approaching the speed of sound. Figure 2.3 shows solutions of the dispersion relation (Equation 2.19) for vertically propagating gravity waves, which lie lower than the curve for $k_z = 0$.

The spectral distribution of gravity waves in the atmosphere has been measured by means of many instruments e.g radars, lidars, all sky imagers (Vincent 1984, Smith et al. 1987, Senft et al. 1993). Data from these instruments show that although the amplitude of frequency spectra increases by a factor of 100 or more from the troposphere to the mesosphere (Balsley & Carter 1982, Balsley & Garello 1985) the power spectral density of vertical wavenumber spectra at large wavenumbers does not increase significantly over the same altitude range. Such a spectrum is called saturated.

Existing theories of gravity wave spectra invoke a variety of different phys-

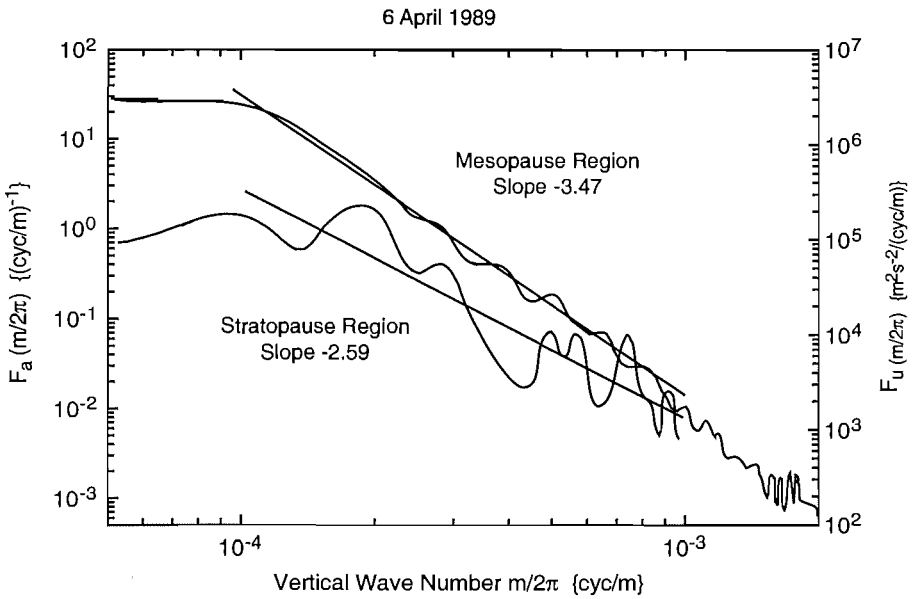

Figure 2.4: Vertical wave number power spectrum of the atmospheric density perturbation associated with internal gravity waves in th stratopause and mesopause regions. The spectra were inferred from Na lidar data collected at Arecibo on 6 April 1990. The straight lines are linear regression fits to the spectra for 1-10 km wavelengths. After Senft et al. (1993).

ical mechanisms for dissipating wave energy including shear and convective instabilities, wave-induced Doppler effects, and wave-induced diffusion. A detailed discussion of the leading wave dissipation paradigms is given by Gardner (1996). The Linear Instability Theory (LIT) paradigm, originally described by Dewan & Good (1986), the Doppler-Spread Theory by Hines (1991), and the Diffusive Filtering Theory paradigm, formulated by Gardner (Gardner 1994, Gardner 1995), are the most prominent theories. These models predict the same form and behaviour for the vertical wavenumber spectrum of horizontal winds. The spectrum (see Figure 2.4) is characterized by a vertical wavenumber that partitions the spectrum into a low wavenumber regime dominated by the gravity wave source characteristics, and a high wavenumber region dominated by saturation and dissipation processes. In the source region ($m<m_*$) the spectrum is proportional to m^s, where s is

between 1 and 2. In the so-called saturation region ($m>m_*$), the spectrum is proportional to N^2/m^3, where N is the buoyancy frequency. The characteristic vertical wavenumber m_* is proportional to N/u'_{rms} and decreases therefore with altitude as u'_{rms} increases. For the mesopause region the characteristic vertical wavelength $\lambda_z^* = 2\pi/m_*$ varies between about 10 and 16 km depending on the wave activity (Smith et al. 1987).

Previous workers (Manson et al. 1979, Richter et al. 1981, Vincent 1984, Meek et al. 1985, Senft et al. 1993) have reported mainly on the mean vertical wavelength and the mean amplitude, although some have reported on the wave spectrum of the wave activity found in the middle upper atmosphere. This paragraph will give an overview of the wave parameters measured by various authors. Manson et al. (1979) found a mean vertical wavelength $\lambda_z \sim$ 20km using a medium frequency radar in Saskatoon, Canada. Vincent (1984) measured a mean vertical wavelength λ_z of 12 km with a mean amplitude u'_{rms} of 30 ms^{-1}. With a medium frequency radar in Adelaide, Australia, he found that a large fraction of the energy flux is carried by short period (<1h) waves. Vertical wavelengths λ_z between 3 and 15 km and phase speeds c of 0.5-3 ms^{-1} were reported by Richter (Richter et al. 1981) using a lidar. Using a lidar (during the AIDA-89 campaign) Senft et al. (1993) measured a mean vertical wavelength λ_z of 6.2 km and an amplitude u'_{rms} of 28 ms^{-1}. The mean characteristic wavelength $\bar{\lambda}_z^*$, which defines the breakpoint in the spectrum between the weak and strong wave interaction subranges, was for example measured to be 14.3 km (Senft et al. 1993) which lies well within the interval of 10 to 16 km assumed in the gravity wave model by Gardner (1998). According to a model after Smith et al. (1987) most gravity wave energy lies within a factor of 3 around 1.26 λ_z^* (see Figure 7.10). This corresponds well with the findings of Vincent (1984) who observed that the most energy was transported in waves with wavelength λ_z between 10 and 20 km. Meek

et al. (1985) measured the horizontal scale of gravity waves and their phase speeds above Saskatchewan, Canada, and found the distributions shown in Figure 7.11. Similar results were reported by Giers et al. (1997). They found that waves with a horizontal wavelength of less than 120 km make up about 80% of the measured wave activity and that the observed horizontal phase speeds are centered at about 50 ms^{-1}. This is confirmed by Vincent (1984) who calculated the horizontal phase speed to be around 40 ms^{-1}.

The impact of gravity wave propagation upon airglow layers, especially the OH and OI layers, has been investigated by several authors (eg. (Noxon 1978, Frederick 1979, Hatfield et al. 1981, Gardner & Shelton 1985, Hines & Tarasick 1987, Walterscheid & Schubert 1987, Tarasick & Hines 1990)). Frederick (1979) showed that atomic oxygen density variations in the mesopause, lower thermosphere region, of up to 10 km in the vertical direction, are possible under the influence of gravity waves with horizontal wavelength of 200 km and vertical wavelength of 20 km. Similar findings with regard to vertical emision profile variations were reported by Hatfield et al. (1981) and Gardner & Shelton (1985) who investigated gravity wave effects on OH night airglow and neutral sodium layer emission intensities, respectively.

Tides and gravity waves are important dynamic features of the atmosphere. They are a substantial part of the atmosphere's energy budget in the mesosphere and lower thermosphere. Gravity waves are, for example, responsible for the warm winter mesopause as they drive an air circulation which brings the warm air from the summer hemisphere to the winter hemisphere or they have an influence in the photochemistry of the airglow layers. It will be shown later (Chapter 7) that the Fabry-Perot spectrometer used for the data aquisition of this thesis is unable to detect a certain part of the gravity wave spectrum. This inability, however, makes the instrument an excellent tool to measure the tidal dynamics in the mesopause, lower thermosphere region.

2.3 The Airglow

The most prominent optical emission from the terrestrial atmosphere is the *aurora* which can sometimes be seen with the unaided eye during night-time in the southern (aurora australis) and the northern hemisphere (auroa borealis) at high latitudes around the geomagnetic poles. In contrast to this spectacular looking and irregular *aurora*, *airglow* occurs continuously and is extremly weak (invisible to the eye), and is not confined to a region around the geomagnetic poles. This weak emission can be used to determine wind speed, wind direction, and temperatures in the so called airglow layers.

This chapter briefly descibes the airglow excitation and emission mechanism which is relevant to this work.

The atmosphere radiates at a wide variety of frequencies due to excitation and relaxation processes of atmospheric species such as N_2, N_2^+, O_2, O, N, H and OH. This work uses the airglow emission of the atomic oxygen O(^{1}S) (557.7 nm) and the $P_1(2)$ branch of the excited OH(6-2) transition (840 nm) to determine wind speed and temperatures at the heights of these emission layers. Two atomic oxygen emission layers can be found in the atmosphere (see Figure 2.5) although only the one in the lower thermosphere (about 95 km (Thomas & Young 1981)) is of interest here. The second layer contributes very little emission and does not usually contaminate the measurements. At high latitudes, however, during high geomagnatic activity the emission of this thermospheric layer can reach intensities which influence the data obtained (Chamberlain 1961). This increase in intensity is also observable at mid-latitudes (Hargreaves 1992). As a consequence only data obtained during geomagnetic quiet times ($K_p <= 3$) can be used (see Chapter 4).

The height and vertical structure of airglow layers have been measured by

λ (nm)	Emitting Species	Intensity (Rayleighs)	Height (km)
557.7	$O(^1S)$	250 R	90, 300
589.3	$Na(^2P)$	20-150 R	$\approx$92
630, 636.4	$O(^1D)$	10-500 R	300
761.9	$O_2(b^1\Sigma_g^+$	6 kR	$\approx$ 80
IR - FIR	$OH(\nu \leq 9)$	1 MR	$\approx$90

Table 2.1: Night time airglow emissions from 500 nm to far infrared. Listed here are only the brightest nightglow emissions in units of Rayleigh (R) between 500 and 1300 nm. One Rayleigh R = 4πI where the intensity I is measured in units of 10^6 quanta $cm^{-2}s^{-1}sterad^{-1}$. After McEvan & Phillips (1975)

rocket flights (e.g Thomas & Young (1981)). In addition space-based orbiting satellites are used to study the various airlow layers in the atmosphere (e.g Shepherd et al. (1995)).

Rocket and satellite measurements have previously indicated that the mid-latitude 557.7 nm emission peaks near 95 km (Thomas & Young 1981, Hernandez et al. 1995, Shepherd et al. 1995). The emission height profile of the atomic oxygen emission has a full width at half maxium (FWHM) of 10-12 km (Shepherd et al. 1995). The OH(6-2) emission (see Figure 2.6) originates from a layer at about 87 km height with a FWHM of 8-12 km (Baker & Stair 1988, Swenson & Gardner 1998).

2.3.1 Excitation

The excitation processes in the atmosphere can be divided into several mechanisms:

- Fluorescence is the emission process which results when an atom, molecule or ion is excited by light absorption.

- Resonant scattering is a special case of fluorescence where the emission and excitation wavelength are the same. In big volumes, like the atmosphere, this can lead to an isotropic scattered radiation such as the blue sky during the day.

- Excitation by charged particles due to the inelastic collision of photoelectrons and electron-ion recombination.

- The collisional deactivation (quenching) of excited species can involve excitation of the quencher by energy transfer.

- The chemical excitation process due to an exothermic chemical reaction can place the excess energy of the reaction into rotational, vibrational or electronic states.

The two processes relevant to this thesis are of the chemical excitation type.

2.3.2 Atomic Oxygen Layer

The photodissociation of O_2 produces neutral oxygen atoms in the thermosphere. The atoms produced slowly diffuse downwards to below 100 km where they are removed in a chemical reaction described by Barnes (1964). This reaction is very effective in this height region as it coincides with the maximum concentration of neutral atomic oxygen and because the $O(^1S)$ production rate is proportional to the square of the number density of the atomic oxygen. These are the conditions which lead to a high concentration of $O(^1S)$ atoms which de-excite by emitting photons of 557.7 nm wavelength.

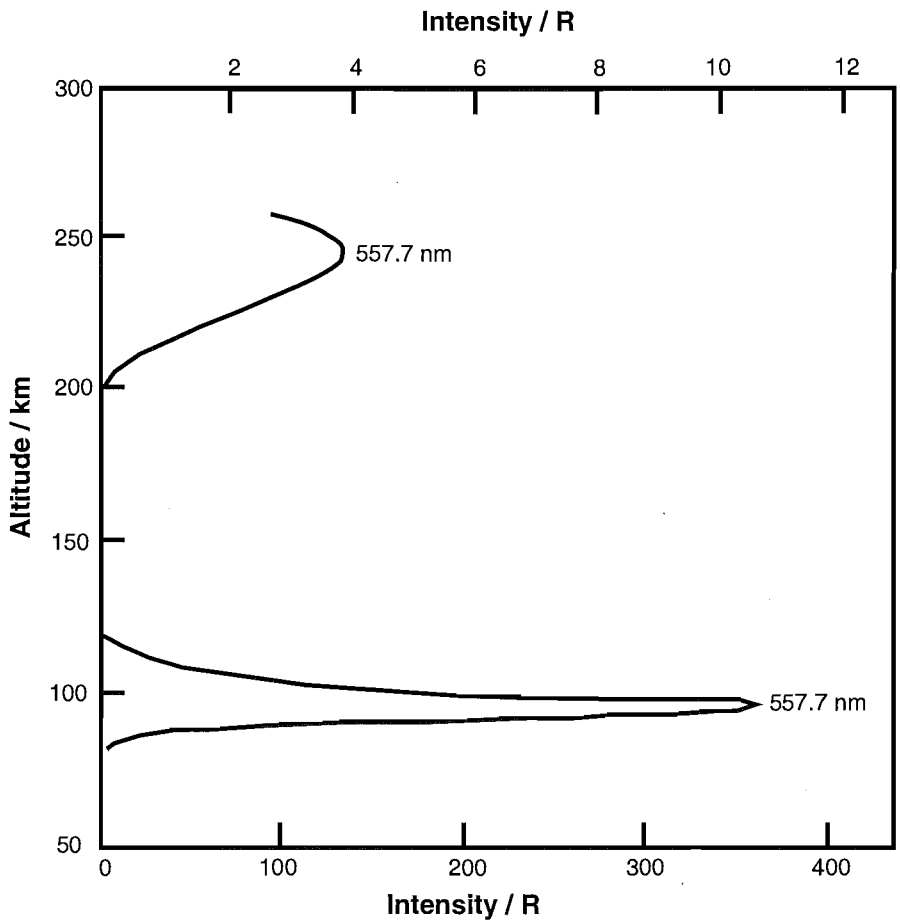

Figure 2.5: Height profile of the oxygen 557.7 nm airglow

The Barth mechanism (1964) is generally accepted as the major progenitor of the 557.7 nm emission. This mechanism is a two-step process involving a three-body association to produce O(^{1}S).

$$O + O + M \longrightarrow O_2^* + M$$

M here is any atomic or molecular species. Next the energy is transfered via collisional de-excitation (Witt et al. 1979) to produce O(^{1}S)

$$O_2^* + O(^3P) \longrightarrow O_2 + O(^1S)$$

The excited O_2^* molecule may radiatively de-excite or collisionally de-excite by other atomic or molecular species. The final stage involves radiative de-excitation of the O(^{1}S) atom:

$$O(^1S) \longrightarrow O(^1D_2) + h\nu(557.7\ nm)$$

The sharp drop-off in the emission below 95 km (see Figure 2.5) observed in the emission profile from rockets and satellites is a consequence of the increase in the collisional frequency and number density of quenchers such as O(^{3}P) atoms (Petitdidier & Teitelbaum 1979) or O_2 molecules (Thomas 1981) which de-excite the O(^{1}S) atoms by collisional energy transfer.

A high collisional frequency ($\sim$ 3500 s^{-1}) with the relatively long radiative livetime ($\tau \sim$ 0.74 s) of the O(^{1}S$_0$) state ensures that the oxygen atom is thermalised before emitting.

2.3.3 Hydroxyl Layer

The wavelength integrated hydroxyl (OH) emission is the brightest nightglow feature (see Table 2.1). Rocket measurements of the altitude profiles of OH* emissions (Rogers et al. 1973, Baker 1978, Baker & Stair 1988) show that the mean OH emission peak height is at about 87 km. The full width at half maximum of the emission height profile is measured to be between 8 and 12 km (Baker & Stair 1988, Swenson & Gardner 1998) A chemical excitation process is responsible for the excitation of the Meinel OH bands, named after A. B. Meinel (1950) who discovered the OH emission in the nightglow.

Several reviews of OH$^*(\nu')$ production and quenching in the mesopause have appeared in the literature. References of these reports are provided by (Bates 1982, Texier et al. 1987, Kaye 1988, Nicolet 1989, Meriwether 1989, McDade

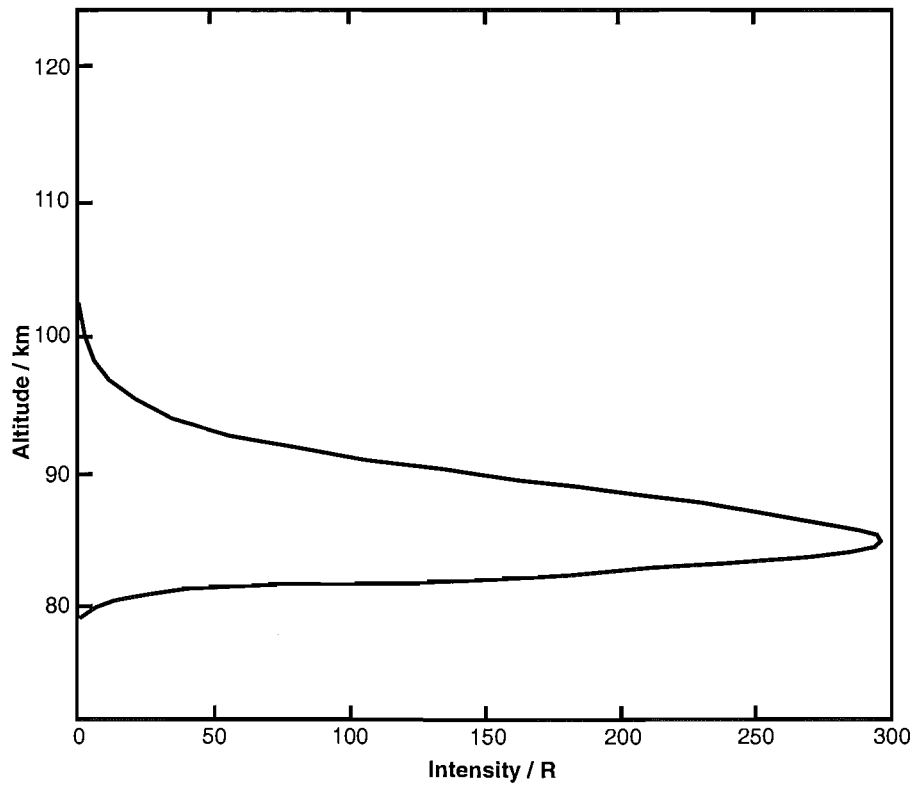

Figure 2.6: Height profile of the OH(6-2) airglow emission. After Petitdidier & Teitelbaum (1979)

1991, Sivjee 1992). The most widely accepted mechanism for the prodution of $OH^*(\nu')$ in the mesopause is the following exothermic hydrogen ozone reaction first proposed by Bates & Nicolet (1950):

$$H + O_3 \longrightarrow OH^*(\nu \leq 9) + O_2$$

While the Bates and Nicolet mechanism is accepted as the major source of the mesopause OH^* as yet no consensus has emerged on the exact distribution of the metastable radicals with their vibrational levels from $\nu' = 1$ to $\nu' = 9$.

Among the many possible OH emissions the $P_1(2)$ branch of the excited OH(6-2) transition emitting at 840 nm is used in this work to determine the wind's speed and direction at a height of about 87 km.

Chapter 3

Experimental Setup

The importance of multiple beam interferometry was first recognized by Bouloch (1893), who gave the theory of formation of a fringe system which was essential to the interferometer invented by Fabry & Perot (1897) who developed both the theory and practice of their celebrated plane parallel-plate interferometer. The Fabry-Perot spectrometer (FPS) is the most versatile optical interferometer. Instruments of this kind have been used for absolute wavelength measurements giving the highest precision, e.g. resolution of spectroscopic line structures such as the hyperfine structure, evaluation of the meter, determination of the refractive indices of gases, measurement of small displacements, etc. An instrument of this kind is used in this work to measure the wind speed and direction in the airglow layers of the atmosphere by measuring the Doppler shift of emission line profiles. With such high resolution the instrument is also able to measure the emission line width which gives the possibility to determine temperature in those airglow layers. Babcock first used a Fabry-Perot spectrometer in airglow studies in 1923 to determine the kinetic temperature of the 557.7 nm emission layer. The routine determination of winds and temperatures in the airglow layers of the

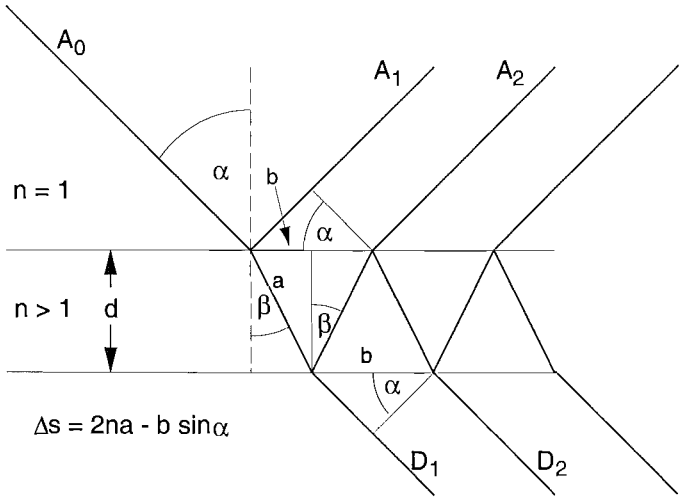

Figure 3.1: Path difference in a parallel plate.

mesopause, lower thermosphere region by optical means is a relatively recent technique, beginning in the 1960's (Armstrong 1968). Fully automatic FPS's are now employed throughout the world (Hernandez 1980, Jacka 1984).

3.1 Fabry-Perot Interferometry

The Fabry-Perot interferometry is based on multiple beam interference. A plane wave $E = A_0 exp[i(\omega t - Kx)]$ with an amplitude A_0, a frequency ω and a wavenumber k falls with an angle of incidence α to the normal onto a plane parallel, translucent plate with partly reflective surfaces (Figure 3.1). On each boundary surface the wave with amplitude A_i will be split into two beams, the reflected one has an amplitude $A_i\sqrt{R}$, the transmitted beam has an amplitude of $A_i\sqrt{1-R}$ provided absorption can be neglected. The reflectivity $R = I_R/I_i$ were I_R is the reflected intensity and I_i is the transmitted intensity depends on the angle of incidence α and on the polarisation. The path difference Δs between successive beams in a parallel plate is $\Delta s = 2nd\cos(\alpha)$ (n refractive index). As $n > 1$ within the plate and $n = 1$ outside, the resulting phase difference δ has to be taken into account, where

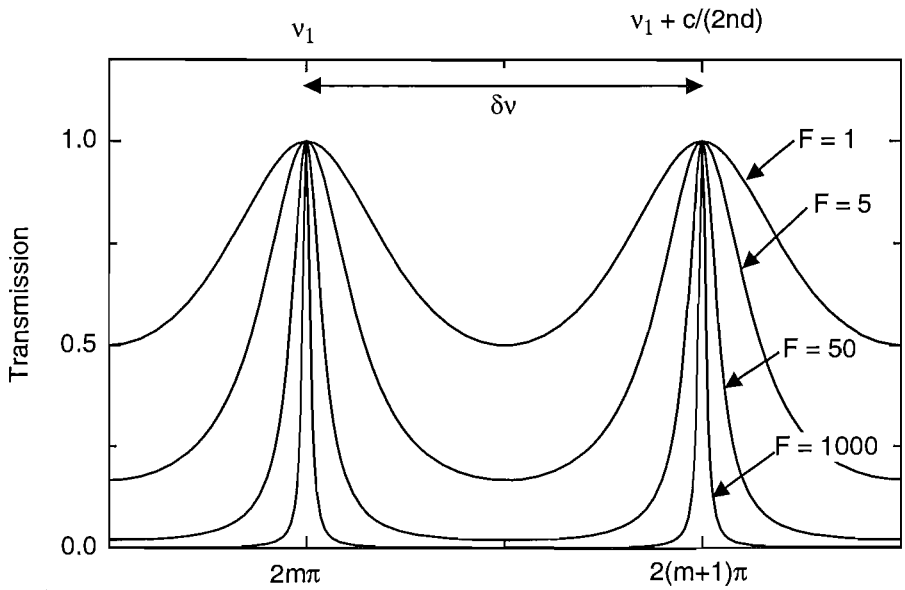

Figure 3.2: Transmission of a Fabry-Perot etalon with different values of finesse F. The Airy function has a periodicity of $2m\pi$. The distance between two successive maximas is the free spectral range (FSR), $\delta\nu$.

$$\delta = 2\pi\,\Delta s/\lambda + \Delta\phi$$

Here $\Delta\phi$ includes any phase jumps due to reflections. The first reflected beam A_1 experiences a phase jump $\Delta\phi = \pi$ as it is reflected at the optically denser medium so that

$$A_1 = \sqrt{R}A_0 e^{i\pi} = -\sqrt{R}A_0 \tag{3.1}$$

The sum of all reflected waves can be obtained by summing over the number of all phase corrected reflections p

$$A = \sum_{m=1}^{p} a_m e^{i(m-1)\delta} = -A_0\sqrt{R}\left[1 - (1-R)e^{i\delta}\sum_{m-1}^{p-2} R^m e^{im\delta}\right] \tag{3.2}$$

If the plate is infinitely large or if the angle of incidence $\alpha = 0$ so that number of reflections $p \to \infty$, the geometric series in Equation 3.2 has the limit

$$A = A_0\sqrt{R}\frac{1 - e^{i\delta}}{1 - Re^{i\delta}} \tag{3.3}$$

With the incoming intensity I_0 the intensity I_R of the reflected waves can be calculated to be

$$I_R = 2c\epsilon_0 AA^* = I_0 R\frac{2 - 2cos(\delta)}{1 + R^2 - 2Rcos(\delta)} \tag{3.4}$$

Similar considerations lead to the intensity I_T of the transmitted waves. Employing the finesse $F = 4R(1 - R)^{-2}$, the Airy formulas can be written as

$$I_R = I_0\frac{Fsin^2(\delta/2)}{1 + Fsin^2(\delta/2)} \tag{3.5}$$

$$I_T = I_0\frac{1}{1 + Fsin^2(\delta/2)} \tag{3.6}$$

where I_R is the intensity of the reflected beam and I_T is the intensity of the transmitted beam.

Figure 3.2 shows the transmission $T = I_T/I_0$ of a Fabry-Perot interferometer as a function of δ contoured with different finesse F. The Airy function and therefore the Fabry-Perot interferometer is periodic in frequency with a periodicity of $2m\pi$.

The free spectral range (FSR), which is the wavelength difference between two maxima of the Airy function, is

$$\delta_1 - \delta_2 = \frac{2\pi\,\delta s}{\lambda_1} - \frac{2\pi\,\delta s}{\lambda_1} = 2(m + 1)\pi - 2m\pi = 2\pi$$

with $\nu = c/\lambda$ the FSR can be rewritten in terms of $\delta\nu$

$$\delta\nu = \nu_{1max} - \nu_{2max} = \frac{c}{2d\sqrt{n^2 + sin^2(\alpha)}} \tag{3.7}$$

in the case of $\alpha = 0$ this simplifies to

$$\delta\nu = \frac{c}{2nd} \tag{3.8}$$

The full width at half maximum (FWHM) $\epsilon = |\delta_1 - \delta_2|$ of the transmission maxima $I_T(\delta_1) = I_T(\delta_2) = I_0/2$ can be obtained using Equation 3.6

$$\epsilon = 4\arcsin\left(\frac{1-R}{2\sqrt{R}}\right) \tag{3.9}$$

3.2 The Fabry-Perot Spectrometer at Mt. John

The instrument used for this work has been described in detail by Steve M. Smith (1996).

The physical experiment measures the Doppler shift of the emitting atomic or molecular species in the atmosphere due to motion in the atmospheric gas. Two emission layers are measured in the mesosphere and lower thermosphere (MALT). The OH-layer residing at about 87 km height emits various rotational transition lines, the $P_1(2)$ branch of the OH(6-2) transition emitting at 840 nm is measured in this thesis. The atomic oxygen layer at about 97 km height is also of interest, where the $O(^1S)$ transition occurs with a wavelength of 557.7 nm. The FWHM of both emitting layers are in the range of 10-12 km (see Section 2.3).

There are two motions to distinguish: the bulk motion of the particles which represents a wind; and the motion of the individual particles represented by

the velocity distribution. This latter is primarily a consequence of the temperature resulting in a Doppler broadening of the emission lines (although as will be shown later, wind shear in the airglow layer contributes to this). The frequency shift is measured with respect to the observer. As a consequence of the relative velocity between the observer and the emitting particles, the emission line is shifted in frequency. The observer at rest will measure the frequency

$$\omega = \omega_0 + \mathbf{K} \cdot \mathbf{v} \tag{3.10}$$

$$|K| = 2\pi/\lambda$$

For the wind determination at Mt. John all four cardinal directions are measured to obtain the zonal and meridional component of the horizontal wind. The wind velocity can be determined using

$$v = \frac{c\, F_\nu\, \nu_B}{\nu_0\, K_g\, F_B} \tag{3.11}$$

Here c is the speed of light, F_ν and F_B are the free spectral range in frequency and channels respectively. ν_0 is the frequency of the unshifted line while ν_B is the shift in channels of the shifted line. K_g is a factor which takes any geometric effect, such as a deviation from a horizontal observation, into account.

The measuring process is unable to determine the height of the emission layer itself. As a zero wind reference the zenith direction is measured assuming there is no vertical wind (or that it is significantly smaller than the uncertainties of the measured horizontal component, see Hernandez (1980), Price et al. (1995)). The zero wind reference is calculated, in this project, using the average over the whole night of measurements.

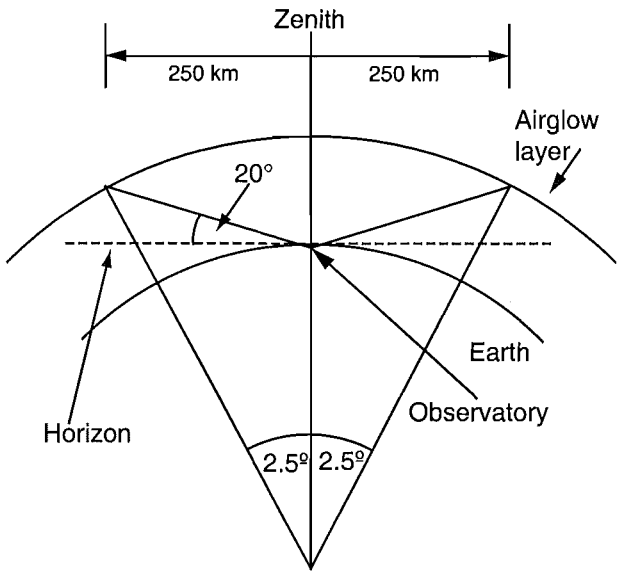

Figure 3.3: Sampling geometry of the Mt. John FPS (not to scale). The instrument is located at the Mt. John observatory and measures at an elevation angle of 20° above the horizon. As the airglow layers are at about 90 km height it sets the sampling volumes about 250 km to each side of the observatory. Taking the curvature of the Earth into account (about 2.5°) results in a corrected observation angle at airglow layer height of 22.5°.

The temperature is derived from the same fringes as the wind speed. Its determination is based upon the fact that, in the case of thermal equilibrium, the velocity of the gas molecules obey a Maxwell distribution

$$F(\boldsymbol{v})d^3v = \left(\frac{m}{2\pi kT}\right)^{3/2} e^{-mv^2/2kT} d^3v \tag{3.12}$$

where v is the velocity, k is the Boltzman constant, m is the mass of the molecule, and T is the temperature. This velocity distribution causes a Gaussian shaped Doppler broadening of the emission line measured. The temperature can be calculated using the FWHM of the measured Gaussian shaped emission line using

$$\delta\nu = 7.15 \times 10^{-7} \nu_0 \sqrt{\frac{T}{m}} \tag{3.13}$$

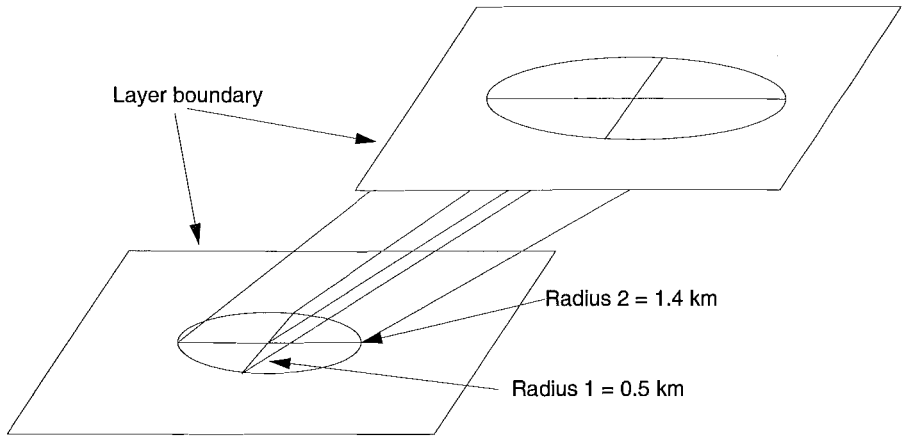

Figure 3.4: Geometry of the sampling volume in the mesopause.

where $\delta\nu$ is the width of the emission line in Hertz, ν_0 is the centre frequency, m is the mass of the molecule of atom, and T is the temperature.

To improve the signal-to-noise ratio each measurement takes about 10 - 15 minutes depending on the brightness of the OH emission (840 nm). The green line emission (557.7 nm) is measured simultaneously. Wind speeds and temperatures are averaged over the measuring time. A complete set of measurements in all 5 directions requires 50 - 75 minutes resulting in a time resolution for each individual direction of about 60 minutes.

The four major directions are measured at 20 degrees from the horizontal. As the maximum of the emitting particles resides at 87 km (OH, 840 nm) and 97 km (atomic oxygen, 557.7 nm) in height the observation distance from the observatory are 240 km and 267 km respectively. Taking the radius of the earth into account (see Fig. 3.3) leads to a corrected angle of observation of 22.5 degrees. At this angle the path through the emitting layer (FWHM $\sim$ 10 km) is approximately 23 km for the major directions. The solid angle of the FPS is about $\Omega = 1.2 * 10^{-2}$ steradian so that the sampled volume is about 50 km^3 for any cardinal (see Fig. 3.4) and 5 km^3 for the zenith direction.

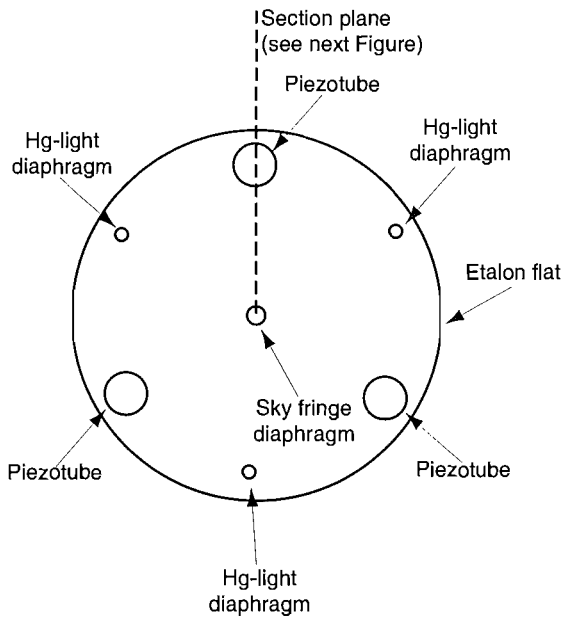

Figure 3.5: Topview onto the FPS etalon. Shown are the positions of the Piezotubes, the Hg-Lamp diaphragms, and the airglow fringe diaphragm. The dashed line indicates the crosscut section shown in Figure —refoptpath

3.3 Optical Path

The optical path can be described as follows (see Figures 3.5 and 3.6). The light from the sky is directed downwards to the FPS by a computer controlled mirror system which points in the appropriate direction. Passing a shutter, which is closed during the daytime to prevent daylight damaging the PMTs, the light reaches the etalon which resides in a temperature stabilised housing. The major component of the FPS is the etalon which consists of two optical quartz flats with a flatness of $\lambda/100$. The aperture of the 2 cm thick flats is 15 cm in diameter. The surfaces are coated with an aluminum coating which yields the reflectivities listed in table 3.1. A lens of 660 cm focal length focuses the light onto the scanning diaphragm with a diameter of 27 milli-Kayser at 632.8 nm. From there the light is split by a dichroic filter into a red and a blue beam where it is then further selected by interference filters

Year	557.7 nm	632.8 nm	840 nm
1991	0.794	0.7966	0.7920
1994	0.784	0.7754	0.7903
1996	0.8006	0.7534	0.7791
1997	0.8089	0.7531	0.7785

Table 3.1: Etalon reflectivities as measured with the Giacomo method (Giacomo 1952)

with a typical FWHM of 3 nm before it reaches the PMTs. The resulting signal is then discriminated and the count rate is registered by a computer.

The etalon flats are mounted with an air gap of 2 cm resulting in a FSR of 250 milli-Kayser. In order to scan the frequency range of interest the gap has to increase or decrease which is done by means of three high voltage driven piezo tubes. Applying a voltage ramp of 0-1000 Volts to the piezos increases the gap between the etalon flats resulting in a wavelength scan. A scan takes 9 sec, 8 sec for the scan and 1 sec for the fly back. As the parallelism of the etalon is important for the quality of the interference (sharpness of the fringes) it has to be monitored during the scan. This is achieved by measuring the fringes produced by three mercury lamps which light diaphragms lying between the piezo drivers on the edge of the etalon (see Fig. 3.6). At two points during the scan the signals of the mercury lamps are analysed if they cross the signal maximum at the very same time. In case there is any difference a correction voltage is applied to the corresponding piezo tube. This is done by means of an electronic device, the self alignment unit (SAU), which is basically a voltage controlled high voltage amplifier.

A second group of 3 piezos is built into the etalon which have their own high voltage amplifier. The purpose of this equipment is to keep track of any air pressure changes as high or low pressure systems move over the observatory.

Those pressure changes result in a change of the refractive index of the air between the flats causing the optical path length to change. This second group corrects for air pressure changes and increases or decreases the gap accordingly.

With all this technical preparation it is possible to obtain high quality fringes which enable the wind to be calculate with an accuracy of about 5 ms^{-1} and temperatures with an accuracy of up to 2 Kelvin.

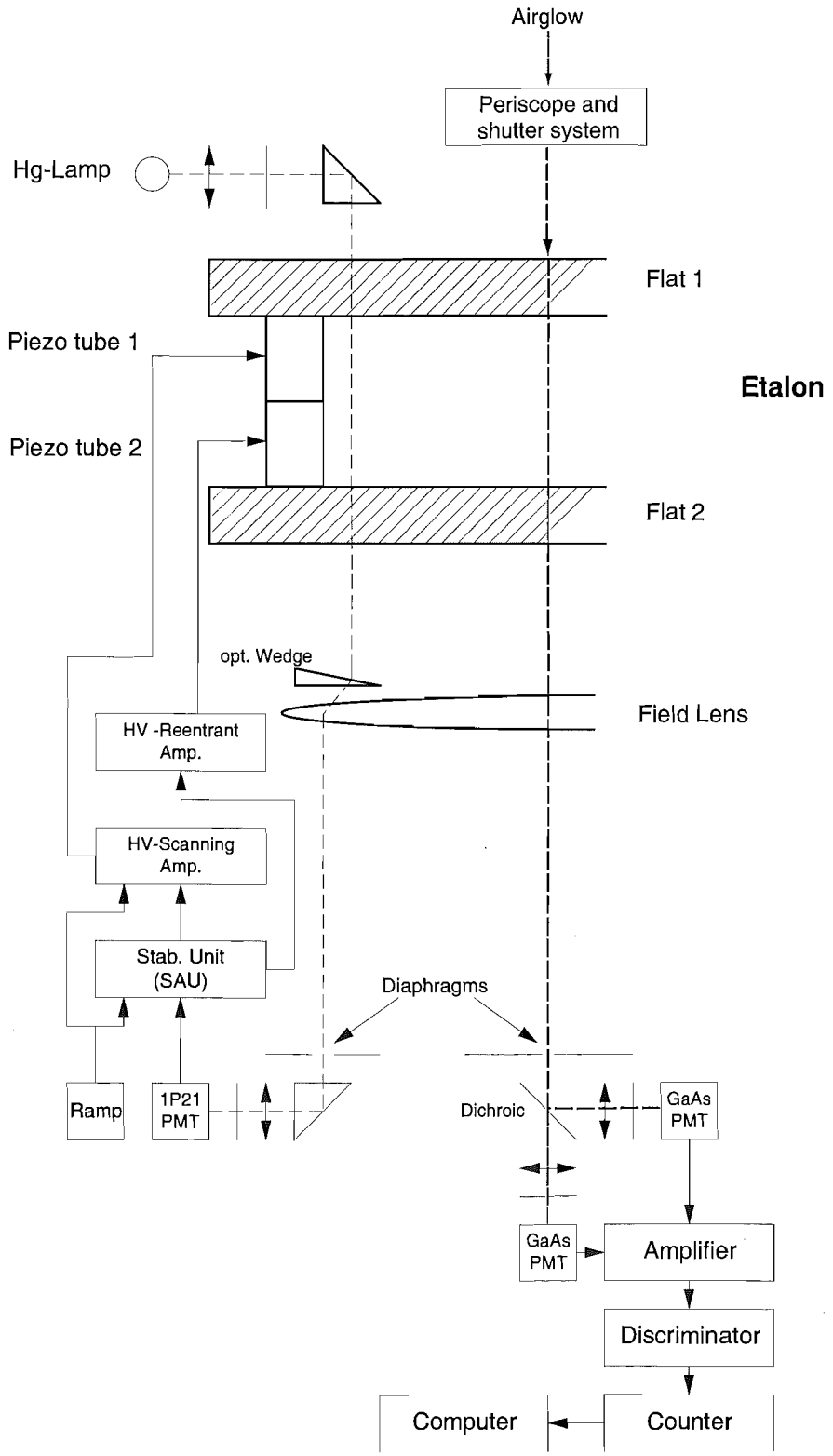

Figure 3.6: Optical path and electronic components of the FPS.

Chapter 4

Data Reduction

The data reduction methods described in the following section describes the methods employed to reduce the optical Fabry-Perot spectrometer data. The data originating from the meteor radar and the medium frequency radar used in this thesis were obtain from my co-workers G. Fraser and S. Marsh in reduced form.

4.1 Pre Data Selection

The recorded raw data can be corrupted by various effects. It is therefore important to select only those measurements which are unaffected. Clouds are a major disturbance that corrupt the data as they act like a diffuser and the recorded Doppler shift is then due to the movement of the clouds and not the motion of the atmospheric gas near the mesopause. The green line fringes can look reasonably good showing only a slightly decreased S/N ratio despite a thin cloud cover. The S/N-ratio of OH-fringes, however, are very much affected by clouds and the fringe features vanish even with

relatively thin clouds. This result can however be used to detect clouds and therefore reject the OH and contemporaneous measured green line data. Even so, this cloud detection is not the *ultima ratio* as it assumes that the emissions are homogeneous which is not the case for the OH and green line emission (Peterson & Kieffaber 1973, Taylor & Garcia 1995). Patches of weaker airglow emission moving into the field of view will reduce the S/R ratio which could be misinterpreted as a cloud. A weaker OH emission is therefore not necessarily indicating a cloud in the field of view. A good meteorological log is essential for rejecting those nights or periods of the night where clouds were present.

Another source of data corruption is increased geomagnetic activity. The published planetary magnetic index K_p is used to determine the geomagnetic activity. Nights with a $K_p < 3$ are considered quiet and therefore suitable. With a higher geomagnetic activity the auroral 557.7 nm emission from above 100 km height would contaminate measurements of the wind and temperature in the mesopause region (Hernandez 1988, Phillips et al. 1994).

4.2 Wind Determination

The wind is measured by detecting the Doppler shifted profile of the airglow emission. The wind determination is done by means of a comparison with a zero wind profile, as a "zero-shifted" reference profile, with any other profile. Any difference in fringe location of any profile from the cardinal directions with the reference profile (zero wind profile) is a measure of the wind. The shift in frequency is converted into a wind speed by use of the formula below:

$$v = \frac{c\, F_\nu\, \nu_B}{\nu_0\, K_g\, F_B} \tag{4.1}$$

Here c is the speed of light, F_ν and F_B are the free spectral range in frequency and channels respectively. ν_0 is the frequency of the unshifted line while ν_B is the shift in channels of the shifted line. K_g is a constant which takes any geometric effect, like a deviation from a horizontal directed measurement, into account. In the setup used here where the measurement is taken at an elevation angle of 22.4° $K_g = \cos 22.4°$ is the projection of the recorded wind vector onto the horizontal plane.

To obtain the frequency shift (Doppler shift), only the position of the fringe maximum and the free spectral range needs to be determined. This position parameter is independent of all other parameters which are varied in order to fit the Gaussian model to the data. A deconvolution of the FPS response function, important to derive temperatures, is not strictly necessary although it reduces the fitting error and therefore the uncertainty in the wind. (Tests showed that the uncertainty decreased by about 10%.) The noise level in the data produced comparable errors with both methods. So the direct-fit method and the Fourier transform method are equally usable. Only when the signal to noise ratio sinks far below the typical signal quality did the Fourier transform method yield results superior to the direct-fit method.

As the expansion of the piezo-electric crystal stacks is not linear as the scanning voltage increases the fringes occur, from order to order, closer and closer together. This non-linear behaviour, described and analysed by Hernandez (1978*b*), has been numerically removed from the raw fringes prior to any wind calculations. This linearization process produces unevenly spaced data which have to made evenly spaced in order to calculate the temperature using the Fourier coefficients. The linearization procedure is not necessary with the new etalon (installed February 1997) which employs piezo-electric tubes instead of stacks. These tubes show linear expansion with voltage. The additional steps of calculating the linearization and the subsequent calculation

of the evenly spaced data by interpolating can be avoided. This reduces noise introduced by the interpolation and therefore reduces uncertainty of the obtained results.

To obtain the zero wind reference the positions of the zenith fringes are averaged. This mean position is then used to calculate any possible Doppler shift. Individual zenith fringe shift are measured against the mean position to give a zenith wind. The variation σ_z of this so called zenith wind is added to the uncertainties σ_f of the fit for all other wind calculations.

Another source of uncertainty is the fluctuation of the FPS etalon. This can be determined by measuring the shift of the laser fringes accumulated during the day time. The laser fringes are recorded primarily to calculate the response function of the Fabry-Perot spectrometer necessary to calculate the temperature but are also used in the wind determination to calculate the position fluctuations of the etalon. The variation σ_L of this "laser wind" also has to be taken into account. The uncertainty of the wind is typically 7-10 ms^{-1} and given by:

$$\sigma_w = \sqrt{\sigma_f^2 + \sigma_z^2 + \sigma_L^2}$$

The effect of correcting for the dead-time of the detection system is hardly noticeable as the event rates are much to low. For the wind determination a correction in therefore not necessary. For the temperature determination, however, the dead-time of the system is of importance as recorded intensity depends in a non-linear manner on the brightness of the emission source.

4.3 Temperatures Determination

The temperature determination is more complicated than the wind determination as the fitting algorithm has to fulfill more requirements (see section 4.4). The number of free parameters determined by the fitting algorithm is larger and they are partly interdependent. The temperature is obtained by measuring the width of the fringes at half maximum, it is therefore essential to deconvolve the response function of the FPS from the fringes. Prior to the deconvolution the fringes have to be linearised as described above (see section 4.2). The response function of the FPS is measured by means of a He-Ne laser line emission (632.8 nm). The laser is highly frequency stable and hence has a width which is considered negligible. However, the measured fringes of the laser emission still appear to have a width due to the convolution of the laser emission with various functions (see Section 4.4). This response function is then deconvolved from the sky fringes. The resulting fringes are afterwards fitted with a model function to obtain the width of the fringe.

The dead time of the photon counting components, negligible for the wind calculation, has to be taken into account and the fringes have to be corrected using

$$C_c = \frac{C}{1 - Ct_0}$$

where C_c is the corrected intensity, C is the measured intensity and t_0 is the dead time of the FPS electronics. As the signal intensities increase the dead time correction becomes important. The event rate for sky fringes is about 500 and 150 photons per second for the green line and the OH emission respectively. The laser fringes however have a rate of about 7000 events per second which makes the dead time correction necessary. The dead time of the FPS used here has been measured to about $2.5\mu sec$. With no dead

time correction the fringes appear broader and consequently lead to a higher (sky fringes) or lower (laser fringes) temperature. After those corrections the temperature is calculated using Equation 4.3.

4.4 Fitting techniques to derive temperatures and winds

Two techniques immediately come to mind when recovering Doppler line profiles to derive temperatures from Fabry-Perot spectrometer (FPS) observations. There is firstly the technique, demonstrated by Hays & Roble (1971), which employs discrete-Fourier-transformation (DFT) of the profiles and nonlinear least-square fitting of the low-order coefficients. Hernandez (1978*a*) showed that the low-order Fourier transformation coefficients can be least-square fitted to obtain the temperature of the emitting species.

The second technique makes use of a multiparameter nonlinear least-square fit using the Levenberg-Marquardt algorithm to fit a model function to the raw data. This direct fit has the disadvantage of slower speed and less sensitivity to any line shapes when compared with the DFT.

The analysis of FPS data requires knowledge of the instrument parameters, i.e. the reflectivity of the etalon, the optical gap, the scanning aperture, and the defects function. This information can be obtained by means of a response function measured using a spectral stabilized laser.

The analysis of single lines has been carried out with DFT methods and is well described by Hernandez (1978*a*, 1986). The analysis of multiplet structures (i.e. lambda-doubled molecular emission features) requires a more complex analysis (Conner et al. 1993). The DFT is still slightly faster but statistical

fluctuations play a more important role in limiting its usefulness. The determination of Doppler shift (winds) and Doppler broadening (temperature) requires the determination of the signal intensity and the background sky intensity, two parameters one does not need to pay any attention to when performing DFT on periodic structures. In the following the two techniques (Direct-fit method, Fourier-transform method) are described for single as well as double peak structures. These descriptions are excerpts from the paper by Conner et al. (1993) which also describes the advantages and disadvantages of these methods. Their conclusion is that the direct fit method to derive Doppler temperature from multiple-line Fabry-Perot profiles produces more consistent results and is less sensitive to noise than the method of least-squares fitting to low-order Fourier-transform coefficients.

4.4.1 Direct-Fit Method

The direct-fit determination of the Doppler shift and width starts with an analytical model of the expected profile with start values of peak position, width, maximum intensity, and background intensity. The Levenberg-Marquardt (1963) method is then used to minimize the least-squares error in the χ^2 sense by varying the parameters. This method is a combination of the inverse-Hessian and the steepest-descent methods. The steepest-descent method is used to get close to the minimum, and then the inverse-Hessian method takes over.

As Doppler-broadening plays the dominant role in the line width of the measured atomic or molecular transitions (Demtröder 1991, Chapter 3) the analytical model for the expected profile is the convolution of a Gaussian Doppler line profile with an instrument function for the spectrometer in use. The instrument function is a convolution of the Airy function, describing a perfect

etalon with a given reflectivity, the top-hat function of the scanning aperture, and the etalon surface defects. The etalon surface defects are determined by a direct-fit of the recorded fringes from a frequency stabilized He-Ne laser. This assumes a negligible laser width when compared with the instrument function. Presuming that the width found is Gaussian the defects can be expressed by the FWHM or can be translated into an effective temperature (Conner et al. 1993). The defects-width can than be deconvolved from the measured profile width by simply subtracting the squares.

Singlet Analysis

From the Maxwell-Boltzmann distribution of molecular speeds it follows that the analytical expression for the Doppler broadening is a Gaussian profile $g(\lambda)$:

$$g(\lambda) = N + \frac{g_0}{\sqrt{\pi}} \left(\frac{\sqrt{2}}{dg} \right) exp \left[-(\lambda - \lambda_0)^2 \left(\frac{\sqrt{2}}{dg} \right)^2 \right] \tag{4.2}$$

where

$$dg = \frac{7.15 \times 10^{-7}}{2ln2} \lambda_0 \sqrt{\frac{T}{m}} \tag{4.3}$$

$$dg_i = \frac{\lambda_i}{\lambda_0} dg$$

T is the temperature in Kelvin, c is the speed of light, k is the Boltzmann constant, λ_0 is the non-Doppler shifted emission wavelength, λ is the Doppler shifted emission wavelength, m is the mass in atomic mass units, g_0 and N are signal and background intensities, and A is Avogrado's number.

Doublet Analysis

For the analysis of a doublet there has to be a second term added and the model, assuming the intensities are equal, is

$$
\begin{aligned}
g(\lambda) = N+ \\
&\frac{g_0}{\sqrt{\pi}}\left(\frac{\sqrt{2}}{dg_1}\right) exp\left[-(\lambda-\lambda_1)^2\left(\frac{\sqrt{2}}{dg_1}\right)^2\right] + \\
&\frac{g_0}{\sqrt{\pi}}\left(\frac{\sqrt{2}}{dg_2}\right) exp\left[-(\lambda-\lambda_2)^2\left(\frac{\sqrt{2}}{dg_2}\right)^2\right]
\end{aligned}
\tag{4.4}
$$

where

$$
\begin{aligned}
\lambda_1 &= \lambda_0 - \Delta, \\
\lambda_2 &= \lambda_0 + \Delta
\end{aligned}
\tag{4.5}
$$

for Δ equal to one half the value of the doublet spacing.

As the measurement is a discrete process the spectrum is sampled and binned into channels Equation 4.4 has to be expressed in terms of channel number x_i:

$$g(x_i) = N+$$

$$\frac{g_0}{\sqrt{\pi}}\left(\frac{\sqrt{2}}{dg_1}\right) exp\left[-(x_i - x_{01})^2(x_{cal})^2\left(\frac{\sqrt{2}}{dg_1}\right)^2\right] + \frac{g_0}{\sqrt{\pi}}\left(\frac{\sqrt{2}}{dg_2}\right) exp\left[-(x_i - x_{02})^2(x_{cal})^2\left(\frac{\sqrt{2}}{dg_2}\right)^2\right] \tag{4.6}$$

$$x_{cal} = \frac{[nm]}{\text{sample units}}$$

This expresses the Gaussian Doppler line profile model which has to be convolved with the aperture function P and the Airy function $A(R)$ to obtain the desired model function $M(T, g_0, N, x_0)$:

$$M(T, g_0, N, x_0) = A(R) \otimes F \otimes g(T, g_0, N, x_0, \delta); \tag{4.7}$$

In the case of a singlet source profile g is independent of δ. The aperture function F is described by a top-hat function of unit area. The Airy function $A(R)$ is a periodic function of the etalon reflectivity R which is described in detail by Born and Wolf (1959). The width of the defects function, obtained by measuring the emission of a He-Ne laser, is included in the width of the signal function g. To remove the influence of the defects function its width has to be recalculated from the laser line wavelength to match the wavelength of interest (here 557.7 nm and 840 nm). The width obtained can now be subtracted by means of an effective temperature or by subtracting the square of the defects width from that of the signal function g:

$$dg_{res}^2 = dg_n^2 - dg_{laser}^2$$

4.4.2 Fourier-transform Method

As in the direct-fit method model, the Airy and the aperture functions are generated and convolved to produce a model instrument function. The instrument function obtained and one order of the scanned emission profile is then transformed using the DFT. The model instrument function is deconvolved from the emission profile by division in the frequency domain. The remaining coefficients describe the source function convolved with the defects function. This defects function can be represented by an effective temperature. The instrumental defects can again be measured by a frequency stabilized He-Ne laser which has a narrow spectral width that can be neglected compared with the width of the defects function. The obtained coefficients will be linear fitted. The temperature is then derived from those fit parameters as shown below.

Singlet Analysis

In the case of a Doppler-broadened singlet structure defined by Equation 4.2 the Fourier transformation $G(s)$ where s is the transform variable is described by:

$$G(s) = \int_{-\infty}^{+\infty} \left(\frac{\sqrt{2}}{dg\,\pi}\right)^2 exp\left[-\left(\frac{\sqrt{2}}{dg}\right)^2 (\lambda - \lambda_0)^2\right] exp(-2\pi i s\lambda)\,\mathrm{d}\lambda \quad (4.8)$$

which gives

$$G(s) = exp\left[-\left(\frac{dg\,\pi\,s}{\sqrt{2}}\right)^2\right] exp(-2\pi i s\lambda_0) \quad (4.9)$$

$$|G(s)|^2 = exp\left[-(dg\,\pi\,s)^2\right] \quad (4.10)$$

Taking the logarithm of both sides of Equation 4.10 and using the definition of dg one gets:

$$ln[|G(s)|^2] = -(dg\,\pi\,s)^2 = -\left(\pi\,s\,\frac{7.15\times10^{-7}}{2ln2}\lambda_0\right)^2\frac{T}{m} \tag{4.11}$$

which shows the linear relation between the slope of the Fourier coefficients and the temperature, as stated by Hernandez (1986). He uses a linear-regression analysis to obtain a value of T from a scanned sky profile. The phase information in Equation 4.9 can be used to locate the peak position which is required for wind measurements but not for the derivation of temperatures. In Equation 4.8 the signal is set to $g_0 = 1$ and the background is set to $N = 0$ as g_0 enters the final expression as a constant and $N \neq 0$ provides additional power in the zeroth order coefficient as it raises the mean signal level.

Doublet Analysis

The Fourier transform of the doublet Equation 4.4 is written as

$$\begin{aligned} G(s) &= exp(-2\pi is\lambda_1)exp\left\{-\beta^2s^2\left[1-2\frac{\Delta}{\lambda_0}+\left(\frac{\Delta}{\lambda_0}\right)^2\right]\right\}+ \\ &\quad exp(-2\pi is\lambda_2)exp\left\{-\beta^2s^2\left[1-2\frac{\Delta}{\lambda_0}+\left(\frac{\Delta}{\lambda_0}\right)^2\right]\right\} \end{aligned} \tag{4.12}$$

where Δ is defined in Equation 4.5 and β^2 is set to

$$\beta^2 = \pi^2\frac{dg^2}{2}$$

Thus the absolute square of G yields

$$
\begin{aligned}
|G(s)|^2 &= 2exp\left\{-2\beta^2 s^2\left[1+\left(\frac{\Delta}{\lambda_0}\right)^2\right]\right\} \\
&\times\left[cosh\left(4\beta^2 s^2\frac{\Delta}{\lambda_0}\right)+cos(4\pi s\Delta)\right]
\end{aligned}
\tag{4.13}
$$

In the case of $\Delta \ll \lambda_0$, as for the OH transition $P_1(2)$, the approximation $cosh(\ldots) = 1$ can be used. The transition from the expression in Equation 4.13 to a discrete representation can be made by considering the convolution procedure shown in Equation 4.6. The spectrum is periodic as the periodicity of the Airy function produces successive orders of the spectrum. This periodicity determines the discrete values which the transform variable s can obtain. These values are harmonics of the periodicity of the Airy function. Thus the sampled points in Fourier space are in the series $s_n = n/\tau$, where τ is the period of the Airy function or the free spectral range (fsr) and n is any positive integer.

With this in mind Equation 4.13 can be rewritten to

$$
\begin{aligned}
ln[|G_n(s_n)|^2] &= -\left(\pi\, s_n\frac{7.15\times10^{-7}}{2ln2}\lambda_0\right)^2\frac{T}{m} \\
&+ln\{1/2[1+cos(4\pi s_n\Delta]\}+ln(4)
\end{aligned}
\tag{4.14}
$$

This expression is the same as that for the singlet analysis except for the additional modulation given by $ln\{\ldots\}$. The temperature has to be determined from the slope of the graph of the demodulated expression.

4.4.3 Conclusion

Wind speed is determined by means of a comparision with a zero wind profile (see Section 4.2). To obtain the frequency shift (Doppler shift) only the determination of the position of the fringe maximum and the free spectral range is necessary. This position parameter is independent of all the other parameters varied in order to fit the Gaussian model to the data. A deconvolution, important to derive temperatures, is not strictly necessary although it reduces the fitting error. The direct-fit method and the Fourier transform method appear equally usable.

Temperature determination is more crucial as the width of the Gaussian model function depends on the amplitude determined during the fit. Furthermore it has to deal with the convolution of Airy function, aperture function, defects function and signal. These have to be deconvolved in order to derive correct temperature. As long as only singlet structures are to be analysed both methods give results within the errorbars and the only advantage seems to be the speed of the DFT algorithm. However, when it comes to more complicated structures such as doublet profiles the DFT method is found to be more sensitive to S/N ratio. The presence of spectral features and the significant statistical fluctuations appear to produce distortions in the DFT of the observed spectrum. These distortions cause large errors in the derived temperatures (see Conner et al. (1993)). Conner et al. (1993) showed that the nonlinear least-squares method is the better method of analysis in the case doublet structures such as the OH $P_1(2)$ transition.

The software to reduce the raw spectrometer data used in this work was written by the author of this thesis. The software can linearise the recorded spectrum to allow the reduction of data measured prior to February 1997. It corrects for the dead-time of the detection system and automatically rejects

spectra which differ from the mean free spectral range by more than 1%. The software uses the direct-fit method for both the singlet analysis of the OI data and the doublet analysis of the OH data.

Chapter 5

Meteor Radar and Medium Frequency Radar

In this thesis data originating from meteor radar and medium frequency radar facilities is used. The following paragraphs give a short introduction into how these techniques are used for measuring winds in the mesosphere and lower thermosphere. Reduced data were obtained from colleagues at the University of Canterbury. A brief description of these techniques is only included for completeness and the reader is referred to the primary and secondary literature for a more detailed description

5.1 The Meteor Radar

The AMOR facility began operation in 1990. Its primary purpose is to determine the orbits of meteoroids down to a limiting diameter of $\sim 100 \mu m$. The system uses a 26.2 MHz, 60kW pulse radar transmitter at a pulse repetition frequency of 379 s^{-1}. A fan shaped antenna beam is used so as to restrict the

azimuthal radiation pattern to $\sim 1.5°$ (Baggaley & Bennet 1996). Thus, by confining the azimuth angle only the elevation angle needs to be measured in order to locate the position of the reflection point. A transmitter located at Birdlings' Flat, on the South Island of New Zealand (172° 39′ E, 43° 34′ S) radiates in the meridian towards both geographical North and South. In the presence of a wind, the electron train of the meteor is known to move with it provided that the electron/ion collision frequency is much smaller than the gyrofrequency for ions or electrons, i.e., below 140 km. Recent modifications to the radar have meant it is now possible to measure a Doppler shift in the transmitted radiation caused by any such movement of the train and infer a line of sight wind velocity. From the line of sight velocity a horizontal meridional wind component can be determined.

5.1.1 Details of Height Measurement

Many meteor wind radars determine echo reflection heights from the inferred rate of diffusion or simply assume a representative height for all observations, (Muller 1966). As echo points must lie near the meridian through the Home site (as the array beam width is only 1.5°) AMOR can use simple geometry because both the elevation and range of the train's specular reflection point are determined. AMOR is capable of determining event heights accurate to 1 km which is equivalent to the width of one Fresnel zone and hence cannot be improved upon.

5.1.2 Determining Elevation Angle

The elevation angle is obtained via a dual interferometer consisting of three receiving antennas called for historical reasons 1, 4 and 5 located at the

Home site. The inter–antenna spacing of 3.0λ and 11.5λ have been chosen to prevent elevation ambiguities for angles of 0–180°. The phase differences between antennas are obtained via two phase detectors and analysis of their analogue output provides elevation angles accurate to 0.3°.

5.1.3 Determining Range

Transmitter pulses are sent every $2.64ms$ and the returned signal is sampled with $66 \times 40\mu s$ range bins each representing a 6 km increase in range. Due to the pulse length and receiver bandwidth, echoes are generally detected in three adjacent bins and analysis comparing the relative amplitudes in these bins enables a more accurate determination of the range and therefore height.

5.1.4 Phase Measurements

The signal present at the radar's receivers is split into both phase and phase-quadrature components. As the receiving antennas can "see" the transmitting antenna, a ground pulse (radiation coming directly from the transmitting antenna) precedes any reflected radiation and hence data for both the ground pulse and reflected radiation can be received and stored. Receiving the ground pulse has many advantages in this system. Firstly, circuits at the receiver site make use of this ground pulse to ensure that local reference oscillators stay on frequency with those of the transmitter. The second major use of the ground pulse comes about in the analysis technique.

5.1.5 Analysis Technique

The line of sight wind component is obtained from the frequency change experienced by the transmitted pulse when reflecting from the moving meteor train. As frequency is proportional to the phase change of the echo signal with time $\frac{d\phi_E}{dt}$ it can be seen that the train velocity is simply given by $|v| = \frac{\lambda}{2\pi}\left[\frac{d\phi_E}{dt} - f_0\right]$ where λ is the wavelength of the transmitter signal and f_0 is the transmitter frequency. As phase and phase quadrature information are recorded for both echo and ground pulse, the time rate of change of both echo and ground pulse can be obtain . Therefore the above expression can be modified to give $|v| = \frac{\lambda}{2\pi}\left[\frac{d\phi_E}{dt} - \frac{d\phi_T}{dt}\right]$, where ϕ_T is the transmitter phase.

$\frac{d\phi_E}{dt}$ and $\frac{d\phi_T}{dt}$ are calculated using a linear least squares fit which also provides an uncertainty value. Those echoes for which the uncertainty is deemed too large are rejected at this point.

Typically data are averaged into time bins of one hour at the various heights (which range from about 70 – 110 km). The average provides a mean value with a standard deviation which can be used as an uncertainty for further analyses.

5.2 The Medium Frequency Radar

The medium frequency radar facility located at Birdlings' Flat has been routinely producing mesospheric, lower thermospheric wind measurements by the Spaced Antenna method since 1964 (Fraser 1965, Fraser 1968). The radar is a partial reflection radar which operates in a pulse mode at vertical incidence using a frequency of 2.4 MHz. The partial-reflection spaced-antenna method enables monitoring of the ionosphere between 60 and 100 km height

region. The MF radar probes the mesosphere, lower thermosphere region by sending short, high powered radio pulses vertically into the atmosphere. A triangle shaped array of ground-based antennas detects and records the back-scattered Fresnel echoes, each of which are similar in form, but shifted in time due to the relative spatial displacements of the antennas. Partial reflections from the entire height region between 80-100 km, with a sampling interval of 1 km, are acquired in about 90 seconds. Raw radar winds are obtained about every 10 minutes, depending on the data quality.

The signal amplitude of the back-scattered pulse at each antenna is observed to fluctuate temporally, this is known as fading. The fading records are analysed using the Full Correlation Analysis (FCA) technique (Briggs et al. 1950, Brown & Chapman 1972, Briggs 1984). The Brown and Chapman algorithm is used at Birdlings Flat for historical reasons and it differs from the Briggs method in that it uses one side of the antenna array triangle as a baseline to calculate the apparent velocity. The apparent velocity is the velocity obtained from the pattern changes due to its movement taking the disturbance of the pattern due to turbulence etc. into account converts the apparent velocity into the true velocity. The true velocity is determined by employing the characteristic ellipse to correct the apparent velocity. Unlike the Briggs method, the Brown and Chapman algorithm gives no error estimates for the derived parameters.

The back-scattered radio pulse produces a defraction pattern on the ground. This pattern is detected by the receiving antenna arrays. The line joining the points in the defraction pattern which are responsible for the maxima in the signal strength recorded at each of the receiving antennas is known as the "line of maxima". This "line" is assumed to be aligned perpendicular to the direction of drift. If random motions within the defraction pattern are assumed to be small then the apparent drift velocity can be derived from the

time lag of the maximum of the cross-correlation function between each pair of the spaced receivers.

Chapter 6

Data Comparison of Wind Measurements

6.1 Introduction

An important test for any measurement technique of a physical quantity is whether it delivers results consistent with data obtained by other accepted techniques. Since frequently there is no clear 'reference method', intercomparisons between several measurement techniques at the same time are most useful as they can uncover systematic biases and shortcomings. Instrumental biases are of particular interest since observations are frequently used to validate computer models.

Research undertaken by the Department of Physics & Astronomy allows an intercomparision of wind measurements in the mesopause by three different ground based instruments to be made. This chapter will present the results of a comparison of wind measurements in the mesopause, lower thermosphere region using a meteor radar (MR), a medium frequency radar (MF) and

an optical Fabry-Perot spectrometer (FPS). The comparison will focus on both short- and long term variations of the observed winds at the height of the hydroxyl airglow layer (about 87 km) and the atomic oxygen airglow layer (about 97 km). It will further show as a consequence of the result of the comparison that the height of the airglow layers can be obtained by comparing the wind measurements of the FPS and the MR. The variations of the airglow heights of the atomic oxygen and the hydroxyl layer are derived using data from the period between May 1997 and April 1998.

At first the location and the properties of the three instruments will be briefly discussed to show that the instruments used here are co-located or in close proximity to each other. Thereafter the data preparation and the height determination are revealed followed by the presentation of the results of the wind comparison. While generally good agreement is obtained between the FPS and the MR data, on several occasions the night-time wind compares poorly. Possible reasons for this behaviour are presented. The comparison between the MF and MR night-time data is poor, however, the day-time data shows occasionally good agreement. The variation of the airglow heights are presented in 6.6 showing a constant height OI airglow layer and a hydroxyl layer that shows an annual variation with the lowest height in early summer.

6.2 Location and Instrumentation

All three instruments referred to in this work are located on New Zealand's South Island. The FPS is located at Mount John in the centre of the South Island (43°59'S, 170°28'E) (Hernandez & Smith 1995), while the MR and the MF operate at Birdlings Flat (43°49'S, 172°41'E) near Christchurch on the east coast, as shown in Figure 6.1. The zonal distance between the

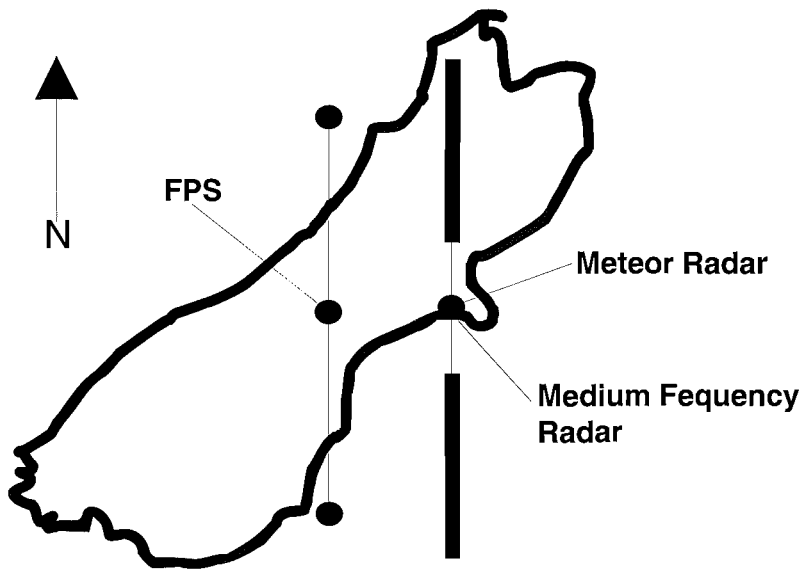

Figure 6.1: The South Island of New Zealand with the location of the MR and MF radars and the Fabry-Perot spectrometer. The dots indicate the location of the FPS sampling volumes. The bars are the ground range of the meteor radar volume.

observation sites is about 180 km and the meridional sample volumes are, also due to the different operational setups of the instruments, distinct (see Figure 6.1).

The FPS at Mount John used for the wind measurements has been described in detail earlier (Hernandez 1986) (see also Chapter 3). The high-resolution Fabry-Perot spectrometer simultaneously measures the spectral position of the emission lines due to the OH(6-2) $P_1(2)$ transition at 840 nm and of the atomic oxygen line (OI) at 557.7 nm. The observed lines are Doppler-shifted relative to a reference position due to large-scale motion of the atmosphere and thus allow determination of the horizontal wind component in the mesopause, lower thermosphere region. The instrument looks at an elevation angle of 20 degrees above the horizon and in the four cardinal directions and zenith. The uncertainties of determination for the FPS winds are about 4-8 m/s throughout the night and are dependent on the brightness

of the airglow.

The meteor wind Doppler radar is an addition to the existing meteor orbit radar system (AMOR) (Baggaley et al. 1994) and measures the meridional component of atmospheric motion. Incoming meteoroids produce a trail of ionized molecules which acts as a radio wave reflector. As this trail follows the air motion, the wind speed is determined by measuring the position of that trail with consecutive pulses of the meteor radar. Typical uncertainties in the meteor wind determinations are about 4-10 m/s, with the larger values in the early evening hours due to a fewer number of recorded meteor events. AMOR is capable of determining event heights with a precision of 1 km. On average the instrument detects over 100 meteors per hour over a height range between 75 to about 120 km.

The MF radar obtains winds by the partial-reflection technique (Fraser 1984). The winds are calculated from the motion of ground-level diffraction patterns arising from partial-reflections from ionization in the upper regions of the atmosphere. The ionized molecules and atoms are produced, in contrast to the meteor radar, by solar radiation. This causes the performance of the medium frequency radar to depend on the time of the day. The reduced electron density during the night causes the signal to be more susceptible to noise and interference. Depending on conditions, MF measurements are available for heights from 70-105 km with a height resolution of 4 km, a temporal resolution of two minutes and a sampling rate of 3 samples per hour. Each sample contributes 3-4 points to the mean values used here. The hourly averaged MF radar winds have a statistical uncertainty of 10-25 m/s, with the higher uncertainty during night-time due to poorer ionization levels.

6.3 Data preparation

The data preparation can have a great impact on the outcome of a comparison of data sets originating from different observational methods because of differences in the sampling, heights coverage, uncertainties, etc. Wherever possible each data set should be reduced using the same computer programs. The raw wind data sets should be available in a common file format to ensure that the data can be reduced using the very same computer programs. This ensures that the potential differences found in the data sets are not due to the different data handling and difference in their statistics. However, this cannot overcome intrinsic differences in the instruments used. For instance, the sampling could, in one instrument, represent already an average of some sort while the other instruments do not average or produce a different weighted average. It is therefore necessary to be aware of how the raw data are generated, and what is being done to them to actually compare them.

The data used here were selected according to their spatial and temporal availability in all three methods. The MR is in its current setup restricted to meridional measurements. As a consequence only the meridional components of the FPS and the MF data were used in the comparison. The data were further divided into daytime and night-time periods to account for the FPS data being available only during the night. The data were averaged into hourly means as the MF did not allow for a higher time resolution. A time resolution of 1 hour represents a minimum for the FPS since the spectrometer makes only one measurement in meridional direction every 30 minutes; the data of the north and south beam of the instrument would therefore alternate in each time bin if a shorter time resolution of 30 minutes were used. The wind differences between the north and the south beam of the Fabry-Perot spectrometer can sometimes exceed 40 ms^{-1} presenting a difficulty when

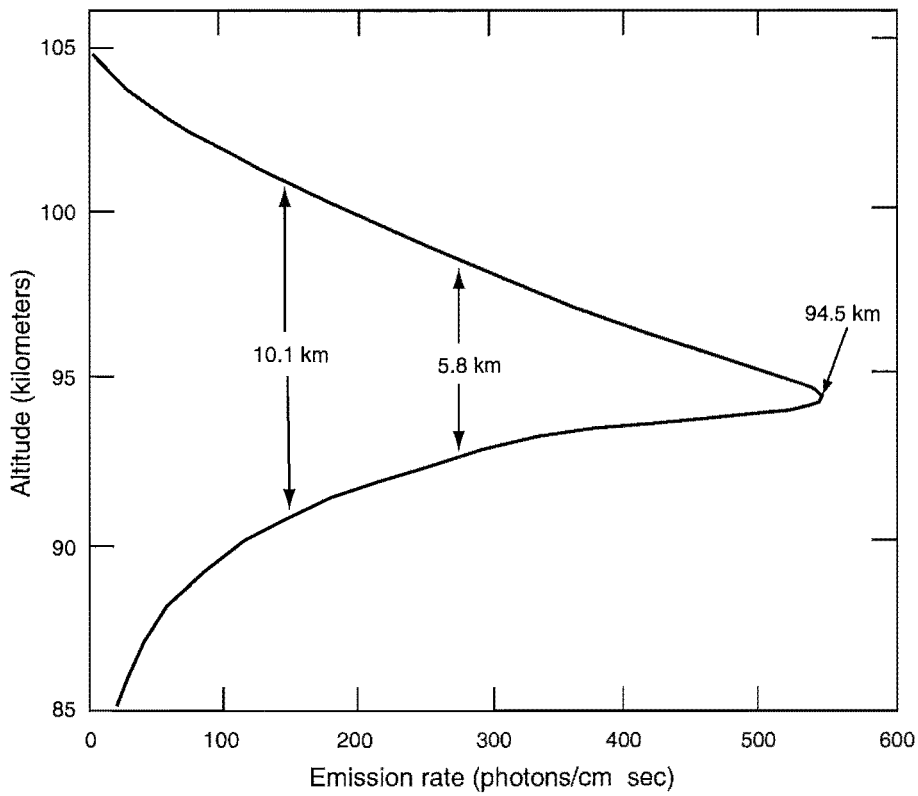

Figure 6.2: Altitude profile of emission of 557.7 nm night airglow. After O'Brien et al. (1965).

comparing these data with measurements which are not selective in their meridional direction such as the medium frequency radar. The origin of these differences are investigated in detail in 7.6.

As the FPS integrates over the sampling volume and weights the bulk motion of the molecules or atoms according to the airglow distribution the data of the MR and the MF were also averaged with a weighting function over the height range of the airglow layers. This airglow distribution has a full-width-half-maximum (FWHM) of about 6-10 km (O'Brien et al. 1965, Baker & Stair 1988).

The great variability of the shape of the airglow profile (see Baker & Stair (1988)) which can be seen in the significant profile differences between the

up and the down leg reported by rocket flights makes it impossible to know the correct airglow emission distribution for averaging the MR and MF data. It is necessary to use an average profile as a proxy. The symmetric profile (see Figure 6.2 used with the data presented in this thesis has been proposed by O'Brien (1965). The MR and MF wind data were averaged using the O'Brien profile as a weighting function to simulate the wind integration over height by the FPS. It should be noted that this averaging process is only an approximation of the FPS sampling behaviour. The instantaneous and spatially restricted sampling of the MR can not be precisely converted into the FPS sampling as the MR data is sampled at random time and at random height depending on the meteor distribution and not continuously over time and height (see Chapter 7). However, tests with different profile shapes have revealed that the results presented below are not very sensitive to the shape of the profile assumed. However, asymmetric shapes will, of course, change the reported average airglow height according to the degree of their asymmetry (see Chapter 6.4).

6.4 Determination of the Airglow Heights

In comparisons of wind measurements obtained by optical methods and by radars the question of the heights of the airglow layers has always been a weak point. Assuming a constant height for these layers is unsatisfactory if it is unknown whether or not those heights are variable over the time scale relevant for the comparison. Plagmann et al. (1998) have described two methods of deriving the airglow layer height using the wind data from a meteor radar and a optical Fabry-Perot spectrometer. The first method uses the phase of the semidiurnal tide, the strongest wind variation at these latitudes, and compares the phases measured by the two instruments. The

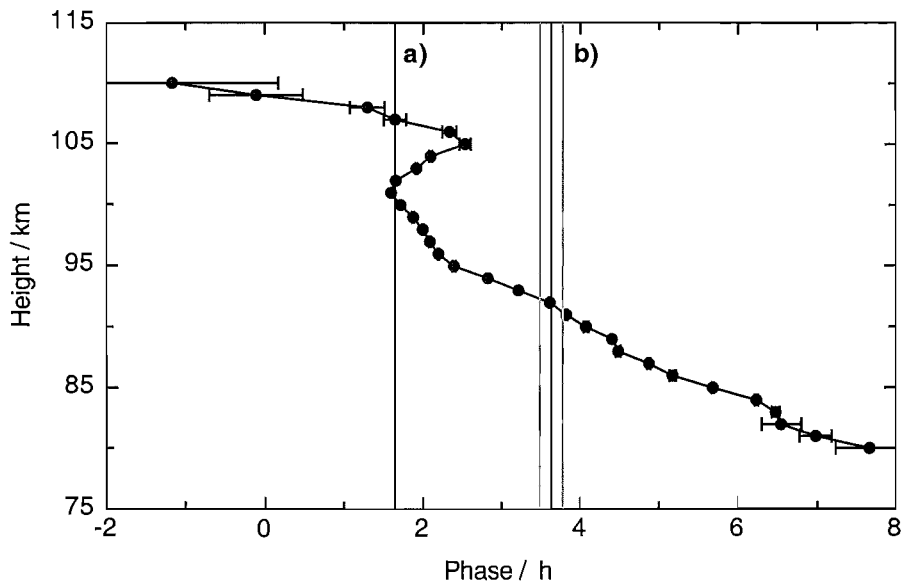

Figure 6.3: The phase of the semidiurnal tide measured by the MR on 2 May 1997 and the phase values determined from the FPS data (vertical lines) from the atomic oxygen layer (a) and the hydroxyl layer (b) for the same day

MR delivers almost continuous phase information with a resolution of 1 km in the height range between 80 and 120 km. The FPS measures the phase of the 12 hour wind variation in the two simultaneously sampled airglow layers. The heights of the airglow layer are located where the two FPS phase values agree with the phase values measured by the MR. Figure 6.3 shows the phase of the semidiurnal tide measured by the MR on 2 May 1997 and the phase values determined from the FPS data (vertical lines) from the atomic oxygen layer (a) and the hydroxyl layer (b) for the same day. The fact that there are two intercepts for the oxygen layer (a) is unsatisfactory but this ambiguity can be removed using the correlation method described below.

The phases of the semidiurnal tide in both the MR and the FPS data were determined by using the time series analysis method of Lomb (1976). This method was chosen instead of the simple Fourier analysis as the MR data can have time gaps, leading to unevenly spaced data points. These gaps occur

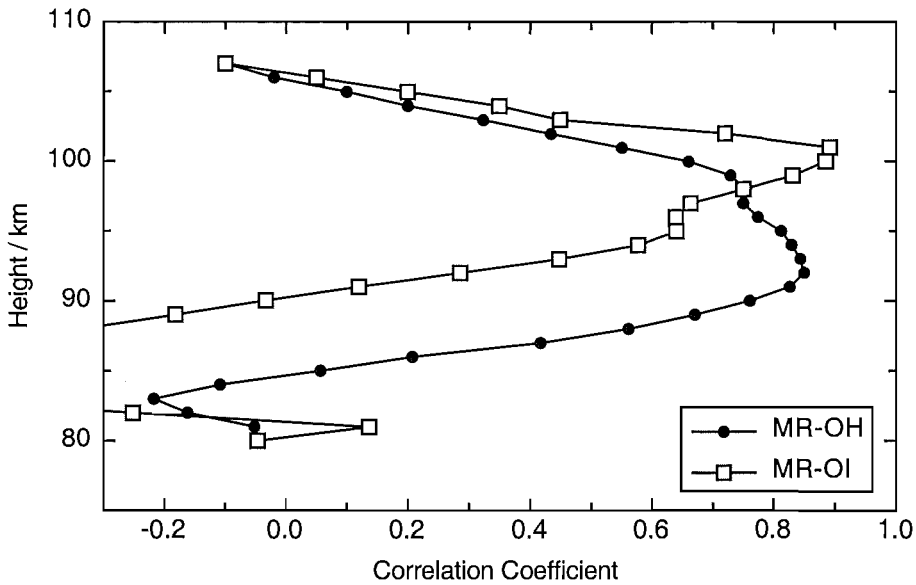

Figure 6.4: The cross-correlation coefficients of the meteor radar data and the FPS data with height for 4 May 1997

when no meteor is recorded during a time interval of one hour at a particular height.

The second suggested method for deriving the airglow heights is much simpler than the first and determines the best correlation between both data sets by varying the height of the weighting airglow emission profile on the MR determined winds until maximum correlation between these winds and the airglow winds is found. A result using data from 2 May 1997 is shown in Figure 6.4 for the atomic oxygen emission (open squares) and the hydroxyl emission (dots).

Comparing the results of the two methods displayed in Figures 6.3 and 6.4 reveals that both obtain essentially the same heights for the two airglow layers. The simpler cross-correlation method is also able to resolve height ambiguities like the one for the atomic oxygen layer shown in Figure 6.3. The cross-correlation method can furthermore be applied in cases where no

semidiurnal variation is present in the data or where not enough data points are available and therefore no phase can be calculated.

Both methods were employed, where possible, on a data set covering the period from May 1997 to April 1998. Occasionally differences of ± 2 km in the heights derived by the two methods were found. These airglow heights, which represent an important variable in the comparison, were used in the wind data comparison described below. Without the height determination a constant height for the airglow layers would have to be used which would result in a poorer agreement between the data sets.

6.5 Wind Comparison

The data preparation methods described above build the basis of the following wind data comparison. The airglow heights were determined using the methods described in 6.4. The heights were calculated using the MR winds because of the better statistics of this data compared with that of the MF data. Centered around this height the radar data were weighted using the O'Brien airglow profile (see Chapter 6.3) to calculate the hourly mean wind of the MR and MF data. This preparation is an attempt to remove the systematic differences which exist between the methods because of their different sampling properties.

Firstly a comparison will be presented which includes data from the meteor radar, the medium frequency radar, and the optical Fabry-Perot spectrometer over a period of 5 days in May 1997 as published by Plagmann et al. (1998). The period from 2 May 1997 to 6 May 1997 was chosen as it is the first consecutive period where all three instruments were operational.

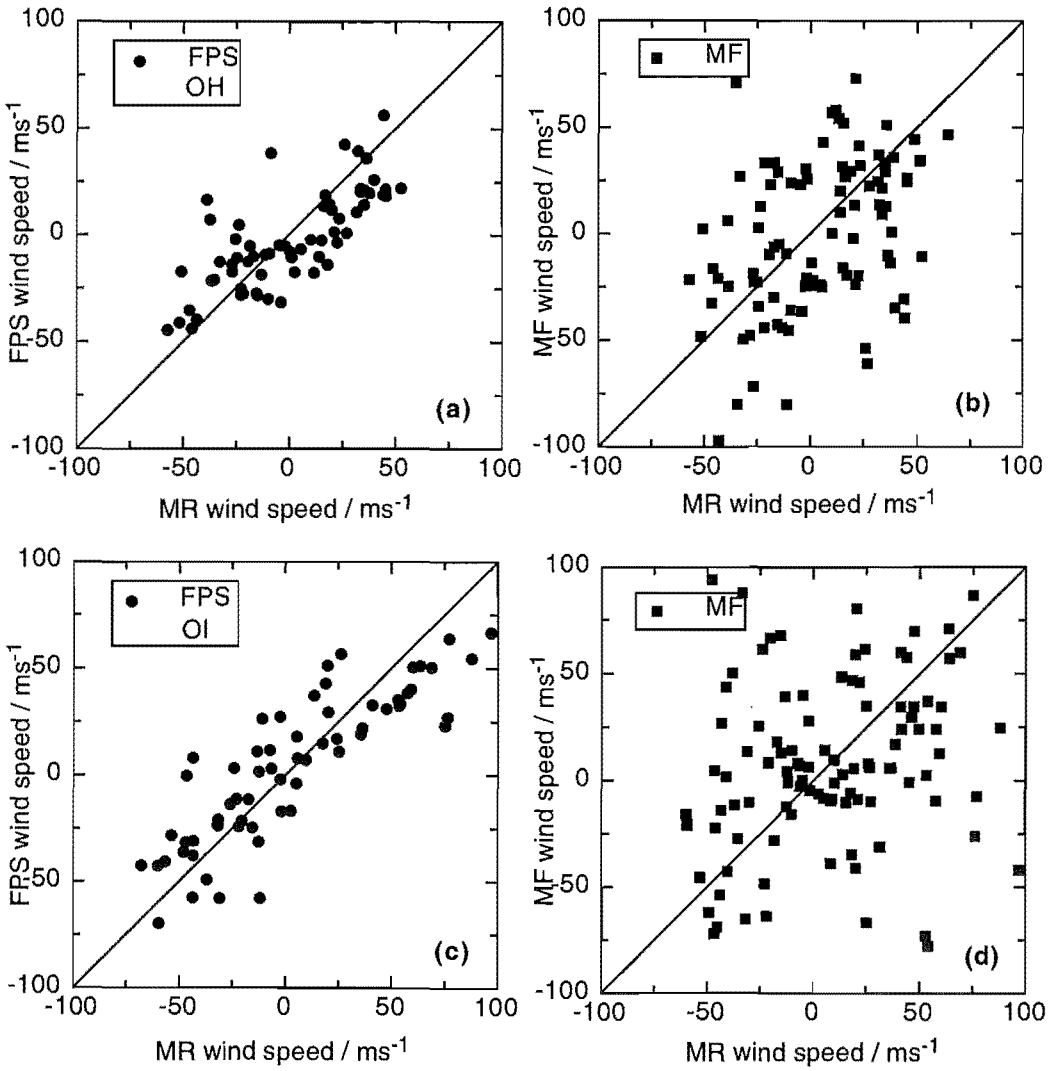

Figure 6.5: Scatterplots of both the FPS and MF hourly-averaged data against the MR hourly-averaged data for the May 2-6,1997 period. Plots (a) and (b) show the FPS and MF data for the OH height while plots (c) and (d) show the FPS and MF data for the OI height. The correlation coefficients are listed in Table 1

Date	Height (km)	MR-MF day	MR-MF all	MR-FPS
02	93	0.56	NS	0.85
	101	NS	NS	0.89
03	94	0.80	NS	0.86
	103	0.58	NS	0.90
04	93	0.82	0.71	0.95
	102	0.63	0.57	0.89
05	93	NS	NS	0.89
	98	NS	NS	0.86
06	97	NS	NS	0.84
	98	NS	0.56	0.93
all	lower	0.82	0.63	0.95
	higher	0.61	NS	0.85

Table 6.1: Cross-correlation coefficients for individual days. The column 'Day' is daytime-only data while the column 'all' refers to the whole day data. The last pair of rows contains the coefficients for the superposed epoch hourly data for May 2-6, 1997 in Figure 6.5. 'Lower' refers to the hydroxyl height, while 'higher' refers to the atomic oxygen height for each day. Correlations below the 95% significance level are abbreviated as 'NS'.

The results of the comparison are shown in Figure 6.5 for the period 2-6 May 1997. Panels a) and c) display the meteor radar data against the FPS wind data for the OH and OI emissions, respectively. The results of the comparison between the radars are also given in Figure 6.5, panels b) and d), at the same heights where maximum correlation was found for the OI and OH results. The quantitative results of the comparison finding the best fit slope to the data are given in Table 6.1.

Figure 6.6 presents the wind data of the individual days measured during the period from 2 May 1997 to 6 May 1997 at the height of the hydroxyl layer (Panels a-e). Panel f) shows the data of the generic day which encompasses

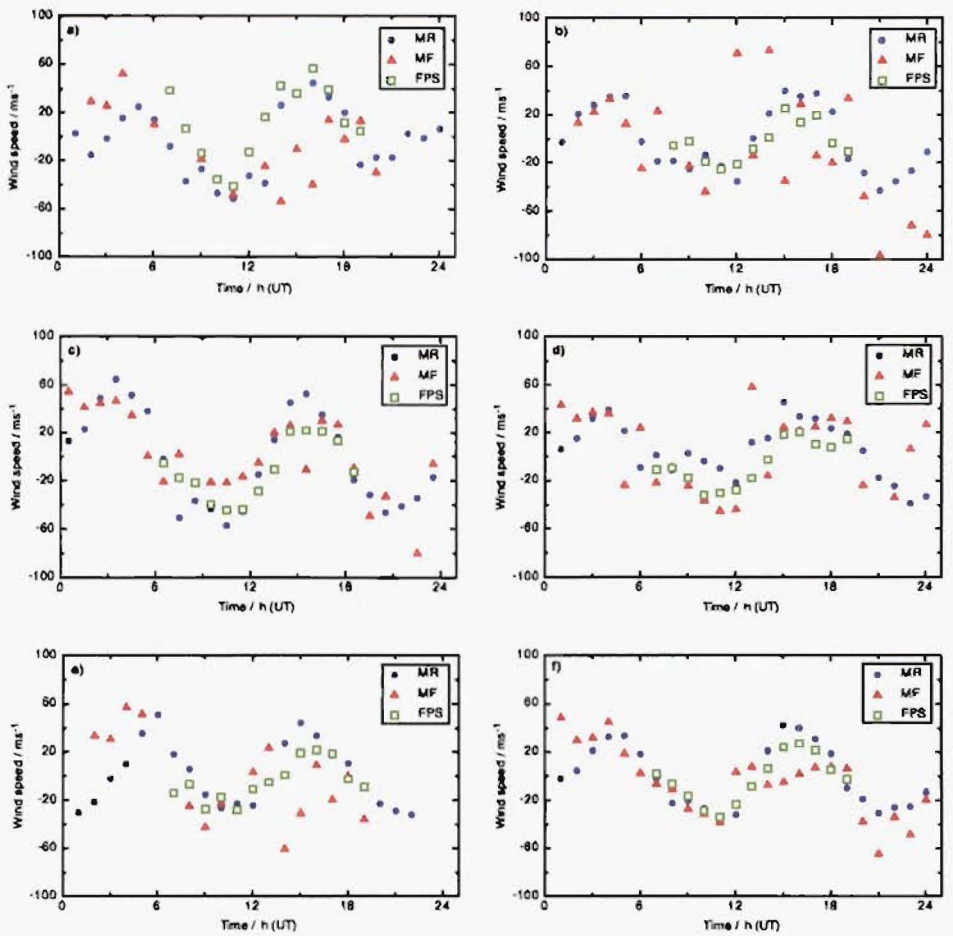

Figure 6.6: The meteor radar (blue), the medium frequency radar (red), and the Fabry-Perot spectrometer (green) wind data, measured at the height of the OH-layer, from 2 May 1997 (Panel a) to 6 May 1997 (Panel e). Panel f shows the data of the generic day which encompasses the data of all 5 days for each instrument.

the data of all 5 days for each instrument at the height at which the OH emission shows maximum correlation. The correlation coefficients for this six-day average are summarized in Table 6.1.

Figure 6.6 shows the wind data of the individual days at the height of the atomic oxygen layer (Panel a-e). Panel f) shows here gain a generic day with the superposed epoch hourly-averaged winds over all 5 days for the height at which the atomic oxygen emission shows maximum correlation.

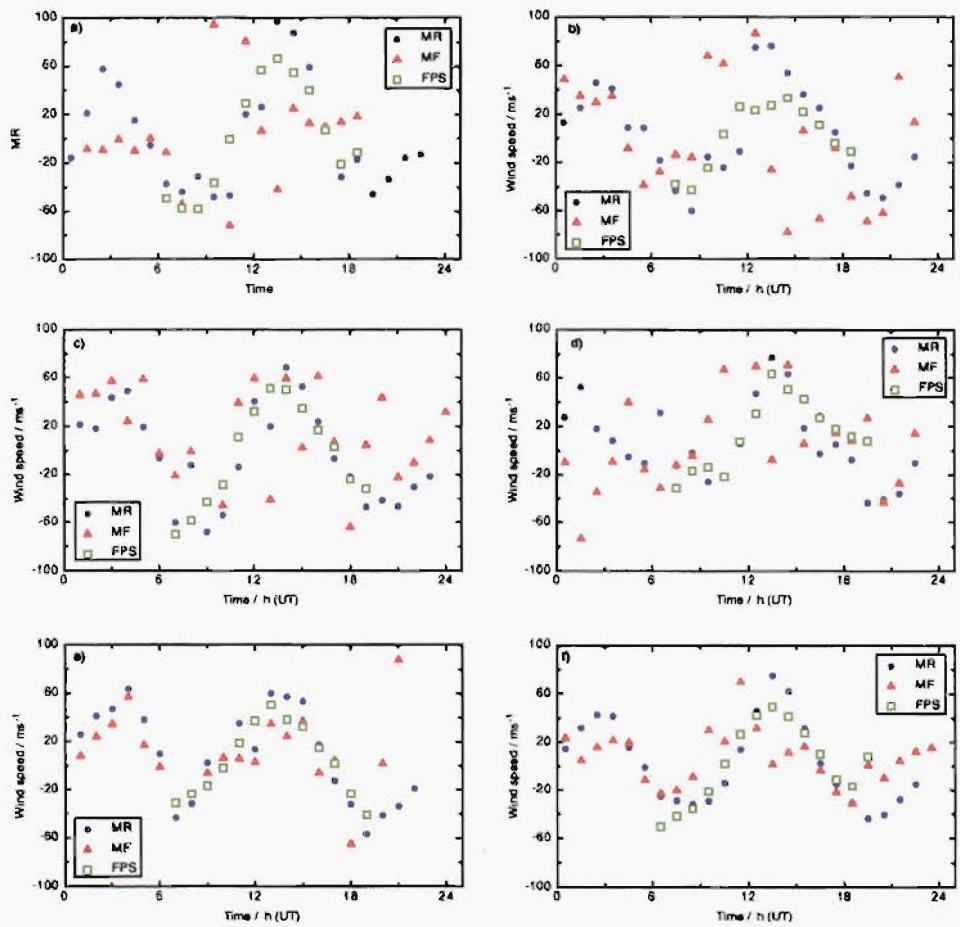

Figure 6.7: The meteor radar (blue), the medium frequency radar (red), and the Fabry-Perot spectrometer (green) wind data, measured at the height of the atomic oxygen layer, from 2 May 1997 (Panel a) to 6 May 1997 (Panel e). Panel f shows the data of the generic day which encompasses the data of all 5 days for each instrument.

The result of the comparison amongst the three methods show better agreement between the FPS and the MR winds than between either the FPS or the MR winds and the MF winds, as shown in Table 6.1. This difference most likely arises because of the larger uncertainties of determination of the MF winds, in particular at night.

The agreement between the MR and the FPS wind determinations is quite good (correlation coefficient near 0.9, as given in Table 6.1) indicating that both methods indeed detect the same motion. These results enable one to obtain nightly height information for the airglow layers by both direct wind correlation as well as using the phase of the strongest oscillatory component present in the MR and FPS data. The MR and MF comparisons usually show a greater variability at the height of the OI airglow layer as both radars receive fewer echoes than at the lower height of the OH airglow layer. This also has an influence on the lower correlation coefficient found for the MR-MF and the MR-FPS correlation at the OI height.

The hourly-averaged MF data is often too noisy when used on a day-by-day basis. During the night the MF data is often affected by interference which, coupled with lower ionization, leads to a lower data rate and poorer signal to noise ratio, typically 20 dB worse than during daytime (see S. Smith (1996) for details). However, comparing the MF and MR daytime data yields good results on some days, especially for the lower height (see Figures 6.6 and 6.7). Therefore, longer averages or higher sampling rates for the MF winds will be expected to give better correlation.

As a consequence of the above result the forthcoming comparison which aims to determine the monthly averaged heights of the airglow layers use will only the MR data and the FPS data.

The MR data and FPS data were reduced using the same technique as de-

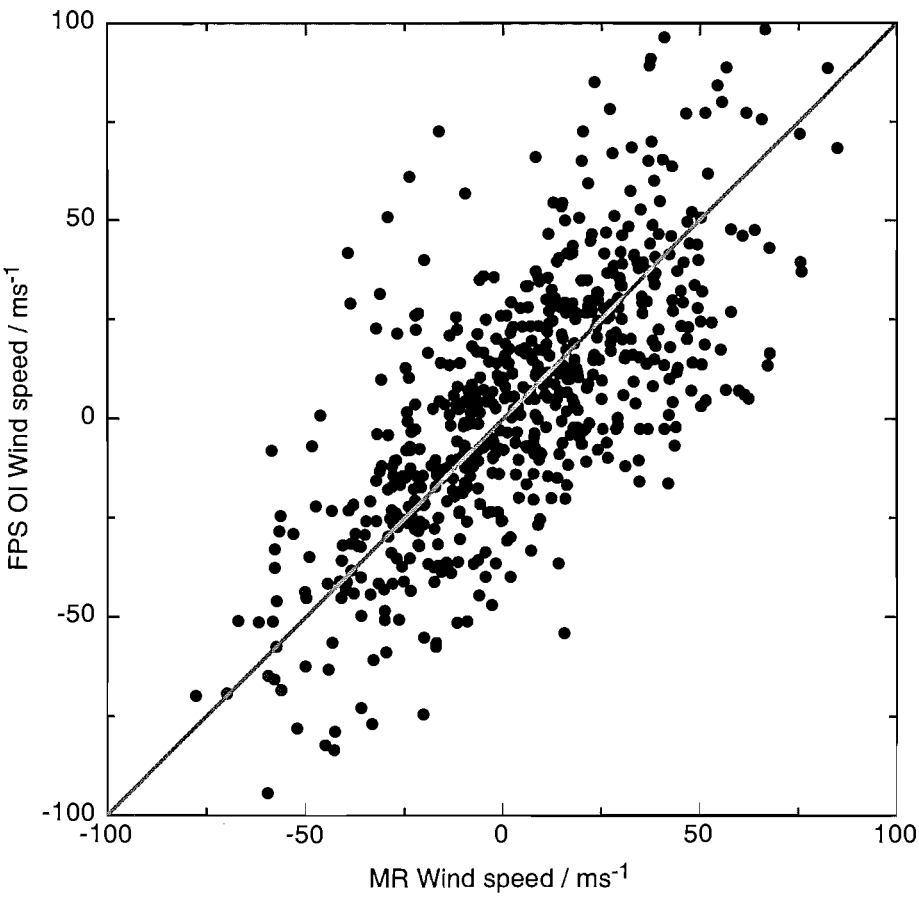

Figure 6.8: The scatterplot of the meteor radar wind data and the FPS OI wind data which includes all simultaneous data measured during the period from May 1997 to April 1998. The straight line denotes a 1:1 correspondence. The correlation coefficient $r = 0.71$.

scribed above. The MR was operational for almost the whole period encompassing May 1997 to April 1998. The amount of available data was therefore only restricted by the availability of the FPS data due to weather conditions and geomagnetic activity (see Chapter 4). A total of 80 data sets are available for the comparison.

Figure 6.8 and Figure 6.9 show the scatterplots of the atomic oxygen and the hydroxyl emission data, respectively. The obtained correlation coefficients r = 0.71 for the meteor radar data and the FPS OI data and r = 0.68 for the

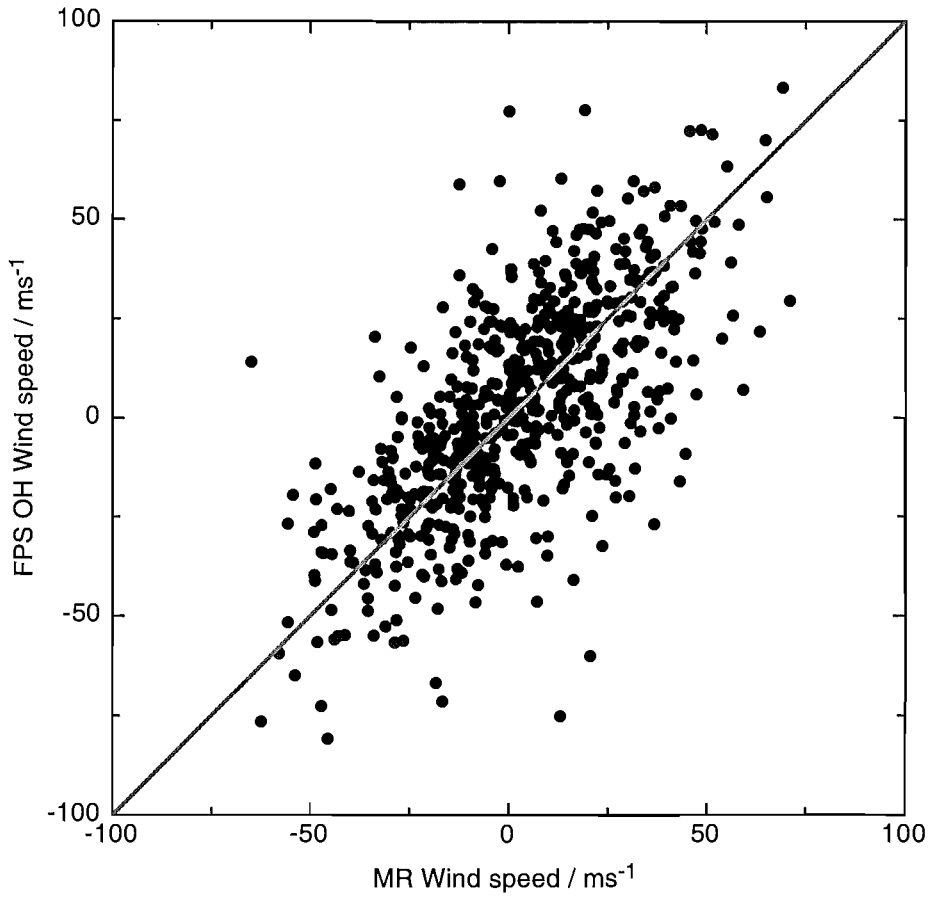

Figure 6.9: The scatterplot of the meteor radar wind data and the FPS OH wind data which includes all simultaneous data measured during the period from May 1997 to April 1998. The straight line denotes a 1:1 correspondence. The correlation coefficient $r = 0.68$.

meteor radar data and the FPS OH data. Both coefficients are statistically significant to the 99.9 % level.

The Figures 6.10, 6.11, 6.12 and 6.13 show example wind data from the meteor radar (blue) and the Fabry-Perot spectrometer (red) for the OI emission (6.10, 6.11) and the OH emission (6.12, 6.13).

These Figures show that the data agrees in general, but occasionally the wind compares poorly between the meteor radar and the Fabry-Perot spectrometer. The poorer correlation can be caused by thin tropospheric clouds such

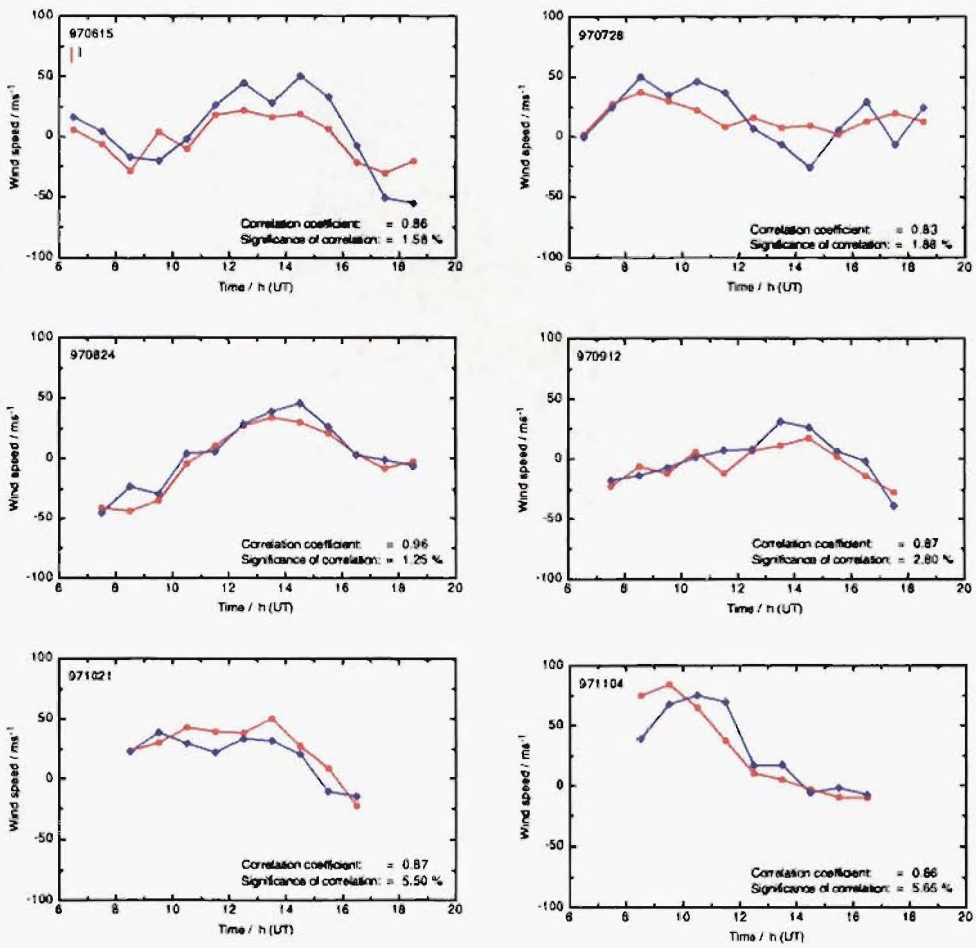

Figure 6.10: Examples of the meteor radar wind data (blue) and the FPS OI wind data (red) from June 1997 to November 1997. The dates are shown in the upper left corner of each panel. The correlation coefficients are shown in the lower right of each panel. The significance corresponds to the probability that the correlation would occur by chance. The top left panel shows lines that represent the 2σ uncertainties of the winds.

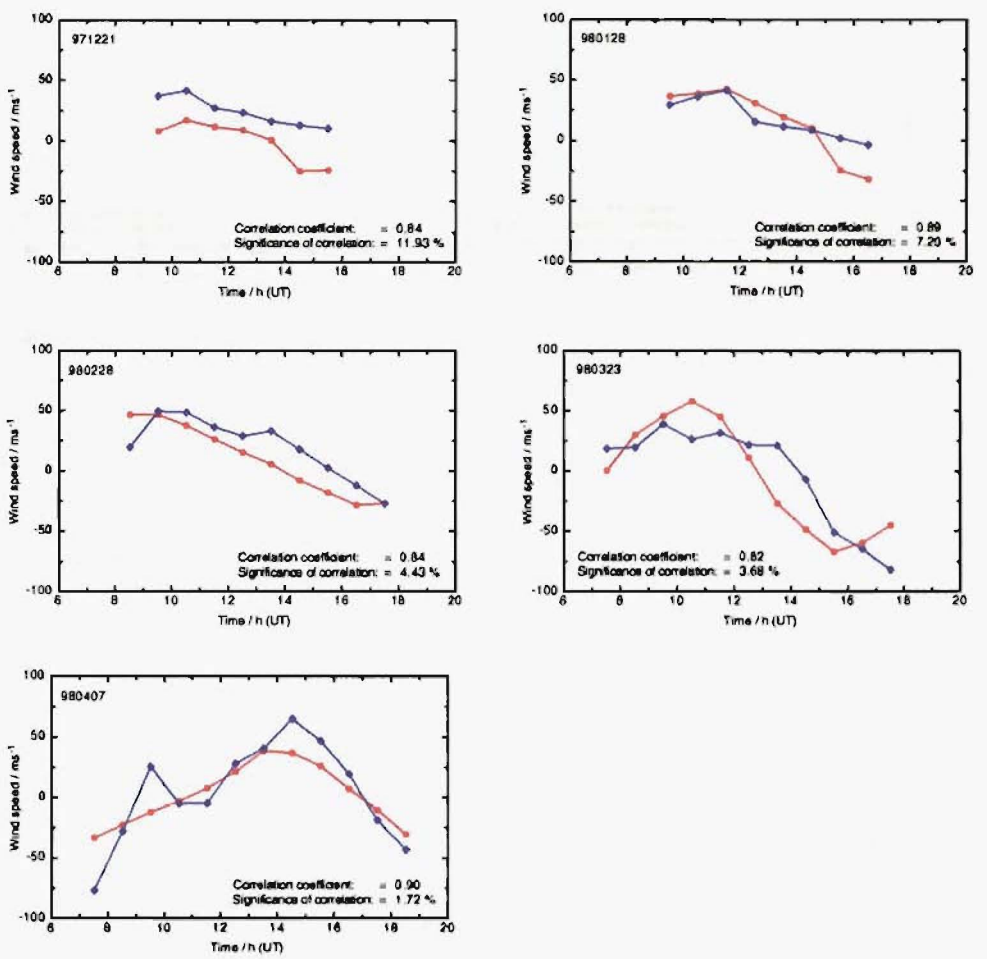

Figure 6.11: Examples of the meteor radar wind data (blue) and the FPS OI wind data (red) from December 1997 to April 1998. The dates are shown in the upper left corner of each panel. The correlation coefficients are shown in the lower right of each panel. The significance corresponds to the probability that the correlation would occur by chance.

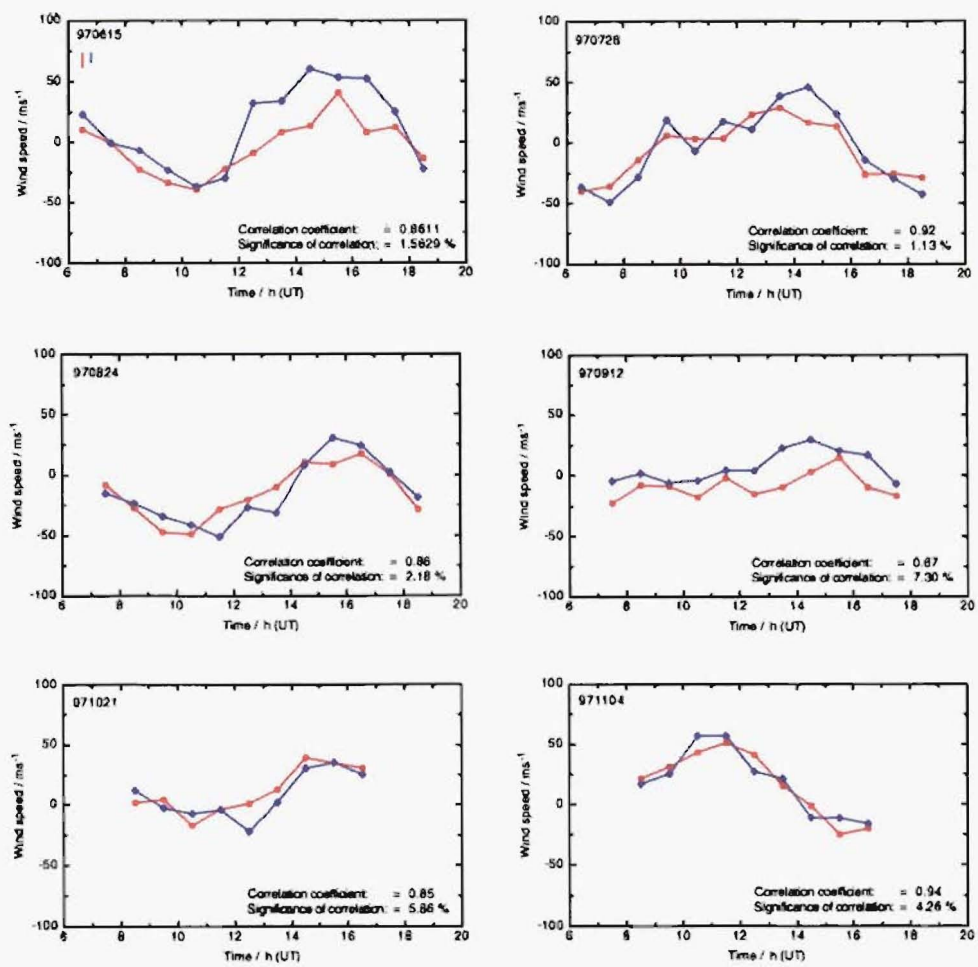

Figure 6.12: Examples of the meteor radar wind data (blue) and the FPS OH wind data (red) from June 1997 to November 1997. The dates are shown in the upper left corner of each panel. The correlation coefficients are shown in the lower right of each panel. The significance corresponds to the probability that the correlation would occur by chance. The top left panel shows lines that represent the 2σ uncertainties of the winds

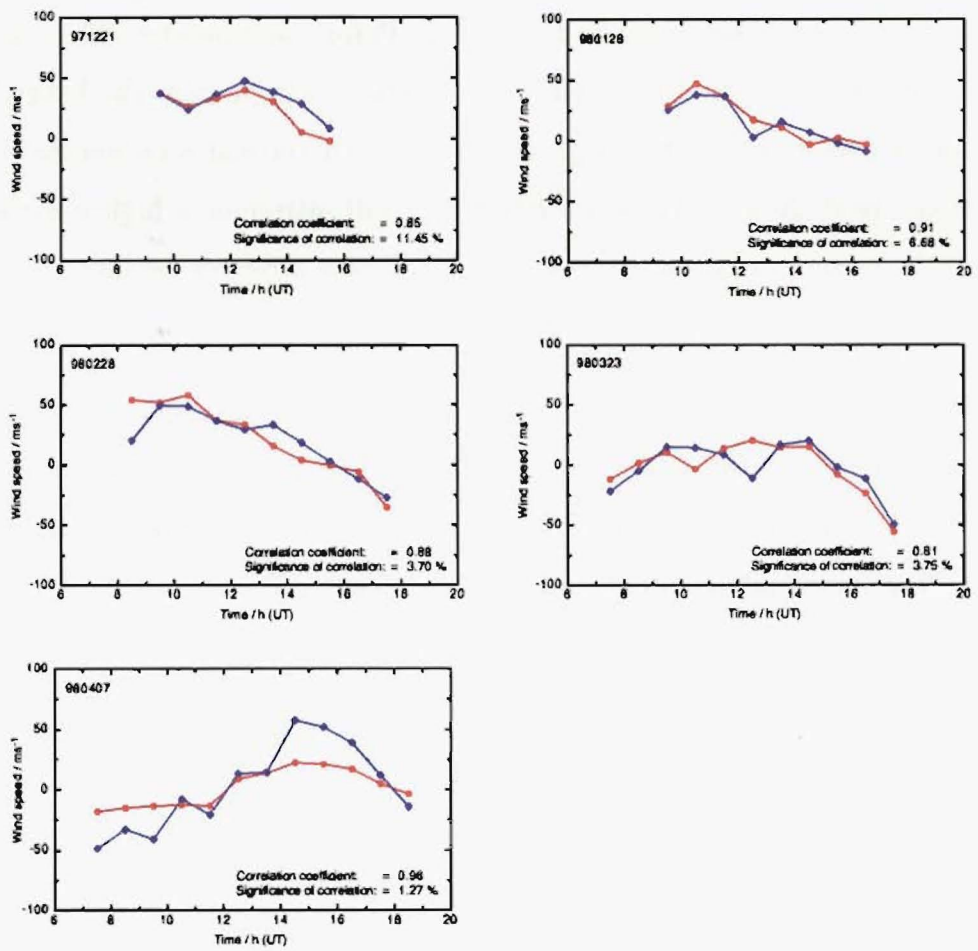

Figure 6.13: Examples of the meteor radar wind data (blue) and the FPS OH wind data (red) from December 1997 to April 1998. The dates are shown in the upper left corner of each panel. The correlation coefficients are shown in the lower right of each panel. The significance corresponds to the probability that the correlation would occur by chance.

as cirrus clouds which would compromise the optical data in such a way that the derived wind speed would detect the speed of the clouds rather than the wind speed in the airglow layer. Another, more likely reason is a stronger gravity wave activity during the nights which show a poor wind correlation between the meteor radar and the Fabry-Perot spectrometer. These gravity waves will affect almost exclusively the meteor radar data as the Fabry-Perot spectrometer cannot detect gravity waves with vertical wavelengths shorter than about 20 km. These gravity waves will introduce a higher variability in the meteor radar data will as a result show a stronger deviation from the semidiurnal wind pattern.

In summary, the meteor radar wind and the optical Fabry-Perot spectrometer wind show a good agreement and both method appear to detect similar air motion. The possible causes of the poor correlation of the wind data, detected during some nights, will be addressed in Chapter 7.

6.6 Airglow Height Variation During a Year

Ground based airglow measurements carried out to date lacked one important detail: the height of the airglow layer. The heights and vertical structure of airglow layers have been measured by rocket flights (see Section 2.3). Today orbiting satellites are used to study the various airglow layers in the atmosphere (see Section 2.3). These instruments are able to measure the peak height of the airglow emission profiles during their flight. The disadvantage of these methods are that the rocket flights are very expensive and the data will only be gathered from a relatively small volume. The satellite based instruments cover almost the whole atmosphere but need about a month to collect a whole day's worth of data for a given longitude and sample with a deep view through the layer on a limb.

The good result in the comparison of the meteor radar winds with the Fabry-Perot spectrometer winds gives the opportunity to determine the heights of the atomic oxygen layer and the hydroxyl layer. However, with the data available only a single nightly averaged height can be obtained for each 24-hour period as the variability of the individual data points is too high. This temporal resolution however is sufficient to calculate a monthly average of the OI and OH airglow heights over a year (here from May 1997 to April 1998).

Figure 6.14 show the monthly averaged OI and OH airglow layer height for one year, encompassing May 1997 to April 1998 as published by Plagmann et al. (1998). The uncertainties shown reflect the spread of the height variation found in each month. The heights were obtained by employing the symmetric O'Brien et al. profile used in weighting the meteor radar winds. The heights presented here were calculated using the correlation method described in Section 6.4. The phase match method was not employed as it is not

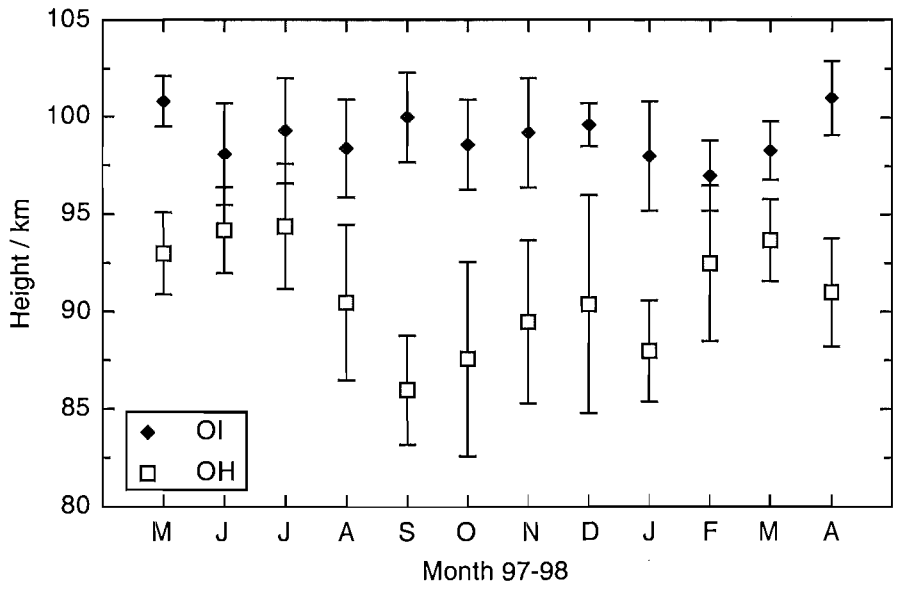

Figure 6.14: Monthly average of the OI and OH layer height for one year, encompassing May 1997 to April 1998. The errorbars represent the standard deviation of the heights for each month. (From Plagmann et al. (1998).

possible to calculate a meaningful semidiurnal phase from the data obtained during the short summer nights. Tests show that the height results are not very sensitive to the shape of the airglow profile assumed. For instance a simple triangle profile does not change the reported airglow heights. However, strongly asymmetric profiles will have an effect on the airglow heights and might have an influence on the amplitude of the OH height variability observed in Figure 6.14. Current information on the airglow profile and its variability is too limited to justify the use of an asymmetric profile for the present correlation study.

6.7 Conclusion

The results of the first part of the comparison has been discussed by Plagmann et al. (1998). The meteor radar and the Fabry-Perot spectrometer

agree in their wind findings remarkable well and appear to obtain similar results. The medium frequency radar winds do not compare as well with the result of the other two methods. A reason for this can be found in the low signal to noise ratio of the medium frequency radar during the night. Other reasons might lie in the different sampling. The medium frequency radar samples directly overhead while the meteor radar samples to the north and south from the home site. The meteor radar data is obtained by averaging over the northern and southern sampling volumes, the medium frequency radar has only one sampling volume and might therefore pick up a different 'mean' wind. Furthermore the statistical sampling makes the MR appear to obtain "better" results because of its higher sampling rate (see Chapter 7). However, during the daytime the meteor radar and the medium frequency radar data show good agreement on some days.

The very good correlation observed between the Fabry-Perot spectrometer and the meteor radar winds for the 5 consecutive days was also found, albeit to a lesser degree, in the complete yearly data set of 80 days (May 1997 to April 1998). The scatterplots of Figure 6.8 and Figure 6.9 show a greater spread which results in the lower correlation coefficients for the OI data with $r = 0.71$ and for the OH layer with $r = 0.68$. These correlation coefficients are significant to the 99.9% level.

A reason for the differences in the correlation coefficients between the May data and the whole year data could have its cause in different gravity wave activities during both periods. Low gravity wave activity, leading to only weak small-scale disturbances of the mean flow, would decrease the variance of the meteor radar data. The wind data measured by Fabry-Perot spectrometer would be more smoothly following the semidiurnal tide. An increase of the gravity wave activity would on the other hand increase the variance of the meteor radar data but would have very little effect on the Fabry-Perot

spectrometer data, resulting in a decreased correlation between the two data sets. This gravity wave noise cannot be totally removed by averaging the meteor radar data as the meteor radar 'sees' only a fraction of those waves at the moment of the meteor event in a small volume while the Fabry-Perot spectrometer 'sees' the wave as a whole and smoothes it out. This tendency of the Fabry-Perot spectrometer to low-pass filter wave motions is described in detail in Chapter 7. However, Figures 6.10 to 6.13 show that during the nights with low gravity wave activity both methods detect the same overall air motion on a hourly mean basis.

Although the heights found here for the airglow layers are higher than the typical peak height quoted in the literature, these heights are within the range of peak heights mentioned by Baker & Stair (1988). Not knowing the correct airglow emission distributions with height for our observations, and using the O'Brien profile as a proxy for them, can easily lead to some discrepancy in the heights reported here and the peak heights reported by direct measurements (Baker & Stair 1988, Hernandez et al. 1995). Simultaneous airglow layer profile measurements from a satellite would clarify the present uncertainty. There are no measurements available from WINDII on the UARS satellite for the period of time discussed here. The uncertainties in our reported height measurements arise from a combination of the natural fluctuation of the atmosphere and instrumental uncertainties.

The variations in emission height during the year, shown in Figure 6.14, should not be too strongly affected by small changes in the emission distribution of the airglow layer with height as a function of time. The highlight of this figure is the rather large variation in the height of the OH emission, when compared with the rather constant OI emission height. Unless there are profound changes in the OH airglow layer profile throughout the year, the observed 9 km height change of this OH emission during the year indicates a

change in the height at which this OH emission occurs. Other evidence (She & VonZahn 1998) shows that the height of the mesopause changes dramatically during the year. During the winter She and VonZahn have found the height of the mesopause is near 100 km and near 88 km during the summer, which is in rather good agreement with the observed height changes for the OH shown in Figure 6.14, implying a close relationship between the height of the mesopause and the OH emission layer height. This height variability will have an impact on the photochemistry of the OH molecule (see Section 2.3) as the production rate of OH depends on the diffusion of atomic oxygen or ozone from the thermosphere above. A lower altitude will also increase the quenching rate of the emission as the density of possible quenchers will increase and the mean free path length decreases this is supported by Takahashi et al. (1995) who reported a semi-annual oscillation of the upper mesospheric OH airglow intensity. The temperature at upper mesospheric heights is lower in summer and higher which will have an impact on the mean free path length as well as on the kinetic of the chemical reactions which form the OH layer.

Chapter 7

Detectability of Gravity Waves in FPS Wind Measurements

7.1 Introduction

Experimental science depends on the instruments and experimental setups employed to measure the quantity of interest. The quality of the measurements can only be assessed if the sampling properties of the instrument are established. Otherwise it is unknown if the instrument measures the true value of the quantity or if it over or under estimates it. The absence of a certain effect may then just be due to the inability of the setup to detect it. Both random error and systematic error have an influence on the result of a measurement. The random error is ubiquitous and accompanies every measurement. It cannot be removed, it can only be minimized using statistical methods. The systematic error on the other hand is a constant deviation from the true value. This deviation has its origin in the instrument used in the measurement. The instrument is baised and constantly over or underes-

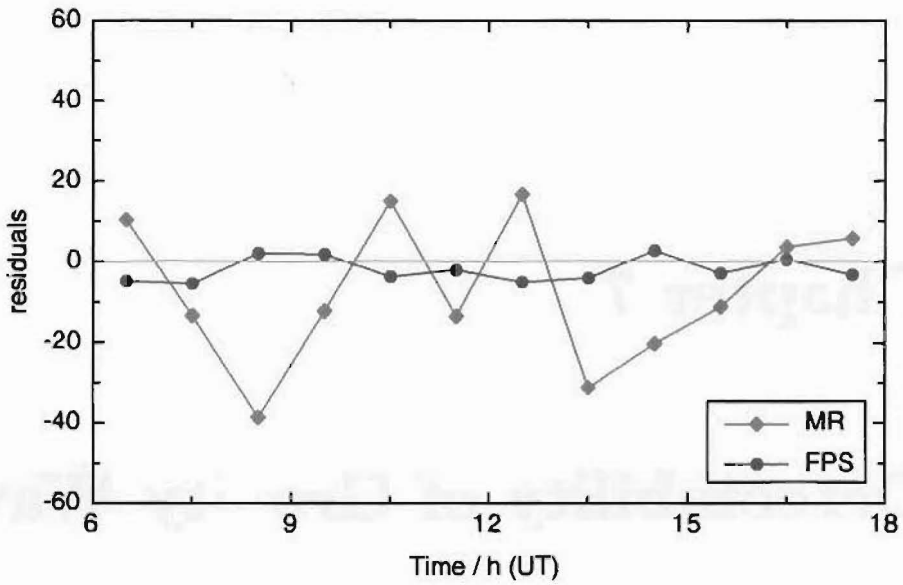

Figure 7.1: Variability in the meteor radar (red diamonds) and the Fabry-Perot spectrometer wind (blue dots) after subtracting the mean wind and the semi-diurnal tide.

timates the true value of a measurement. As this deviation is constant it can be, once it is known, removed. Known systematic deviations from the true value need to be corrected for or have to be accounted for in the uncertainties of the results. It is therefore important to know as exactly as possible what the observational limits of the employed setup or instrument are.

The comparison between a meteor radar and a Fabry-Perot spectrometer described in the preceding Chapter 6 revealed a very good agreement between the FPS and the meteor radar hourly mean winds. However a closer look at the hourly variances shown in Figure 7.1 reveals differences between the two methods which can not originate solely from the distinction of the sampling volumes of both instruments, otherwise the numerical variances would be expected to be about equal. Hence part of the differences must arise from differences in the observation methods employed.

This chapter will attempt to show that the differences between the two

datasets in Figure 7.1 are not originating from noise in the MR data but arise from a systematic difference in the sampling properties of the two instruments. The sampling properties of the Fabry-Perot spectrometer make it unable to detect high-frequency wind variations while the sampling of the meteor radar is able to detect them. The high resolution Fabry-Perot spectrometer used to obtain the data would able to measure high-frequency wind variations the restrictions described in this chapter arise from the airglow intensity which determines the integration time and arise from the width of the airglow layers under investigation which resticts the spacial sampling of the wind profile. This implies that other techniques which also sample airglow will face similar restrictions. When reference is made to the Fabry-Perot spectrometer in this chapter it could be replaced by other airglow sampling techniques.

To lay the foundation for the following sections in this chapter a short summary of the wind determination of the FPS (see Chapter 3) and the airglow layer (see Section 2.3) will be presented in Section 7.2. In order to model a physical system or a certain part of that system a mathematical description is necessary which describes the properties of that system. An analytical model of the sampling behaviour of the Fabry-Perot spectrometer will be developed in Section 7.3. This model describes the observational limits of the instrument with respect to the ability to detect high-frequency wind variations. This analytical model can then be used to simulate how the Fabry-Perot spectrometer samples the atmosphere. A numerical model will therefore be developed in Section 7.4 which models the sampling behaviour of the Fabry-Perot spectrometer and the gravity wave activity in the mesopause, lower thermosphere region. As the Fabry-Perot spectrometer is also able to determine the kinetic temperature in the airglow layers it appears worthwhile to investigate in Section 7.5 what effect a nonhomogenuos wind distribution

in the airglow layer has on the measured temperature. As the observational limits of the Fabry-Perot spectrometer have been characterised it is interesting to see if wind variations well inside the detectable part of the spectrum can be found in the available data sets. In Section 7.6 an example data set will be presented that shows that the instrument is able to detect very long horizontal gravity waves which were not so easily detectable without the described lowpass filtering of wind variations.

7.2 Wind Determination using a Fabry-Perot Spectrometer

A detailed description of the principle of wind measurements using the Fabry-Perot spectrometer has been discussed in Chapter 3. In the following Sections (7.2, 7.3, 7.4) the description is given with particular attention to the ability of the instrument to detect vertical wind variations.

The FPS measures wind in an airglow layer of the atmosphere by detecting the spectral Doppler shift of atomic or molecular transitions. It column integrates the resulting emission of these transition over the depth of the airglow layer. With the pressure and temperatures found in the atmosphere at mesospheric and lower thermospheric heights these emissions are Doppler broadened. The spectral emission lines of the excited molecules or atoms which are used to determine the wind and temperature result in a Gaussian profile [1] in the recorded spectrum. The wind in the airglow layer is deter-

[1] In the following text the term profile is used in two contexts: The airglow layer profile which is the density distribution of the emitting species in the atmosphere, and the emission profile which is the spectral emission distribution produced by the motion of the emitting species in the recorded spectrum.

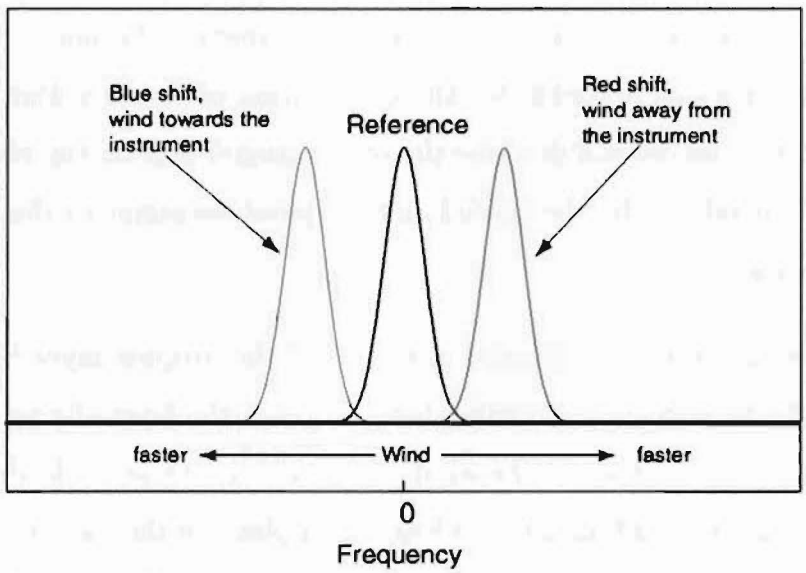

Figure 7.2: Schematic of the shift of the emission profile in the recorded spectrum. Wind blowing towards the instrument causes the emission to be blue shifted, wind away from the instrument results in a red shift. The stronger the wind the greater the distance between the shifted profile and the reference.

mined by measuring the Doppler shift of these Gaussian profiles against a "zero wind" reference. This reference is obtained by measuring in the zenith direction assuming that the vertical wind is negligible compared with the horizontal wind. Figure 7.2 shows red and blue shifted emission profiles representing a wind blowing towards and away from the instrument, respectively. The greater the wind speed the greater the distance to the reference profile.

7.3 Mathematical description of the Observational Limits

The features of the airglow measurement which have most impact on the wind determination are the depth of the airglow layer (see Section 2.3) and the integration time of the measurement. This section discusses the effect

of these features on the FPS wind measurements. An analytical model is developed which accounts for the distribution of winds within the airglow layer. This model will describe the observational bias on the wind measurements introduced by the spatial and temporal averaging of the Fabry-Perot spectrometer.

For the analytical description a model of the airglow layer height profile is used which weights the wind distribution in the layer. Using a sinusodial wave function to describe the wind distribution in the layer the dependence of the detected amplitude on wavelength and phase of the wave is investigated. The dependence of the detected amplitude on the phase speed of the wave is included. The results of this investigation will be presented in the context of the known gravity wave activity obtained by other instruments in the mesopause, lower thermosphere region.

The actual shape of the airglow emission profile is highly variable (Baker & Stair 1988) and deviates from the theoretical Chapman profile as this theory assumes a motionless atmosphere with a constant absorbtion coefficient. A good approximation of the height profile of the hydroxyl and atomic oxygen airglow layer is a Gaussian function $G(h)$ with a full width at half maximum of about 10 km (see Section 2.3 for more details). Assuming this function as a proxy of the airglow layer height profile allows a mathematical analysis of the Fabry-Perot spectrometer wind sampling properties. The Gaussian function $G(h)$ depends on the height h and on the constant $\sigma^2 = \frac{h_w^2}{2 \ln 2}$ where h_w represents the half width at half maximum of the airglow layer.

$$G(h) = \frac{1}{\sqrt{\pi}\sigma} e^{-\frac{h^2}{2\sigma^2}} \tag{7.1}$$

The intensity of the emission profiles of the wind distribution in the layer is therefore weighted by this Gaussian profile $G(h)$. Wind measurements origi-

nating from the edge of the emission profile will consequently contribute less to the wind determination than measurements originating from the centre. As the layer is not indefinitely thin and the FPS integrates over the width of the layer the measured shift of the emission profile represents the average wind speed in the layer weighted by this profile. The instrument will consequently underestimate the wind speed of for example, any sinusoidal wind speed distributions such as tides and gravity waves as long as the vertical wave length of those waves are smaller or about the same as the FWHM of the airglow layer profile. Figure 7.3 (panel 1) shows examples of a cosine function with wavelengths of 0.5, 1, and 2 times the layer profile width here approximated by a top hat function for simplicity.

Each individual volume in the layer emits the light of the molecular or atomic spectral emission profile into the FPS at a position which represents the speed of the bulk motion of these molecules. This results in the summation of many spectral profiles spread over a region in the recorded spectrum representing the wind speed variance in the layer, the Figure 7.3 illustrates the fact that spectral emission profiles are spread over greater regions in the recorded spectrum when the wavelength of the associated wave is shorter. This sum of Gaussian spectral emission profiles in the recorded spectrum will result in a profile which has a distance to the reference profile that represents the mean wind in the layer weighted by the airglow layer profile. Multiplying the weighting function in Equation 7.1 with a cosine function representing the wind speed distribution in the airglow layer yields

$$D(h, m, \phi) = \frac{1}{\sqrt{\pi}\sigma} e^{-\frac{h^2}{2\sigma^2}} \cos(m(h - \phi)) \tag{7.2}$$

This equation describes the weighted emission profile distribution in the recorded spectrum of the FPS. It therefore represents the wind speed distribution in the airglow layer as seen by the Fabry-Perot spectrometer. The

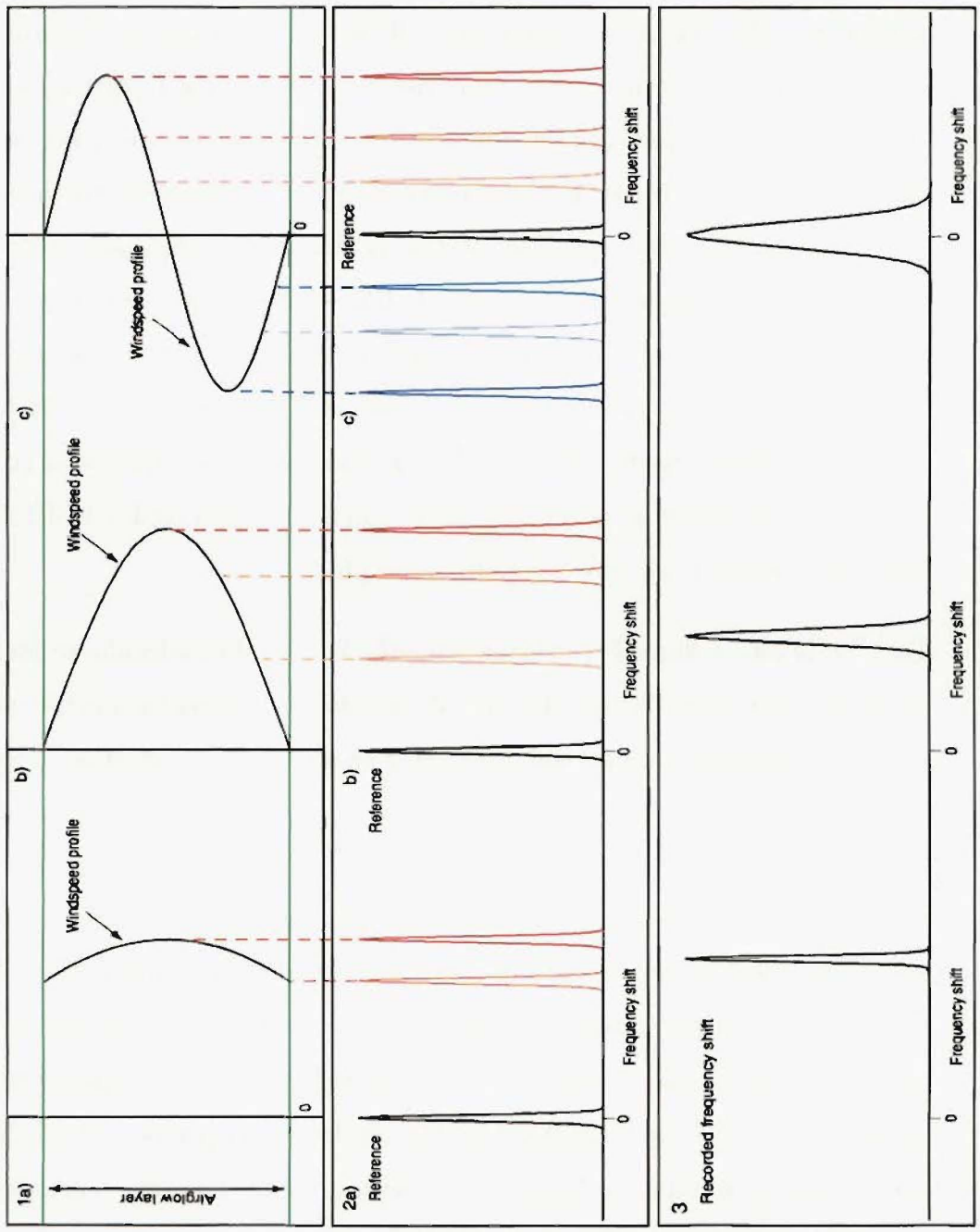

Figure 7.3: The recorded positions of the emission profiles in the spectrum, which represent the windspeed, originating from a wave with wavelengths of 2 (a), 1 (b), and 0.5 (c) times the width of the atmospheric airglow layer (here a top hat profile for simplicity) are shown in Panel 1. The instrument sums over the emission profile. A non-constant wind in the airglow layer will therefore spread the emission profile in the recorded spectrum. Panel 2 schematically shows a few profile positions in the spectrum. The sum of these individual profiles, which are the resulting positions of the profiles as seen by the FPS, are shown in Panel 3.

function $D(h, m, \phi)$ depends on the height h in the layer, the wavenumber m, and the phase ϕ of the wave. The width of the weighting function σ is set constant. Integrating this equation (see Gradshteyn & Ryzhik (1965)) over height h results in a function $\Psi(m, \phi)$ which describes the detected relative wind speed depending on the wavenumber and wave phase in the airglow layer.

$$\Psi(m, \phi) = \int_{-\infty}^{\infty} D(h, m, \phi) dh = \sqrt{2} e^{-\frac{m^2 \sigma^2}{2}} \cos(m\phi) \tag{7.3}$$

Equation 7.3 is plotted in Figure 7.4 where the wavenumber is measured in terms of the FWHM of the airglow layer. The individual graphs in the plot represent different phases of the wave from $\phi = 0$ to $\phi = \pi/2$ in steps of $\pi/20$ where the co-ordinate origin is placed in the centre of the airglow layer profile.

This means that even if the integration time of the Fabry-Perot spectrometer were infinitely short, it only records winds with a minimum vertical wavelength. Wind distributions in the layer with longer vertical wavelengths result in the Fabry-Perot spectrometer reporting an average wind which is smaller than the maximum wind actually in the layer.

Equation 7.3 describes the static case which handles stationary waves. However, waves are likely to travel during the integration time of the FPS hence change their phase with time. To account for this phase change the cosine term in Equ. 7.3 must depend on the time. Assuming that the phase speed c does not change much during the integration time a linear function $\phi(t) = ct + \phi_0$ can therefore be used:

$$\Psi(m, \phi(t)) = \sqrt{2} e^{-\frac{m^2 \sigma^2}{2}} \cos(m\phi(t)) \tag{7.4}$$

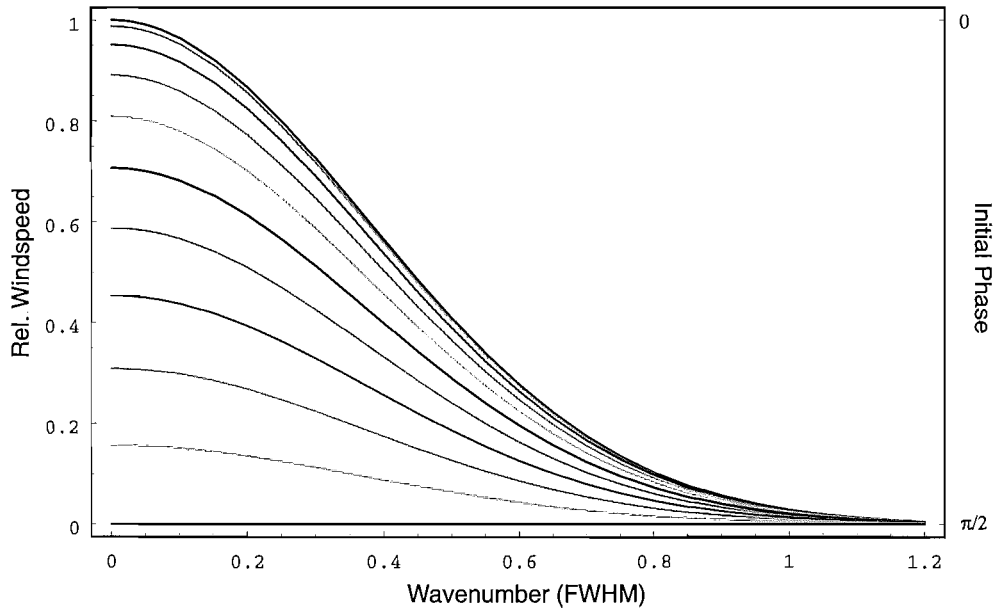

Figure 7.4: Shown here is the detected wind (normalised) depending on the wavenumber (measured in terms of FWHM of the airglow layer profile). The different curves show the dependence of the detected wind on the phase of the wave within the airglow layer (see text for detail).

Integrating this over the integration interval $t-t_0$ yields a function $\Phi(\omega, t, t_0, \phi_0)$ of the wave frequency ω, the integration start time t_0 and the integration stop time t, and the phase ϕ_0 at the start of the integration.

$$\Phi(\omega, t, t_0, \phi_0) = \int_{t_0}^{t} \Psi(\omega, \phi(t))dt = \tag{7.5}$$
$$\sqrt{2}e^{-\frac{m^2\sigma^2}{2}} \left[\frac{\sin(\omega t + \phi_0) - \sin(\omega t_0 + \phi_0)}{\omega}\right]$$

By setting the integration start time $t_0 = 0$, the stop time $t = 1$ and the exponential term in Equation 7.5 to one, we can examine the dependence of the detected relative wind speed on the frequency of the wave (i.e. airglow layer profile effects). $\Phi(\omega, \phi_0)$ depends now only on the frequency ω and the phase ϕ_0 of the wave at the start of the integration and the frequency

is expressed in terms of phase angle per integration time interval. As the direction of the detected wind is not of interest here the absolute value of $\Phi(\omega, \phi_0)$ can be used:

$$\Phi(\omega, \phi_0) = \left| \frac{\sin(\omega + \phi_0) - \sin(\phi_0)}{\omega} \right| \tag{7.6}$$

Equation 7.6 is plotted in Figure 7.5 for an initial phase $\phi_0 = 0$ and frequencies between 0 and 4π. This shows that for a given vertical wind distribution in the case of a stationary wave $\omega = 0$ the detected wave has, as expected, maximum amplitude. Waves that have a frequency $\omega > 0$ will be detected with a smaller amplitude. The FPS detects no wind in cases where the frequency $\omega = n\pi$ that is where the wave moves $n\pi, (n = 1, 2, 3...)$ during the integration time. However, after the first minimum at $\omega = \pi$ the next maximum reaches (in this case $\phi_0 = 0$) just a factor of 0.22 of the true maximum wind speed and all following maxima are even lower.

Given that $\omega = cm$ waves which either travel fast through the layer or have a small vertical wavelength, will be recorded with an attenuated amplitude. The degree of the amplitude attenuation depends on the integration time of the measurements.

Further complexity arises from the fact that the initial phase ϕ_0 can have an arbitrary value at the start of the measurement. A more complete picture can be drawn: Plotting Equation 7.6 $\Phi(\omega, \phi_0)$ in three-dimensions depending on frequency ω and initial phase ϕ_0, the detected amplitudes with different phase speeds and initial phases can be studied. Figure 7.6 displays this dependency with phase speeds c between 0 and 4π and initial phases ϕ_0 between 0 and π. It shows that waves traveling not much more than half a wavelength within the integration time and with an initial phase close to $n\pi$ will be detected with little attenuation. Waves which are faster or

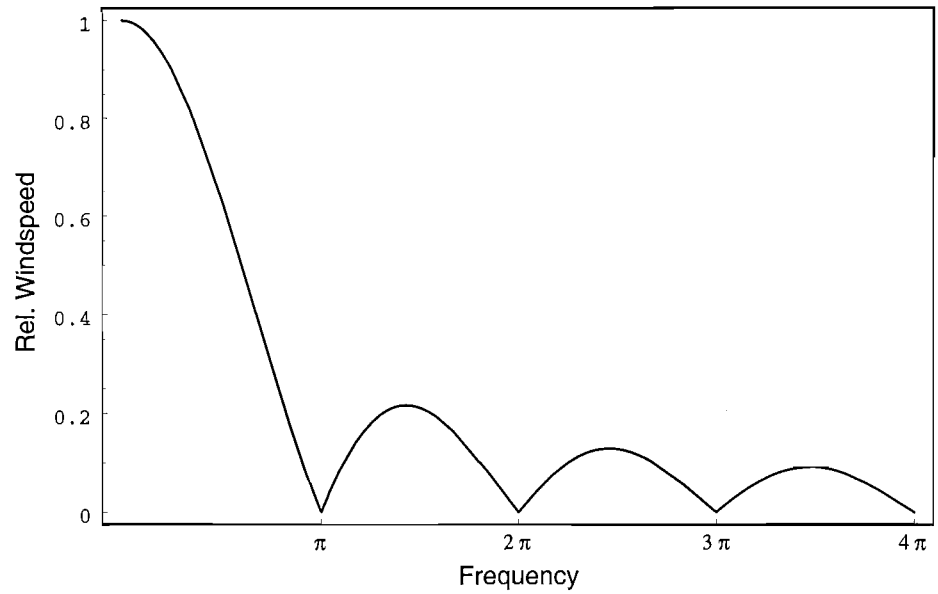

Figure 7.5: The wind (shown here normalised) as measured by the FPS depending on the frequency ω with the initial phase $\phi_0 = 0$ of the wave at the start of the measurement (see text for detail).

with an initial phase in the proximity of $n\pi/2$ will be detected with strong amplitude attenuation. The contour plot of Figure 7.7 shows the location of the the roots of Equation 7.6 more clearly. The contours are drawn in steps of 0.1 with the white area representing a detected amplitude of less than 10% compared to the maximum wind speed in the layer. As expected, the best detectability is a function of both the frequency and the initial phase. For example in stationary waves an initial phase of $\pi/2$ will result in no detection, while faster waves are significiantly attenuated at varying initial phases. The dependence on the vertical wavelength (as shown in Figure 7.4) shows that in the best case where the initial phase of the wave is close to $n\pi$, even waves with a wavelength of up to 2 times the FWHM of the airglow layer are detected with only 20% of the maximum wind by the Fabry-Perot spectrometer.

Equation 7.5 describes both the amplitude attenuation due to both the width

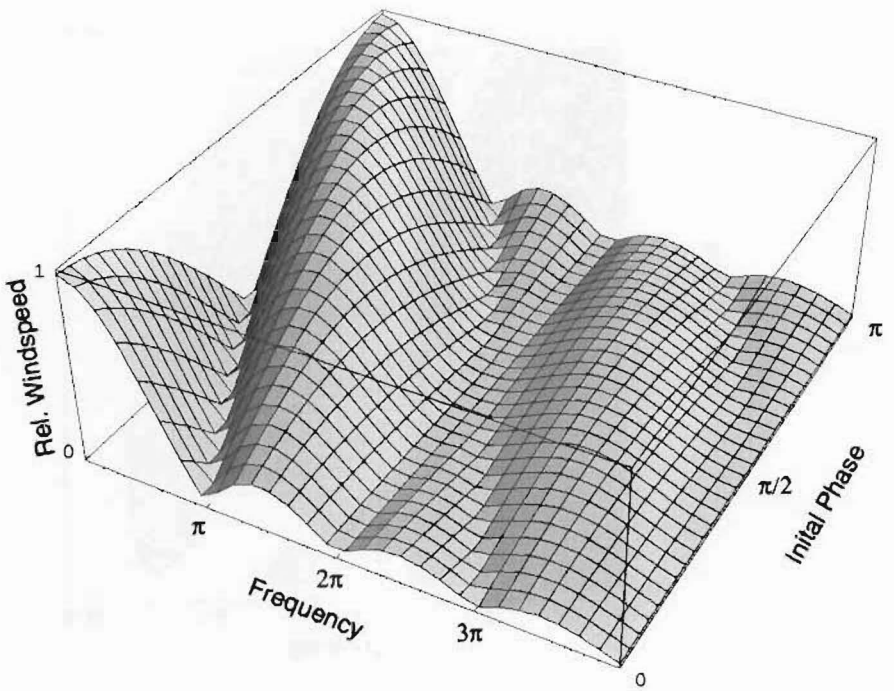

Figure 7.6: The wind (shown here normalised) as measured by the FPS depending on the frequency ω and the initial phase ϕ_0 of the wave at the start of the measurement (see text for detail).

of the layer and the frequency ω of the wave. Assuming the airglow layer width to be 10 km (see Chapter 2.3 for more detail) and the FPS integration time to be 10 minutes allows calculation of the detected relative wind speed (as shown in Figure 7.8) for vertical wavelength between 10 and 50 km and wave periods up to 1 hour. Panels (a),(b),(c), and (d) show the calculated contours with initial phases $\phi_0 = 0$, $\pi/4$, $\pi/2$, and $3\pi/4$, respectively. These graphs show the strong dependence of the filter function 7.5 on the initial phase of the wave.

Three parameters of wave motion in the atmosphere, the wavelength, the frequency, and the inital phase have been taken into account in describing the observational limit of the Fabry-Perot spectrometer. Taking now the solutions of the gravity wave dispersion relation (see Equation 2.19) and plotting

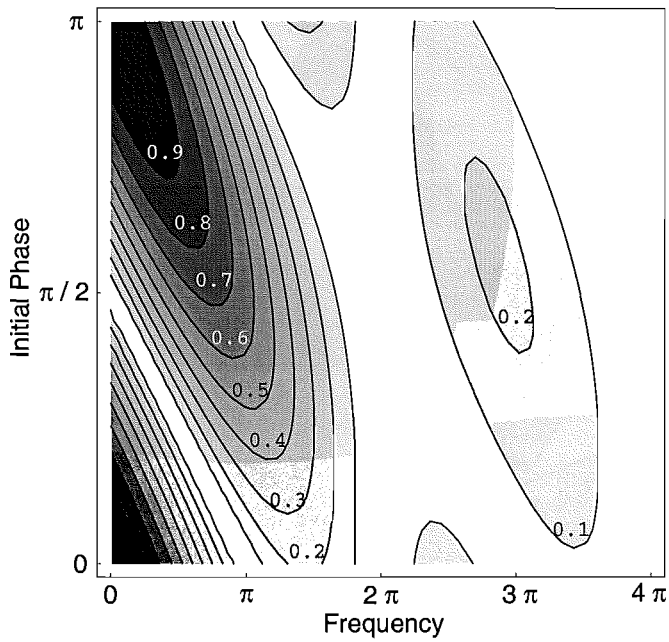

Figure 7.7: The wind (shown here normalised) as measured by the FPS as a function of frequency ω and initial phase ϕ_0 as in Figure 7.6 here as a contour plot, showing the pattern of the roots of Equation 7.6 (see text for detail).

a selection of those solutions on top of the contours of the Fabry-Perot spectrometer filter function will give insight into what waves will experience the most amplitude attenuation.

Figure 7.9 shows the filter function from Figure 7.8 with contours of horizontal gravity wavelengths between 20 and 200 km versus vertical wavelength and wave period. As stated in Chapter 2 about 80% of the gravity waves measured have a horizontal wavelength between 10 and 120 km and Meek et al. (1985) and Giers et al. (1997) showed that the mean horizontal phase speed is about 50 ± 20 ms^{-1}. This is consistent with measurements of the characteristic vertical wavelength λ_* which has been measured to be between 10 and 16 km (Gardner & Taylor 1998) However, most energy is in the waves with vertical wavelength between 0.3 and 3 times the characteristic wavelength λ_* as shown in Figure 7.10 (Vincent 1984, Manson et al. 1979, Senft

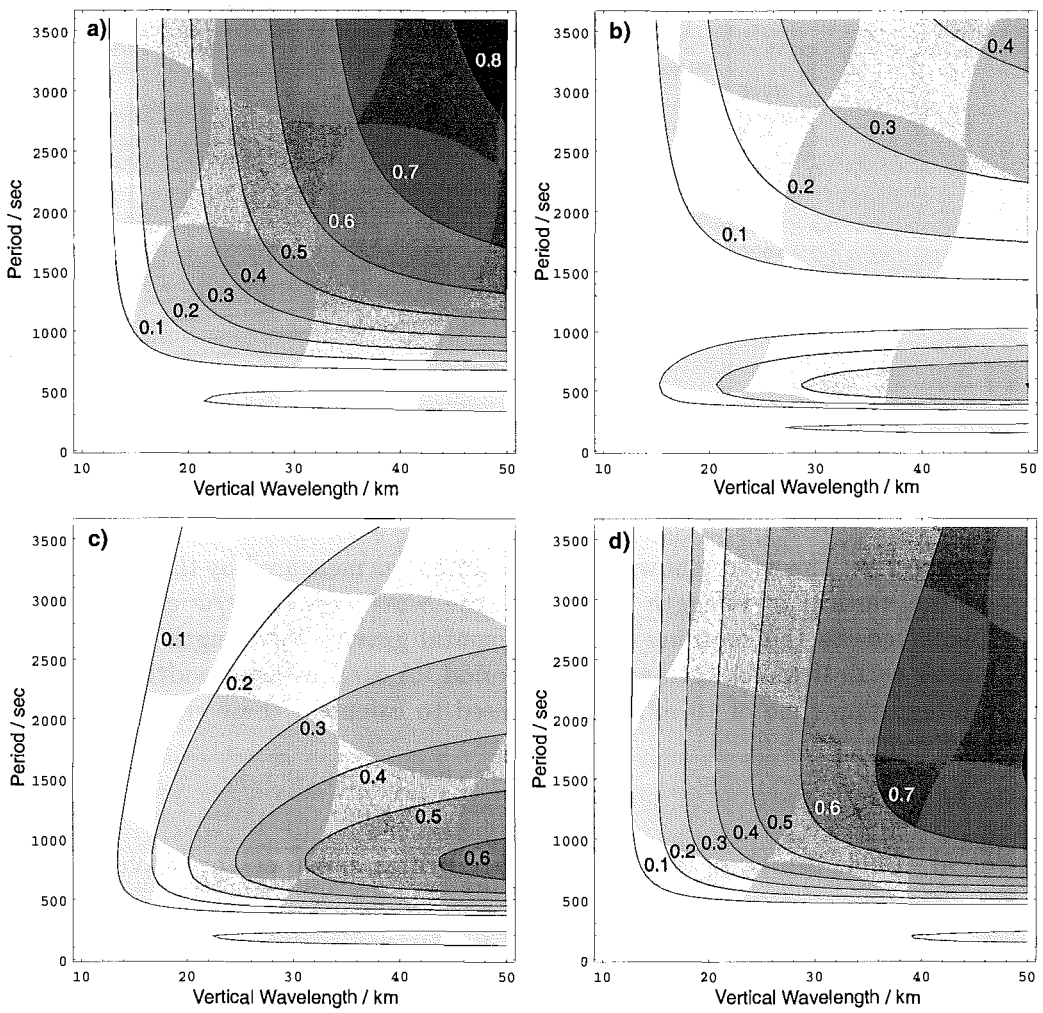

Figure 7.8: The wind (shown here normalised) as measured by the FPS depending on the vertical wavelength $2\pi/m$ and the wave period $2\pi/\omega$ for initial phases $\phi_0 = 0$ (Panel a), $\phi_0 = \pi/4$ (Panel b),$\phi_0 = \pi/2$ (Panel c), and $\phi_0 = 3\pi/4$ (Panel d), using Equation 7.5. A airglow layer width of 10 km and a integration time of 10 minutes was used to calculate these contours. (See text for detail)

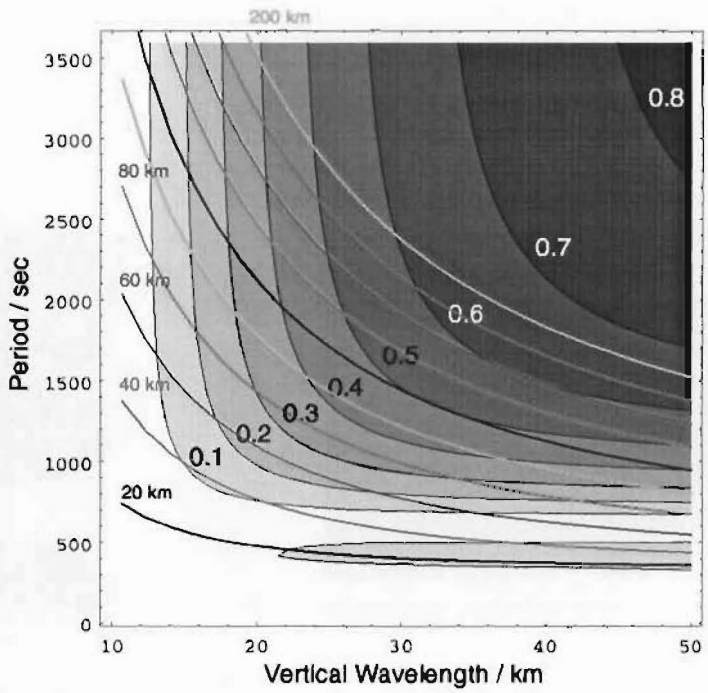

Figure 7.9: The wind (shown here normalised) as measured by the FPS depending on the vertical wavelength $2\pi/m$ and the wave period $2\pi/\omega$ as in Figure 7.8. Overlayed are the contours of the horizontal gravity wavelength (coloured lines) versus vertical wavelength and wave period. A airglow layer width of 10 km and a integration time of 10 minutes was used to calculate these contours. (See text for detail)

et al. 1993, Smith et al. 1987). This brings most of the wave activity in the detected wind speed region between 0 and 0.4 and the detected wave amplitudes therefore close to the measurement uncertainties.

It could be argued that the results cited here are based on empirical data recorded with instruments such as medium frequency radars and Lidars that have their own observational limits and might therefore present biased gravity wave activity. These observational limits have been described by Gardner & Taylor (1998) and show that these instruments are able to record the part of the wave spectrum which is of concern here.

The analytical model derived here describes the effect of the spatial and

temporal averageing for given wind distributions depending on the wavelength, the phase speed, and the initial phase. As a result the analytical model demonstrates that a good portion of the gravity wave spectrum is not detectable by the Fabry-Perot spectrometer.

7.4 Synthetic Spectrum

The analytical model of the Fabry-Perot spectrometer sampling properties developed in 7.3 will now be applied to assumed real winds. A numerical model will be presented which simulates the sampling of the Fabry-Perot spectrometer as described by the analytical model and which simulates the 'true' winds based on observations made by others.

Numerical modelling of the sampling process of the instrument and of the gravity wave activity in the atmosphere enables the effect of the observational limit on the detectability of a certain gravity wave activity to be studied. The instrument model can simulate sampling behaviour such as the slow sampling and long integrating FPS or the fast instantaneous sampling meteor radar. Comparing simulations and measurement of both the FPS and the meteor radar will reveal whether the difference in variances found (see Figure 7.1) can be explained by the difference in the sampling process of each instrument. The filter function describing the observational limit of the FPS can be switched on or off and the effect on the wind measurement can be studied. It will be shown that without the limitations the results obtained will be similar to those obtained by the meteor radar as shown in Figure 7.1. The observational limits of the meteor radar are, however, not included here but will be described by Marsh (1999).

7.4.1 Instrument Model

This part of the model will describe the sampling effect of the Fabry-Perot spectrometer on the real winds. The model of the FPS sampling is easily written in a few lines of code. The instrument samples in 5 different directions. Only one direction is of interest here. The sampling is therefore equidistant and the time span between the end of one measurement to the beginning of the next measurement is four times the integration time. The gravity wave model function (see section 7.4.2) is not easily analytically integratable so it is therefore approximated by averaging over 100 sample points during the integration time interval. This appears to be adequate, taking into account that only very little high frequency gravity wave activity, with periods much smaller than the integration interval, will be present as the integration time is already close to the Brunt-Vaisala period which in the mesopause is about 4.9 minutes.

7.4.2 Gravity Wave Model

This part of the numerical model is simulating the gravity wave activity in the mesopause, lower thermosphere region. The resulting wave functions will be sampled by the instrument model (described above) to simulate the Fabry-Perot spectrometer sampling with and without the above described observational limitations

Desirable features of the model

A numerical model should be as simple as possible to minimize computation time but also of sufficient complexity to correctly simulate the behaviour in

question to an accuracy adequate for the problem under investigation. It is therefore opportune to restrict the model to those quantities which would directly influence the result.

For the problem here the model can be restricted to buoyancy waves. The acoustic branch of the gravity wave dispersion relation is not of interest here as the periods of those waves are smaller than the integration time of the Fabry-Perot spectrometer (420-600 sec) and therefore well beyond the detectability of the spectrometer.

The gravity wave dispersion relation describes possible solutions of wave motion in the atmosphere but it does not indicate which waves are most likely to be observed. The questions are: What does the spectrum of Gravity waves in the middle upper atmosphere look like? What is the characteristic wavelength? What is the mean amplitude of the waves observed? This means that apart from the prediction of gravity models described by others (ie. (Dewan & Good 1986, Smith et al. 1987, Hines 1991, Gardner 1994, Gardner 1998)) empirical data have to be fed into this model.

The model builds a simulated spectrum of gravity waves which will be sampled by a model of the Fabry-Perot sampling properties. To build the spectrum the algorithm sets the phase speed and the horizontal wavelength at random using empirical distributions of these parameters. The gravity wave dispersion relation delivers with these two parameters the corresponding vertical wavelength. The amplitudes of the waves are determined using a Gaussian distribution of empirical wind speeds and employing a model saturated gravity wave spectrum with a characteristic wavenumber m_* of 14 km. The amplitude is then multiplied by the factor derived from the FPS lowpass filter function (Equation 7.5). The model superimposed 50 of those waves to build a spectrum.

The model includes recent advances in theoretical modelling of the spectral composition of gravity waves in the mesopause, lower thermosphere region such as the saturation effect in the gravity wave spectrum. These spectra are characterised by a vertical wavenumber m_* that partitions the spectrum into a low wavenumber regime dominated by the gravity wave source characteristics, and a high wavenumber region dominated by saturation and dissipation processes. The spectrum is assumed to be propotional to m^a with $a \approx 3/2$ in the source region ($m < m_*$). In the saturation region ($m > m_*$) the spectrum is proportional to N^2/m^3, where N is the buoyancy frequency.

It also reflects the empirical knowledge of the gravity wave spectral distribution measured by many other authors. Incorporating these features into the model enables simulations of the gravity wave activity in the mesopause, lower thermosphere region to an accuracy which is sufficient to prove that the low variability in the data obtained with the FPS are caused by a filter which determines the observational limits of the FPS and that without this filtering the variability of the measured data would resemble that obtained by a meteor radar.

Observational parameters

Measurements of gravity waves in the mesopause, lower thermosphere region have been described by others (e.g. (Manson et al. 1979, Vincent 1984, Meek et al. 1985, Richter et al. 1981, Senft et al. 1993) using a variety of techniques such as radars, lidars, airglow imagers etc. These authors have reported mainly on the mean vertical wavelength and the mean amplitude, although some have reported on the wave spectrum of the wave activity found in the middle upper atmosphere. Manson et al. (1979) found a mean vertical wavelength $\lambda_z \sim 20$ km using a medium frequency radar in Saskatoon

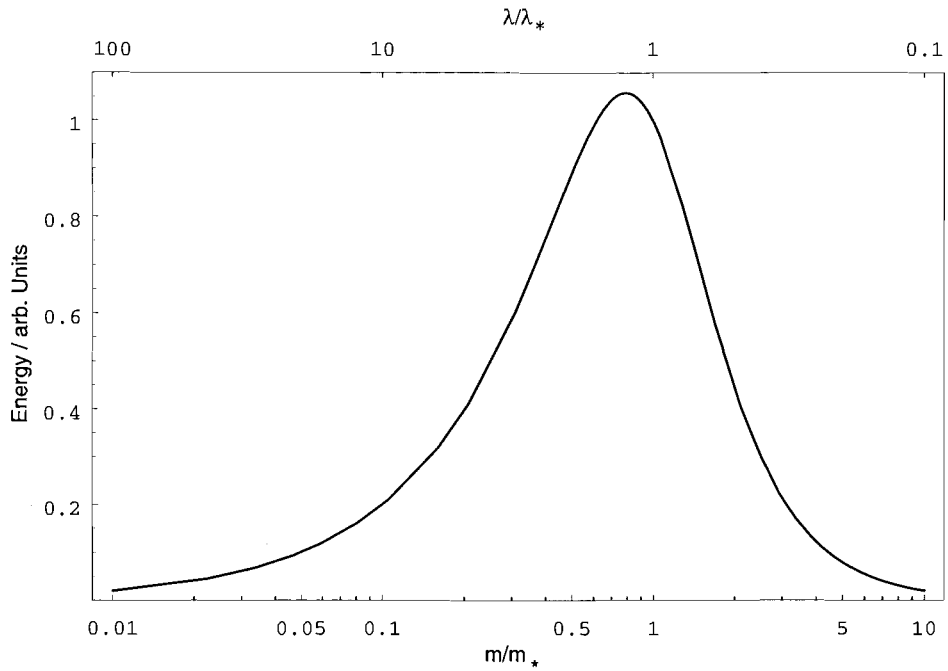

Figure 7.10: The vertical wavenumber spectrum on an energy-content graph. Equal areas make equal contributions to the energy. After Smith et al. [SmiEA87].

(Canada). Vincent (1984) measured a mean vertical wavelength λ_z of 12 km with a mean amplitude u'_{rms} of 30 ms^{-1}. He found that a large fraction of the energy flux is carried by short period (<1h) waves using a medium frequency radar in Adelaide, Australia. Vertical wavelengths λ_z between 3 and 15 km and phase speeds c of 0.5-3 ms^{-1} were reported by Richter et al. (1981) using a lidar in Urbana, Illinois. Using a lidar (during the AIDA-89 campaign) Senft et al. (1993) measured a mean vertical wavelength λ_z of 6.2 km and an amplitude u'_{rms} of 28 ms^{-1}. The mean characteristic wavelength $\bar{\lambda}^*_z$, which defines the breakpoint in the spectrum between the weak and strong wave interaction subranges, was for example measured to be 14.3 km which lies well within the interval of 10 to 16 km assumed in the gravity wave model by Gardner & Taylor (1998). According to a model after Smith et al. (1987) most gravity wave energy lies within a factor of 3 around 1.26 λ^*_z (see Figure 7.10). This corresponds well with the findings of Vincent

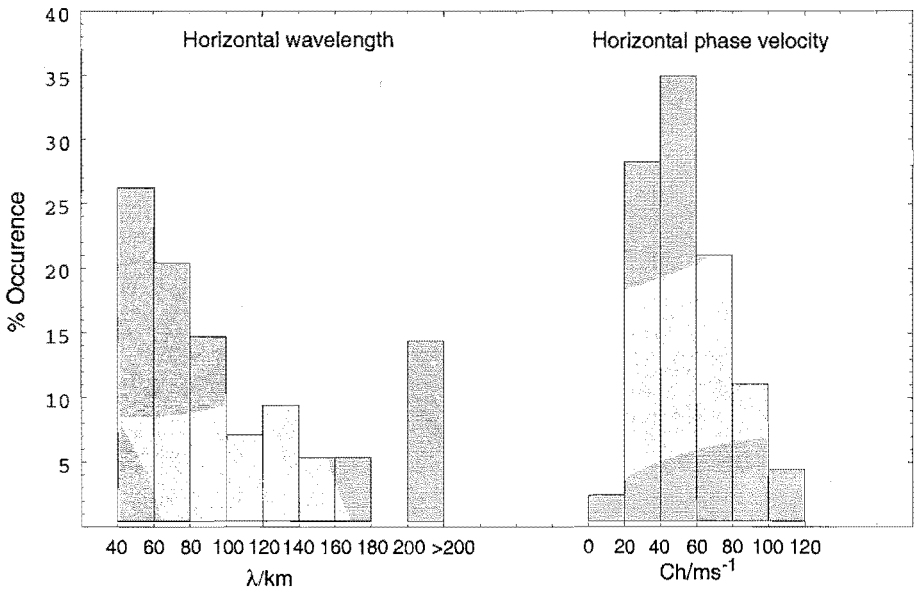

Figure 7.11: The relative occurrence of the horizontal wavelengths (left) and of the observed horizontal phase speed (right). After Meek et al. (1985).

(1984) who observed that the most energy was transported in waves with wavelength λ_z to 10-20 km. Meek et al. (1985) measured the horizontal scale of gravity waves and their phase speeds above Saskatchewan, Canada, and found the distributions shown in Figure 7.11. Similar results were reported by Giers et al. (1997). They found that waves with a horizontal wavelength of less than 120 km make up about 80% of the measured wave activity and that the observed horizontal phase speeds are centered at about 50 ms^{-1}. This is confirmed by Vincent (1984) who calculated the horizontal phase speed to be around 40 ms^{-1}.

In summary, the mean empirical vertical wavelength lies between 10 and 20 km, the mean amplitude measured is about 30 ms^{-1}. For the horizontal wave parameters most measured wavelengths lay between 0 and 120 km. The observed phase speeds lay around 50 ms^{-1}.

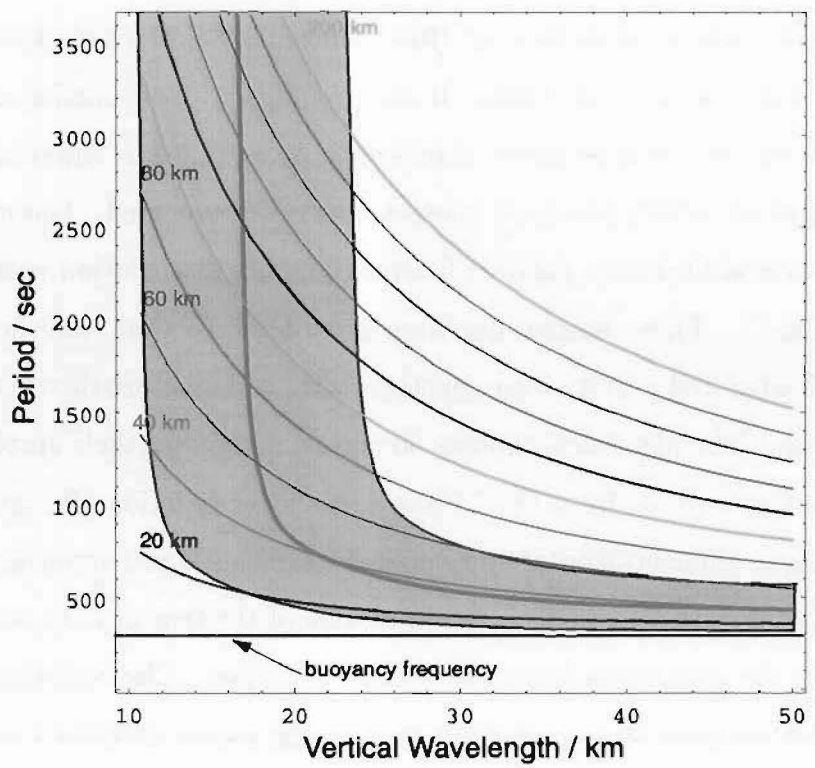

Figure 7.12: The period of gravity wave depending on the vertical and the horizontal wavelength. The shaded area shows the region around the horizontal phase speed of 50 ms^{-1} (red thick line) where 68% of the wave activity in the model is taken from.

Parameters of the synthetic spectrum

The information given above about gravity wave wavelength and phase speed is used to develop a simple gravity wave model. The algorithm sets a horizontal phase speed at random, using a Gaussian distribution, with a mean of 50 ms^{-1} and a variance of 20 ms^{-1}. Using the horizontal wavelength distribution after Meek et al. (1985) (see Figure 7.11) the model takes at random a horizontal wavelength and calculates the corresponding vertical wavelength using the gravity wave dispersion relation. Most vertical wavelengths λ_z will therefore be in the range between 10 and 30 km (see Figure 7.12). This range appears to be reasonable as it includes mean horizontal wavelengths re-

ported by others (Manson et al. 1979, Vincent 1984, Meek et al. 1985, Richter et al. 1981, Senft et al. 1993). It also includes a good portion of the interval around the characteristic wavelength $\bar{\lambda}_z^* = 14.3$ km where according to Smith et al. (1987) the most energetic waves are located. The amplitude of the waves are taken at random from a Gaussian distribution with a variance of 25 ms^{-1}. These amplitudes were attenuated so that they lay close to a model saturated gravity wave spectrum with a characteristic wavenumber m_* of 14 km. The algorithm chooses 50 waves, multiplies their amplitudes with the factors derived from the FPS lowpass filter function (Equation 7.5) according to their horizontal and vertical wavelength and superimposes them. This is taken to be an adequate simulation of the true gravity wave distribution in the mesopause,lower thermosphere region. The resulting winds will then be sampled by the instrument sampling model described earlier.

7.4.3 Measuring winds from the synthetic spectrum

A number of simulations have been performed in the way described above. Figure 7.13 shows an example where the resulting unfiltered data is shown in red and the filtered data is plotted in blue. The Figure resembles Figure 7.1 which showed the variances of the meteor radar data and the Fabry-Perot spectrometer.

Comparing the variance of the unfiltered model data with that of the meteor radar data reveals a striking similarity between the variability of the measured and modelled winds. The top panel of Figure 7.14 shows both (in red) the variability of the model data and (in blue) the variability of some typical meteor radar data. The variability of the filtered model data and the variability of some typical Fabry-Perot spectometer data is presented in the bottom panel of Figure 7.14. The filtered model data simulates the variabil-

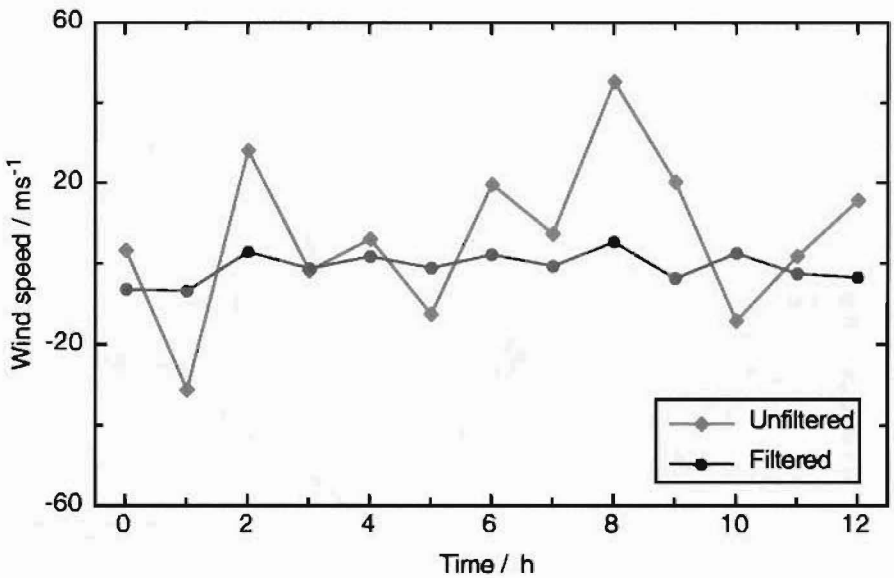

Figure 7.13: The result of the 'unfiltered' model run (red) shows the variablity of the winds without the influence of the FPS lowpass filter function while the 'filtered' model run displays the winds obtained when the sampling goes through the FPS lowpass filter function. (see text for detail).

ity of the FPS data very well and both data sets have a similar numerical variance.

The model is able to produce data similar to that obtained by the FPS measurements using the FPS filter function (section 7.3). Without the filter the smoothing influence of the airglow layer width and the integration time on the data is not present and the results are comparable to the data obtained with the meteor radar. The good agreement between the model data and the data abtained by measurements using the meteor radar and the Fabry-Perot spectrometer suggests that the FPS measurements are indeed limited in their resolution of wave activities as described in 7.3.

It could be argued that the model was in part based on empirical data recorded with instruments such as medium frequency radars and Lidars that have their own observational limits and might therefore present biased grav-

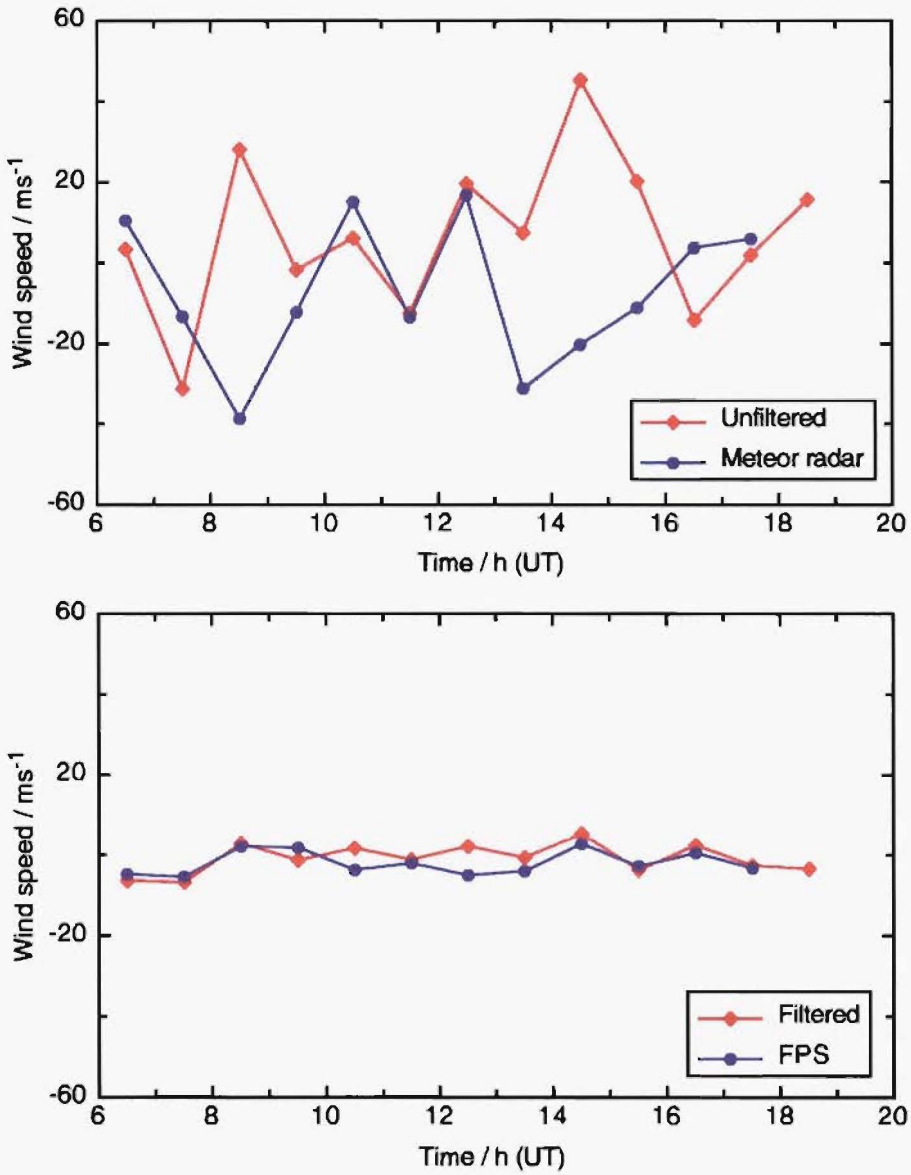

Figure 7.14: Comparison of the variability of typical wind data obtain from meteor radar (top) and FPS (bottom) with simulated data. The top panel shows the non filtered model result (red) and the variability of meteor radar data (blue). The bottom panel displays the variability of the FPS data (blue) and the result of a filtered model run.

ity wave activity. These observational limits have been described by Gardner & Taylor (1998) and show that these instruments are able to record the part of the wave spectrum which is of concern here.

In summary, the Fabry-Perot spectrometer is unable to detect waves in that part of the gravity wave spectrum which transports the most energy into the mesopause, lower thermosphere region. These waves are, however, detected by other instruments such as meteor radar, medium frequency radars, and Lidars. These instrumental differences have to be taken into account when for example the results of measurements are to be compared among different kind of instruments. The Fabry-Perot appears to be the wind measuring instrument of choice if long vertical waves are to be measured such as tides.

7.5 The Effects of Wind Shear on FPS Temperature Determination

The FPS measures the emission of atomic or molecular transitions. With the high resolution obtained by the instrument, the width of the Doppler broadened emission profile can be measured. This width is directly related to the temperature of the emitting species (see (Demtröder 1991)). Equation 7.7 shows the simple relation between the width $\delta\nu$ of the profile, the temperature T and the molar mass M. With the etalon employed here, an accuracy of 2 Kelvin is achievable assuming a good signal to noise ratio in the recorded spectrum.

$$\delta\nu = 7.16 * 10^{-7}\nu\sqrt{\frac{T}{M}} \tag{7.7}$$

This simple concept of temperature measurement is complicated by the fact that the position of the fringes in the spectrum is dependent on the wind in the airglow layer via the Doppler shift. As discussed previously, the observed spectrometer line consists of the spatial and temporal average of all emissions occuring within the airglow layer. In the case of a homogeneous wind the emission profiles from different parts of the layer will occupy coincident positions in the spectrum and therefore the width of the observed line is identical to the line width from each part of the airglow layer. In that case, the temperature will be directly related to the observed line width. However, for a non homogeneous wind distribution the emission profiles from different parts of the layer will be found at different positions in the recorded spectrum. As the instrument sums the emission over the whole layer the resulting emission profile will be broader compared with the profile obtain for a homogeneous wind distribution. This broader profile will result in an apparent

temperature increase if this broadening effect is not be taken into account. The following sections will therefore discuss the extent to which the wind distribution in the layer effects the observed line width, and the associated error in the derived temperature. Initially the effect of wind distribution of a monochromatic vertical wave is described. Thereafter the effect of a more realistic random wind distribution on the temperature is presented.

7.5.1 Monochromatic Waves

The effect of a monochromatic vertical wave in the layer on the temperature is studied by sampling a sinusoidal wind distribution. The airglow layer is divided into 100 equally sized sublayers. Each sublayer represents a Gaussian emission profile where amplitude and position are assumed to depend only upon the airglow emission intensity and the wind speed for that part of the airglow layer. The temperature is assumed to be homogeneous throughout the layer. The width of these emission profiles observed at the ground by a model Fabry-Perot spectrometer were than compared to the result with a constant wind in the layer. The results are shown in Figure 7.15 for the atomic oxygen for wave amplitudes up to 50 ms^{-1}. A fit to the obtained data points reveals a qudratic function $T(w) = aw^2$ to describe the dependence of the temperature difference T as a function of the wave amplitude w. The coefficient $a = 9.22 * 10^{-4} \pm 0.0001$ in case of the atomic oxygen emission. The temperature difference for other airglow layers such as the hydroxyl layer can be calculated by multiplying the temperature difference found for the atomic oxygen line with the ratio of the atomic weights of for example hydroxyl and the atomic oxygen $M_{OH}/M_{OI} * T_{OI} = T_{OH}$. Interestingly, the temperature difference was found to be independent of the wavelength.

This means that the temperature measured by the Fabry-Perot spectrome-

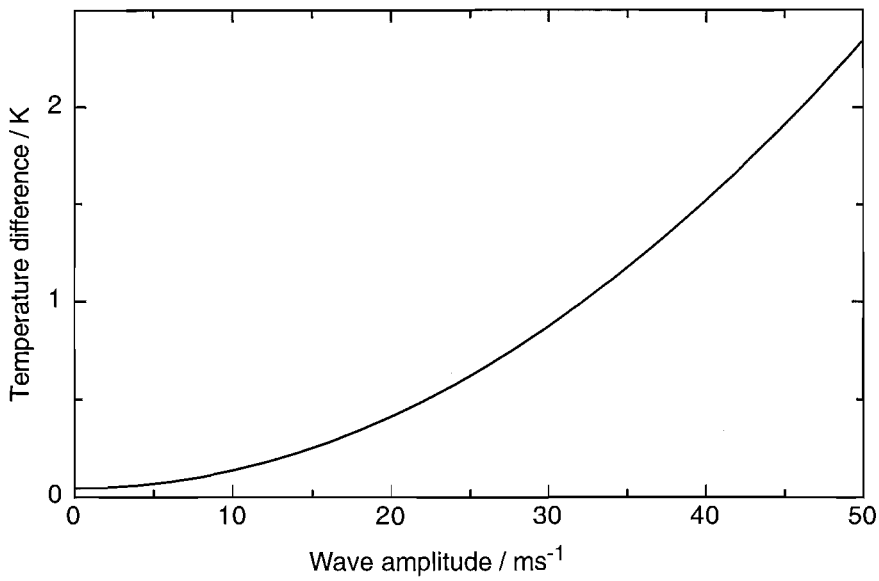

Figure 7.15: The temperature dependence on wind speed in the atomic oxygen comparing the temperature findings between a homogeneous wind profile in the airglow layer and a wind profile like a vertical monochromatic wave with wavelength λ $\leq$FWHM of the airglow height profile (see text for detail).

ter is effected by wind shear in the airglow layer. The resulting temperature increase originating from monochromatic vertical waves with mean wave amplitudes of around 30 ms^{-1} (see eg. Vincent (1984)) are very small and well within the typical uncertainties (4-5 K) of the temperature determination.

7.5.2 Modelled Wind Distribution

Pure monochromatic wind waves will be the exception rather than the rule in the atmosphere. In general the wind profile will more or less resemble noise as waves with different wavelength interfere constructively or destructively with each other. Furthermore, waves also may break leaving turbulent air behind. It was shown before that the gravity wave model described in Section 7.4 is able to model the wind distribution equal to that obtained by a meteor radar. It therefore appears to be appropriate to use that model to caculate

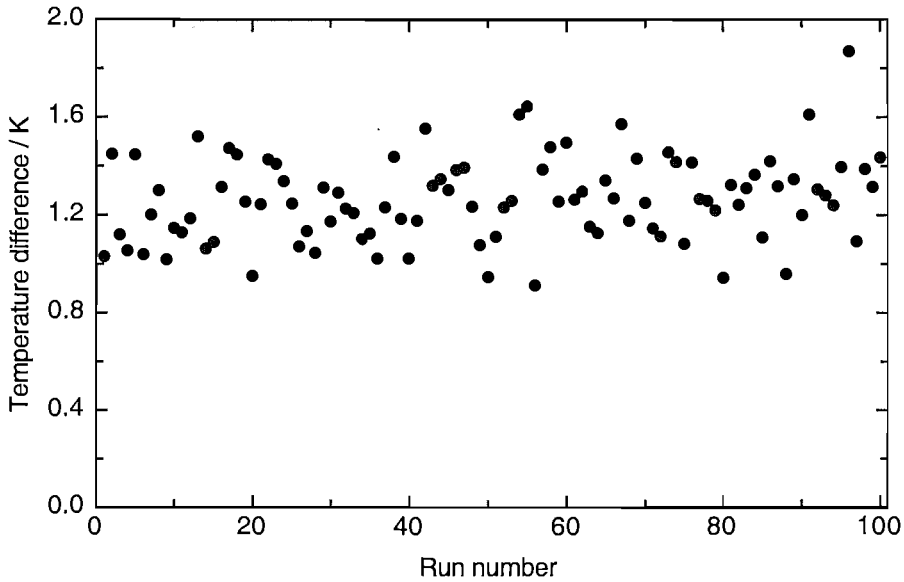

Figure 7.16: The temperature dependence on wind speed in the atomic oxygen airglow layer demonstrated by comparing the temperature findings between a homogeneous wind distribution in the airglow layer and a modelled wind distribution obtained from the model described in Sectio 7.4 (see text for detail).

the wind distribution in the airglow layer.

The airglow layer is, as described for the monochromatic wind profile, divided in to 100 equally sized sublayers. The modelled spectrum obtained from the gravity wave model (Section 7.4) is sampled in each sublayer. Each wind speed determined the position of the emission profile in the spectrum while the amplitude was set according to the airglow emission intensity profile which here was set to a FWHM of 10 km. Determining the width of the sum of those 100 Gaussian profiles yield a temperature which was then compared with the temperature found for a profile describing a constant wind in the layer. The temperature differences are plotted in Figure 7.16 for the atomic oxygen emission. The temperature differences for the hydroxyl emission can be obtained by using the atomic weight ratios $M_{OH}/M_{OI} * T_{OI} = T_{OH}$ as described before in Subsection 7.5.1. Figure 7.16 displays 100 temperature

calculations.

7.5.3 Results

The Figures reveal that the temperatures calculated from the emission profiles of the FPS are over estimated by only 1.26 $\pm$ 0.2 K for the atomic oxygen emission and 1.34 $\pm$ 0.2 K for the hydroxyl emission. These are systematic errors resulting from the ubiquitous presence of gravity waves in the atmosphere. These errors are well within the usual random uncertainties. However, as these are systematic errors and using the fact that the temperatures found are always overestimated the temperatures can be corrected by subtracting about 1.3 K for the atomic oxygen and the hydroxyl emission.

7.6 Detectability of long horizontal Gravity Wave Events

The mathematical description of the observational limits of the FPS regarding gravity waves and the simulation of the sampling using this model show that the attenuation of wave amplitudes is strongest where the most gravity wave activity is expected. However, long period waves with long vertical wavelength must also be present in the atmosphere even if only occasionally. Those waves with long vertical wavelength must be associated with a long horizontal wavelength and therefore have periods in the range of 0.5 to about 8 hours. This, based on the previous discussion, should make them well detectable by the Fabry-Perot spectrometer.

The FPS measures the wind in a volume North and South as well as East and West from the home site. Long wave activity with considerable amplitude

might therefore show up in the substantially different wind values obtained from opposing sampling volumes (e.g. North and South). However, the measured wave amplitude can be underestimated if the wavelength is much longer than the distance of the two sampling volumes (about 580 km for the atomic oxygen airglow layer). The wind differences between the two sampling volumes depends therefore on the distance between the sampling volumes and the wavelength of the gravity wave.

Signatures of such wave events can be seen in the FPS data during some nights. As an example of long wave events Figure 7.17 and 7.18 show the meridional (top) and zonal (bottom) wind data of the atomic oxygen emission for the 2nd and 12th May 1997, respectively.

Figure 7.17 (top panel) shows that at the beginning of the night both sampling volumes detect almost the same wind speed. The detected wind follows a distinct semidiurnal variation. At about 14:30 hours UT the wind findings in the southern sample volume start to deviate from the semidiurnal tide pattern. About two hours later, at 16:30 hours UT, the so far positive difference between North-South becomes negative as the instrument now detects a higher wind speed in the southern volume. The findings are similar for the zonal component shown in Figure 7.17 (bottom panel) and it can be seen that both sampling volumes show an almost perfect semidirunal wind variation throughout the night. The phase differences of about 30 minutes between the eastern and the western sampling volume arises from the distance of about 540 km between these volumes and from the fact that the tide migrates westward. Here, as in the meridional data, a deviation from the semidiurnal variation is observable in the second half of the night, in this case shortly before 16:00 hours UT. In the meridional data only the southern data shows a wave like deviation. In the zonal data only the data from the western sampling volume deviates from the semidiurnal tide pattern.

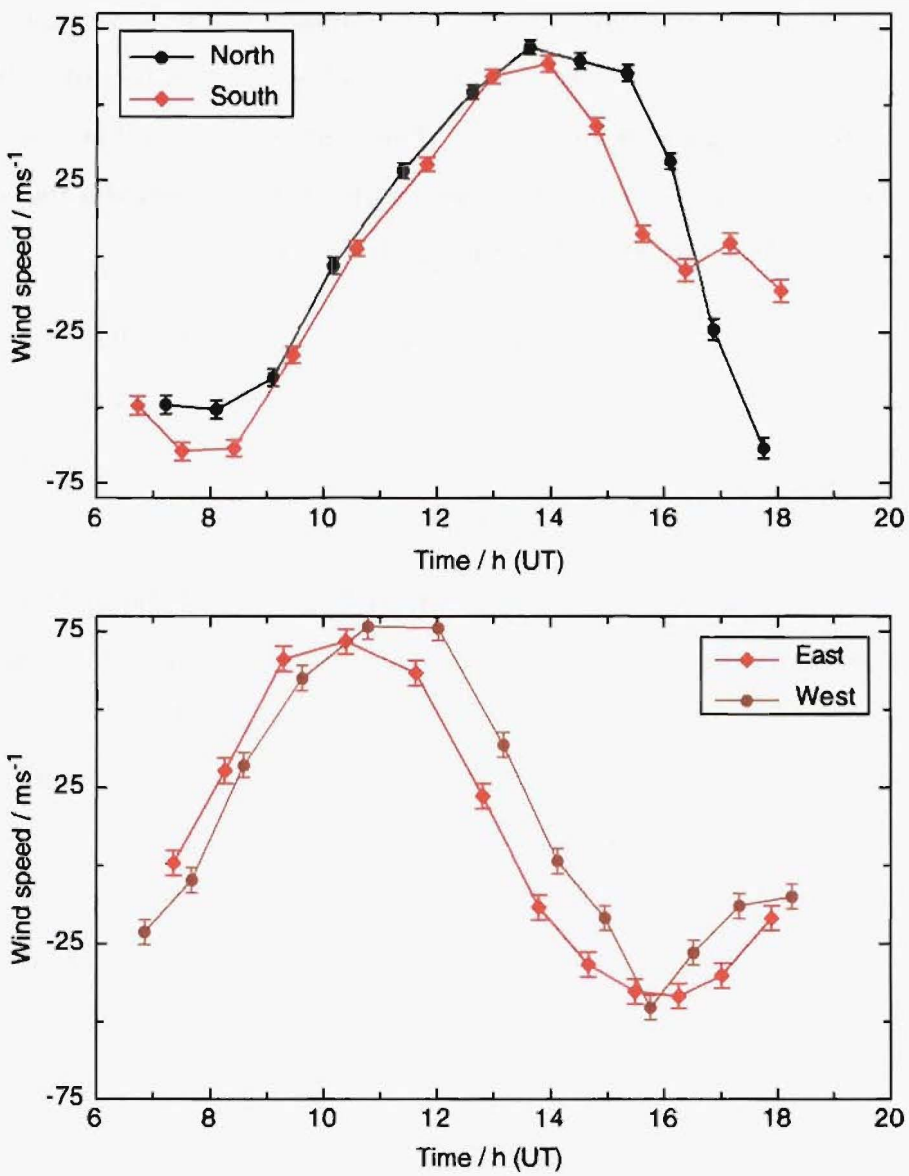

Figure 7.17: The meridional wind data from the atomic oxygen emission for 2 May 1997. During the first half of the night there is no wave activity others than the semidiurnal wave visible. In the second half a long gravity wave event drives the wind findings in the Northern and Southern sampling volumes apart (see text for detail).

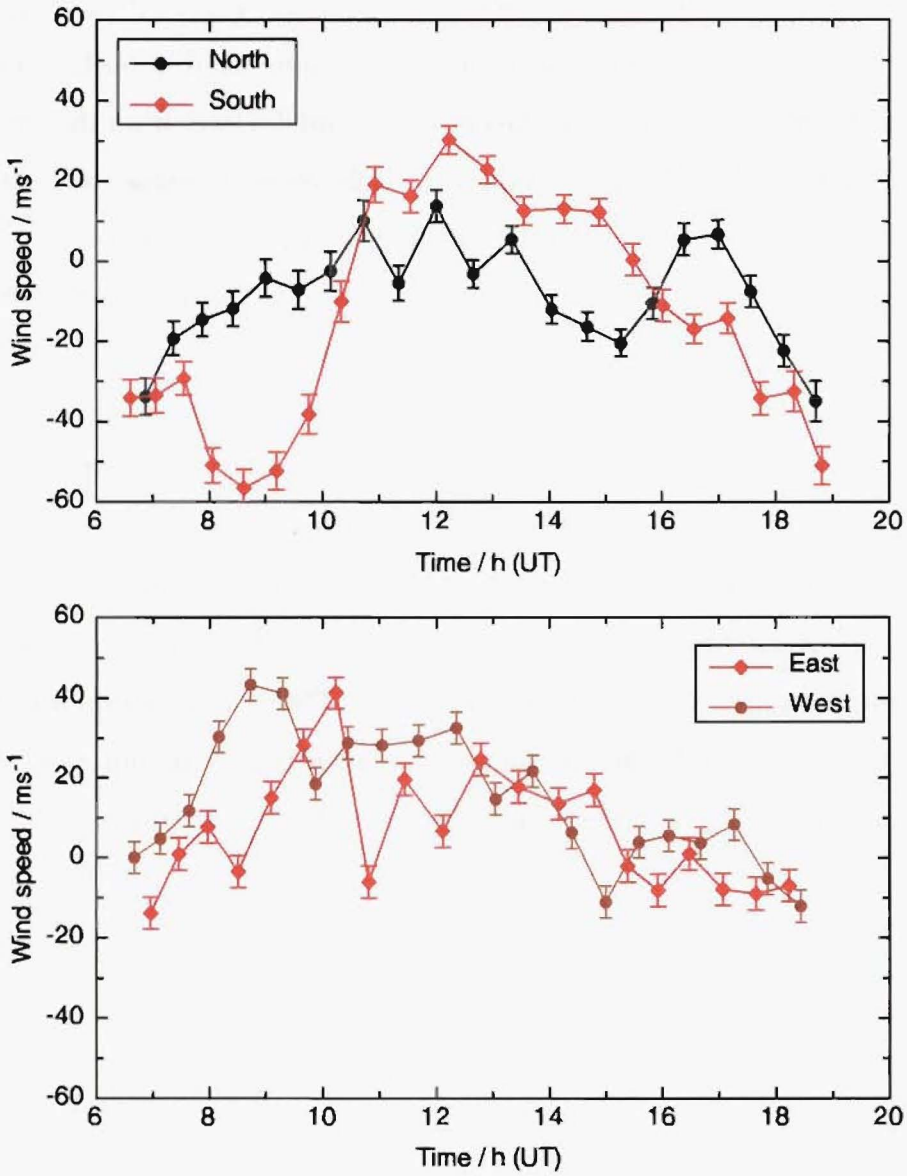

Figure 7.18: The meridional wind data from the atomic oxygen emission for 12 May 1997. During the whole night the wind findings in the Northern and Southern sampling volumes differ considerably with differences up to 45 ms^{-1} indicating strong gravity wave activity (see text for detail).

The second example data from the 12 May 1997 is displayed in Figure 7.18 where remarkable differences in the wind speed between the opposite sampling volumes during the whole night can be observed. At the beginning of the night the instrument detects almost the same wind in both volumes. After only three measurements the detected wind deviates from the semidiurnal tide pattern. For the next 2 hours the differences increase and reach about 45 ms^{-1}. Thereafter, at about 11:00 hours UT, the differences decrease and change from a positive to a negative difference between the northern and the southern sample volumes. Another sign-change takes place at about 16:00 hours UT. Differences of up to 45 ms^{-1} are detected in both cases. The zonal data do not show wave signatures as clearly but indicate a strong wave activity throughout the night. The fact that the differences change sign after a few hours suggests that these movements are caused by wave motions as the wave crest starting at one sampling volume has, after some time, reached the opposite sampling volume and *vice versa*. The gravity waves are distorted by the background wind in the airglow layer, that is in this case the mean wind plus the wind of the semidirunal tide at a given time.

For example, a wave which drives the wind in the meridional direction with an amplitude of 40 ms^{-1} will produce a maximum northward airflow of 40 ms^{-1} at a certain height, say A, at a height B with a wave phase distance of π between A and B it will produce a maximum southward airflow of 40 ms^{-1}. In case there is any background wind this wind superimposes with that originating from the wave. A southward blowing background wind of, for example, 10 ms^{-1} will decrease the amplitude of the northward airflow produced by the wave by 10 ms^{-1} and increase the amplitude of the southward airflow produced by the wave by the same amount. The wind difference, however, will be independent of the background wind speed assuming a homogeneous background wind over the ground distance of the sampling volumes.

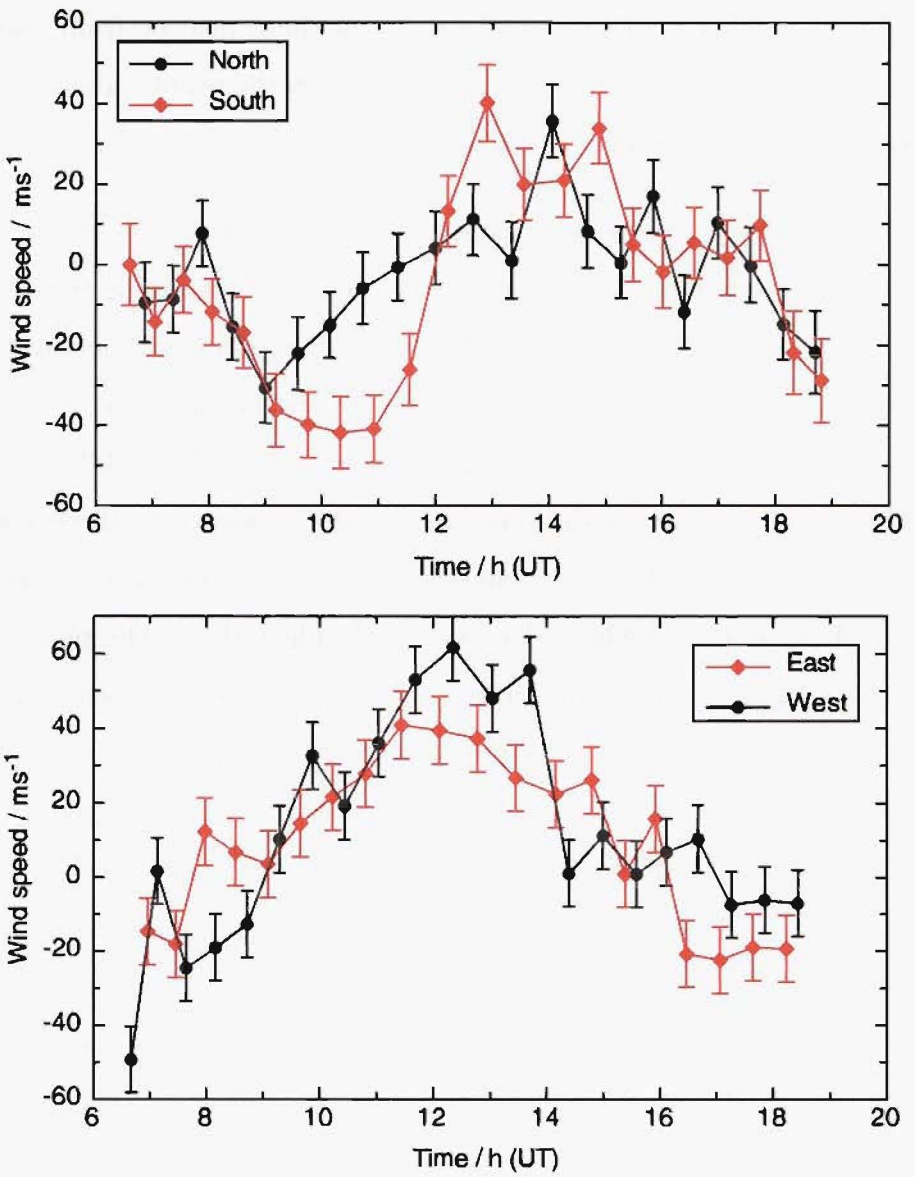

Figure 7.19: Meridional wind data from the hydroxyl emission height of 90 km on 12 May 1997. The top Panel shows the meridonal, the bottom panel the zonal component. During the whole night the wind findings in the Northern and Southern sampling volumes differ considerably (see text for detail). Compare with Figure 7.18 which shows the wind data at 103 km height.

The OH data for 12 May 1997 show similar features (see Figure 7.19). The maximum southward wind of the most prominent wave feature is reached at about 10:30 am UT where the OI data show the transition from a southward to a northward wind. The wind phase between the atomic and the hydroxyl airglow layer is therefore out by about $\pi/2$.

However impressive these differences are, considering that there are only two sampling points, it is not possible to exactly determine the wavelength of these waves. However, provided the phase difference between the two volumes is known the wavelength can be estimated since the distance of the two sampling volumes is a known constant. This phase difference can be estimated by comparing the wave amplitudes measured in the two sampling volumes as the amplitude depends on the phase of the wave. Considering a wave $A = \sin(x + \phi)$ where A is the amplitude and ϕ is the phase at which the wave has maximum amplitude. At a phase $\phi + \pi$ the waves amplitude will be at the minimum. That means that if in one sampling volume the maximum wind is measured and at the same time the wind in other volume is minimal (ie. maximum in the opposite direction) the phase difference is π and the wave has a wavelength of two times the sample volume distance. In the general case the recorded wind will indicate a phase difference other than π but the same considerations as above still hold. With a known maximum amplitude in one volume the wave equation $A = \sin(x+\phi)$ has to be solved for ϕ using the known amplitude A in the other sampling volume. This assumes that the wave is coherent over the distance of the sampling volume. As a wave is a periodic function the solutions for a given ϕ is not definite. The number of possible solutions can usually be restricted by incorporating other knowledge about the wave and considering what is a physically meaningful solution.

Taking the deviation of the wind between the semidiurnal tide and the North

and South sampling volume shown in Figure 7.18 during the first part of the night and using the wave amplitude attenuation of the FPS instrument, which restricts the possible wave solution to those measurable by the FPS, and the gravity wave dispersion relation results in an estimated horizontal wavelength between 1700 km and 2500 km. The airglow heights for this night were calculated to be 103 $\pm$1 km for the atomic oxygen layer and 90 $\pm$2 km for the hydroxyl layer using the wind comparison method between the Fabry-Perot spectrometer wind and the metoer radar wind (see 6). With the knowledge of the distance and the phase difference of the wind between the two airglow layers the vertical wavelength can be calculated to be 58 $\pm$6 km. This vertical wavelength of 58 km, together with the estimated horizontal wavelength between 1700-2500 km, results, in a wave period between 4 and 6 hours using the gravity wave dispersion relation. This result is consistent with the data shown in the Figures. With this vertical wavelength and period the recorded wind amplitude using the FPS is only attenuated by 10%.

With the good agreement between the meteor radar and the FPS it is possible to obtain more insight into the wave characteristics by looking at the meteor radar measurements during those nights. The meteor radar has not only height information about the meteor events but also information about the distance at ground level (horizontal distance) between the meteor and the radar home site. With this additional information it should be possible to measure the wind distribution at airglow heights over a ground distance of about 600 km. However, the detected meteors are not equally distributed over the ground range and show a Gaussian distribution with a peak at about 180 km distance to both sides of the radar. The width at half maximum of this distribution is about 120 km. The northern sampling volume typically gives fewer meteors due to a geometric effect. An additional difficulty arises due to the number density of meteors showing a diurnal variation, with an

increase of meteor events during the morning hours and a maximum at about 6 am LT. At 6 pm LT considerably fewer events are recorded. It is therefore likely that only in the early morning hours enough meteor events occur to provide statistically meaningful results which can be used to find signatures of long gravity waves in the meteor radar data. Figure 7.20 shows the raw meteor radar data for 12 May, 1997 recorded around 16:30 UT. This hour was chosen as it has relatively many meteor radar echoes and the airglow data in the southern sampling volume exhibits a slope change in the wind speed. In Figure 7.20 the data points are spread over a wide range of wind speeds due to the instantaneous nature of the meteor radar sampling which, in contrast to the FPS detects small scale wave motion and turbulence.

The OI airglow height was determined to be 103 km (see above) and only meteor data within $\pm$ 5 km of this height were included in the data analysis. This will, unfortunately, reduce the number of data points available for subsequent fitting. Even fewer data points remain considering that the data in Figure 7.20 are from a time interval of one hour. This interval is much too long to average over the meteor winds as the wave events being considered here have periods in the range of about 5 hours. That means, that during one hour the wave will have changed its position by a significant amount through the sampling volume, and measurements made at the beginning of the hour could sample a substantially different wind speed distribution when compared to measurements made at the end of that hour. It is therefore necessary to reduce the length of the time interval. With the remaining few data points, particularly in the northern sampling volume, no confident fitting is possible as the number of points is too sparse. However, an examination of the southern sampling volume with just three points per time interval of 15 minutes reveals a marked trend (see bottom panel Figure 7.20). In the first time interval the slope built by those points is negative. Positive in the

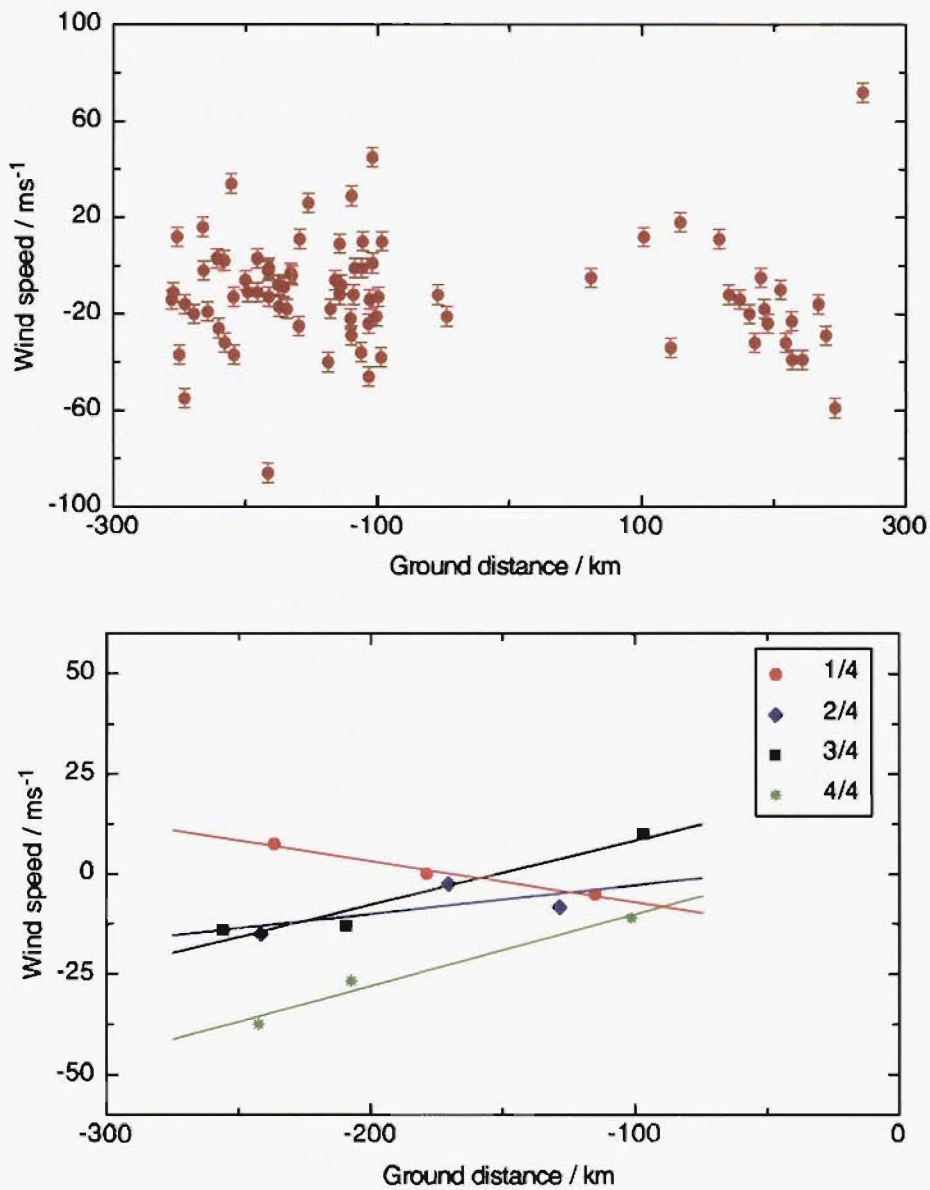

igure 7.20: The raw meteor radar wind data (top panel) over ground range for ıe 12 May 1997 in the hour around 16:30 UT. The bottom panel shows the meteor ıdar data (from the southern radar beam only) averaged into 1/4 hourly intervals rating at 16:00 UT. The data is also averaged in distance from the home site sing 75 km wide bins. The straight lines fitted to these data points indicate the ıange of the slope of the wind profile over ground range with time.

next time interval with a shallow slope which gets steeper over the next 30 minutes. This may be interpreted as the signature of a wave that travels through the radar sampling volume. This behavior is consistent with the slope change seen in the wind measurements recorded with the FPS for this time interval (see Figure 7.17 top panel).

The example data presented here show that the FPS is able to detect long wavelength gravity waves in the mesopause, lower thermosphere region by determining the difference in the wind speed findings of the opposite sampling volumes of the Fabry-Perot spectrometer in the atomic oxygen and the hydroxyl layer. In the example data presented here the vertical wavelength of a gravity wave was measured to be 58 $\pm$ 6km. The amplitude of this rather long gravity wave is only slightly attenuated (about 10%) by the mechanism decribed in 7.3. The waves are therefore readily detected by the instrument. The horizontal wavelength of this long gravity wave event could be estimated to be in the range of 1700 to 2500 km with a period between 4 and 6 hours. The retrieved parameters for this example gravity wave event are consistent with calculations using the gravity wave dispersion relation.

The meteor radar data is too sparse, especially for the northward pointing beam, to obtain data which enable the direct determination of the horizontal wave length of those gravity waves in the example. However, the meteor radar data showed a slope change of the wind speed profile over ground range with time. This result is consistent with the data measured by the Fabry-Perot spectrometer. It appears worthwhile in the future to investigate the meteor radar data during the high meteor flux in the early morning hours and look for gravity wave signatures in the wind data over the ground range.

7.7 Conclusion

Although the comparison of the meteor radar data and the Fabry-Perot spectrometer data revealed a very good agreement (see Chapter 6) the differences in the variances between both data sets raised the question of whether this is due to random noise or system differences between the instruments. Even considering that the sampling volumes are distinct the variability of the data sets should have been about the same assuming both instruments measure the same kind of quantity. Thus differences observed must originate from the differences in the sampling behaviour of the instruments employed. The Fabry-Perot spectrometer samples an airglow layer with a width of its emission profile of about 10 km at half maximum and integrates the airglow of up to 10 minutes. The meteor radar measures instantaneously in a fraction of a second and in the very confined volume of a meteor trail. These differences can not be overcome just by averaging the meteor radar wind as the meteor events are sporadic and not continuous in space and time. Instead the exact influence of the airglow layer width and the integration time of the Fabry-Perot spectrometer on the detectability of the wave motion in the atmosphere has to be taken into account.

In 7.3 the influence of the airglow layer width on the detectability of vertical waves was described. It was shown that waves with vertical wavelength similar to the FWHM of the airglow layer emission profile experience a strong attenuation of the detected amplitude since the instrument averages over the wind in the airglow layer. Allowing for the fact that the waves are likely to move through the layer the integration time of the instrument will also influence the detected wave amplitude. It was found that waves which travel $n\pi$ (n=1,2,3,...) radians within the integration time are not detectable by the Fabry-Perot spectrometer. The detected amplitude of waves traveling faster

than π radians within the integration time are strongly attenuated even for phase speed others than $n\pi$. The conclusion is that only the long period waves with vertical wavelength $\gg$ FWHM of the airglow emission height profile can be detected without much attenuation. However, other authors (Manson et al. 1979, Vincent 1984, Meek et al. 1985, Richter et al. 1981, Senft et al. 1993) found mean vertical wavelength λ_z of about 15 km and that the most energy is transported in waves with wavelength λ_z between 10 and 20 km. This is the range of waves which will experience the strongest attenuation in the detected wave amplitudes using the Fabry-Perot spectrometer. The influence of the waves phase speed on the detected wave amplitude were found to be strongest with short period waves.

Considering the gravity wave dispersion relation and noting that most waves have a horizontal wavelength between 10 and 200 km (Meek et al. 1985, Giers et al. 1997) the following can be said: Waves with long vertical wavelength which are affected little by the spatial averaging are most likely short period (see Figure 7.12) and therefore affected the most by the temporal averaging. On the other hand, waves with short vertical wavelength are affected the most by the spatial averaging but little by the temporal averaging as they are long period.

A numerical model described in 7.4 showed that the wave filter function of the Fabry-Perot spectrometer, together with a gravity wave model based on empirical wind distribution is able to simulate the data produced by the Fabry-Perot spectrometer. This is done by simulating the averaging process employing a special averaging kernel described in 7.3. The model also satisfactorily explains the observational differences between meteor radar data and Fabry-Perot spectrometer data. This supports the results of the observational limits found in 7.3. Together, 7.3 and 7.4 show that the Fabry-Perot spectrometer which samples airglow layers with a full width of about 10 km

at half height is unable to record that part of the gravity wave spectrum which carries the most energy in the mesopause, lower thermosphere region. This is a similar result to that of Gibson-Wilde et al. (1996) in their analysis of the detection of gravity waves in sodium lidar data.

In 7.5 the effect of wind shear in the airglow layer on the recorded temperature using a Fabry-Perot spectrometer were investigated. Assuming the ubiquitous presence of gravity waves in the atmosphere it could be shown that the Fabry-Perot spectrometer over estimates the temperatures by about 1.3 K for the atomic oxygen emission. This is caused by nonhomogenous wind distribution created by gravity waves. This spreads the recorded spectral emission profiles, originating from different parts of the layer, in the recorded spectrum resulting in a broader superposition of those profiles. This broadened profile will result as an apparent temperature increase.

From this discussion it follows that the Fabry-Perot spectrometer can not detect short gravity waves as described above. However, it can detect very long horizontal gravity waves. Signatures of those waves were presented in 7.6 and are observable during many nights. These waves can be detected through the wind differences they produce in two opposite sampling volumes of the Fabry-Perot spectrometer (eg the northern and southern sampling volume).

With just two horizontal sampling volumes and two airglow layers the wave parameters could not be exactly determined. However, a good estimate of the vertical and horizontal wavelength and the period was possible based on the know parameters of the experimental setup.

It was hoped that the meteor radar data would allow to obtain a higher horizontal resolution as it records meteors from up to 350 km horizontal distance north and south of the home site, however, the data were too sparse

to allow for a more detailed wave parameter determination. Only in the early morning hours, where the temporal meteor density is higher, were the number of data points sufficient to observe a phase change of the wave. This phase change was consistent with the that observed in the FPS data. An increase in the number of detected meteor events would improve the overall resolution of the meteor radar and therefore enhance the resolution over ground range. This is, however, not easily achievable as the present instrument is already detecting meteors as small as a few micro meters.

In summary, the Fabry-Perot spectrometer is able to detect long horizontal gravity waves. The detectability of these waves is enhanced by the fact that the FPS can not detect the more frequent short gravity waves. These short gravity waves would probably make the data so strongly fluctuating that the long horizontal gravity waves were not easily detectable. This can be seen in the averageing required of the meteor radar data. Increasing the number of sampling volumes by modifying the FPS would enhance the horizontal resolution, which would enable to determine the wave parameters more accurately.

Chapter 8

Conclusions

8.1 Wind Comparison

The results of the wind comparison using three independent measurement techniques can be summarized as follows: The meteor radar and the Fabry-Perot spectrometer agree in their wind findings remarkably well most of the time and appear to obtain similar results. The medium frequency radar winds do not compare as well with the results of the other two methods.

Reasons for this can be found in the different sampling volume, the medium frequency radar samples directly overhead while the meteor radar samples to the north and south from the home site. The bad signal to noise ratio of the medium frequency radar during the night is undoubtly another reason for the rather poor comparison of the night-time winds. However, during the daytime the meteor radar and the medium frequency radar data show a good agreement on some days. A better agreement can surely be expected when averaging over a longer time period.

Differences in the correlation coefficients between some nights could have cause in different gravity wave activities during those nights. As described in Chapter 7 the Fabry-Perot spectrometer is lowpass filtering the air motion in the airglow layer and is therefore unable to detect small scale waves such as gravity waves. Low gravity wave activity, leading to only weak small-scale disturbances of the mean flow, would decrease the variance of the meteor radar data. The wind data measured by Fabry-Perot spectrometer would smoothly follow the semidiurnal tide. An increase of the gravity wave activity would on the other hand increase the variance of the meteor radar data but would have very little effect on the Fabry-Perot spectrometer data, resulting in a decreased correlation between the two data sets. However, Figures 6.10 to 6.13 show that during the nights with low gravity wave activity both methods detect the same overall air motion on an hourly mean basis.

The heights of the airglow layers derived from the height information of the meteor radar by correlating the wind data of meteor radar and Fabry-Perot spectrometer are higher than the typical peak height quoted in the literature, howevere, these heights are within the range of peak heights mentioned by (Baker & Stair 1988). Not knowing the correct airglow emission distributions with height for our observations, and using the O'Brien profile as a proxy for them, can easily lead to some discrepancy in the heights reported here and the peak heights reported by direct measurements (Baker & Stair 1988, Hernandez et al. 1995).

The variations in emission height during the year is shown in Figure 6.14. The highlight of this figure is the rather large variation in the height of the OH emission, when compared with the rather constant OI emission height. Unless there are profound changes in the OH airglow layer profile throughout the year, the observed 9 km height change of this OH emission during the year indicates a change in the height at which this OH emission occurs. Other

evidence (She & VonZahn 1998) shows that the height of the mesopause changes dramatically during the year. During the winter She and VonZahn have found the height of the mesopause is near 100 km and near 88 km during the summer, which is in rather good agreement with the observed height changes for the OH shown in Figure 6.14, implying a close relationship between the height of the mesopause and the OH emission layer height. This height variability will have an impact on the photochemistry of the OH molecule (see Section 2.3) as the production rate of OH depends on the diffusion of atomic oxygen or ozone from the thermosphere above. A lower altitude will also increase the quenching rate of the emission as the density of possible quenchers will increase and the mean free path length decreases.

8.2 Gravity Wave Detectability

The differences in the variances between meteor radar data and the Fabry-Perot spectrometer data raised the question of whether this is due to random noise or system differences between the instruments. Assuming both instruments measure the same kind of quantity the variability of the data sets should have been about the same. Thus differences observed must originate from the differences in the sampling behaviour of the instruments employed. The meteor radar measures instantaneously in a fraction of a second and in the very confined volume of a meteor trail. The Fabry-Perot spectrometer samples an airglow layer with a width of its emission profile of about 10 km at half maximum and integrates the airglow for up to 10 minutes. These differences can not be overcome just by averaging the meteor radar wind as the meteor events are sporadic and not continuous in space and time. Instead the exact influence of the airglow layer width and the integration time of the Fabry-Perot spectrometer on the detectability of the wave motion in

the atmosphere has to be taken into account.

In 7.3 the influence of the airglow layer width on the detectability of vertical wave was described. It was shown that waves with vertical wavelength similar to the FWHM of the airglow layer emission profile experience a strong attenuation of the detected amplitude since the instrument averages over the wind in the airglow layer. Allowing for the fact that the waves are likely to move through the layer the integration time of the instrument will also influence the detected wave amplitude. It was found that waves which travel $n\pi$ (n=1,2,3,...) radians within the integration time are not detectable by the Fabry-Perot spectrometer. The detected amplitude of waves traveling faster than π radians within the integration time are strongly attenuated even for phase speed others than $n\pi$. The conclusion is that only the long period waves with vertical wavelength $\gg$ FWHM of the airglow emission height profile can be detected without much attenuation. However, other authors (Manson et al. 1979, Vincent 1984, Meek et al. 1985, Richter et al. 1981, Senft et al. 1993) found mean vertical wavelength λ_z of about 15 km and that the most energy is transported in waves with wavelength λ_z between 10 and 20 km. This is the range of waves which will experience the strongest attenuation in the detected wave amplitudes using the Fabry-Perot spectrometer. The influence of the waves' phase speed on the detected wave amplitude were found to be strongest with short period waves.

Considering the gravity wave dispersion relation and noting that most waves have a horizontal wavelength between 10 and 200 km (Meek et al. 1985, Giers et al. 1997) the following can be said: Waves with long vertical wavelength which are affected little by the spatial averaging are most likely short period (see Figure 7.12) and therefore affected the most by the temporal averaging. On the other hand, waves with short vertical wavelength are affected the most by the spatial averaging but little by the temporal averaging as they

are long period.

A computer model described in 7.4 showed that the wave filter function of the Fabry-Perot spectrometer, together with a gravity wave model based on empirical wind distribution is able to simulate the data produced by the Fabry-Perot spectrometer. The model supports the results of the observational limits found in 7.3. Together, 7.3 and 7.4 show that the Fabry-Perot spectrometer which samples airglow layers with a full width of about 10 km at half height is unable to record that part of the gravity wave spectrum which carries the most energy in the mesopause, lower thermosphere region.

In 7.5 the effect of wind shear in the airglow layer on the recorded temperature using a Fabry-Perot spectrometer were investigated. Assuming the ubiquitous presence of gravity waves in the atmosphere it could be shown that the Fabry-Perot spectrometer over estimates the temperatures by 1.3 K for the atomic oxygen emission. This is caused by nonhomogenous wind distribution created by gravity waves. This spreads the recorded spectral emission profiles, originating from different parts of the layer, in the recorded spectrum resulting in a broader superposition of those profiles. This broadened profile will result as an apparent temperature increase.

From this discussion it follows that the Fabry-Perot spectrometer can not detect short gravity waves as described above. However, it can detect very long horizontal gravity waves. Signatures of those waves were presented in 7.6 and are observable during many nights. These waves can be detected through the wind differences they produce in two opposite sampling volumes of the Fabry-Perot spectrometer (eg the northern and southern sampling volume).

With just two horizontal sampling volumes and two airglow layers the wave parameters could not be exactly determined. However, a good estimate of

the vertical and horizontal wavelength and the period was possible based on the know parameters of the experimental setup.

It was hoped that the meteor radar data would allow a higher horizontal resolution to be obtain as it records meteors from up to 350 km horizontal distance north and south of the home site, however, the data were too sparse to allow for a more detailed wave parameter determination. Only in the early morning hours, where the temporal meteor density is higher, were the number of data points sufficient to observe a phase change of the wave. This phase change was consistent with the that observed in the FPS data. An increase in the number of detected meteor events would improve the overall resolution of the meteor radar and therefore enhance the resolution over ground range. This is, however, not easily achievable as the present instrument is already detecting meteors as small as a few micro meters.

In summary, the Fabry-Perot spectrometer is able to detect long horizontal gravity waves. The detectability of these waves is enhanced by the fact that the FPS can not detect the more frequent short gravity waves. These short gravity waves would probably make the data so strongly fluctuating that the long horizontal gravity waves would not be easily detectable. This can be seen in the averageing required of the meteor radar data. Increasing the number of sampling volumes by modifying the FPS would enhance the horizontal resolution, which would enable the wave parameters to be determined more accurately.

8.3 Summary

The night-time meteor radar winds and the winds derived from the Fabry-Perot spectrometer airglow measurements show good agreement with corre-

lation coefficients of up to 0.95. However, nights with correlation coefficients less than 0.70 can be found in the data set encompassing May 1997 to April 1998. This discrepancy in the result can be understood when considering the different nature of the sampling technique of both instruments employed.

The height of the airglow layers was calculated using a correlation and phase matching method involving the meteor radar data and the Fabry-Perot spectrometer data. The calculation of the monthly averaged heights of the atomic oxygen layer and the hydroxyl layer revealed a rather constant height of the OI layer while the OH layer showed an annual variation of 9 km with a minimum in early summer.

Chapter 7 describes that in contrast with the instantaneous and discrete sampling of the meteor radar the Fabry-Perot spectrometer integrates not only over time but also over the airglow height profile. This integration leads to a lowpass filtering of wave motions which affects the detectability of small scale waves such as gravity waves. As a result: The Fabry-Perot spectrometer is therefore unable to record that part of the gravity wave spectrum which carries the most energy in the mesopause, lower thermosphere region.

With the knowledge of the lowpass filter the data sets were scanned for signatures of gravity waves with long vertical wavelength. Such signatures were found during many nights. With the example data presented here a vertical wavelength of about 58 km and horzontal wavelength in the range of about 2000 km were found. Hence, the Fabry-Perot spectrometer can detect gravity waves with long vertical and horizontal waveslengths. Juging from the available data set these long gravity waves appear to be common events. The attempt to gain more information about the horizontal wave structure using the meteor radar ground range information was unsuccessful as the available data were to sparse. In summary, the Fabry-Perot spectrometer is

able to detect long horizontal gravity waves. The detectability of these waves is enhanced by the fact that the FPS can not detect the more frequent short gravity waves.

Bibliography

Andrews, D. G., Holton, J. R. & Leovy, C. B. (1987), *Middle Atmosphere Dynamics*, Academic Press Inc.

Armstrong, E. B. (1968), 'Variations in the width of the OI λ 5577 line in the night airglow', *Planet. Space Sci.* **16**, 211.

Babcock, H. D. (1923), 'A study of the green auroral line by the interference method', *Astrophys. J.* **57**, 209.

Baggaley, J. W. & Bennet, R. G. T. (1996), 'The meteor orbit radar facility AMOR: Recent developments', *Phys. Chem. Dyn. Interplanet. Dust* **104**, 65.

Baggaley, W. J., Bennett, R. G. T., Steel, D. I. & Taylor, A. D. (1994), 'The advanced meteor orbit radar facility: AMOR', *Q. J. R. astr. Soc.* **35**, 293.

Baker, D. J. (1978), *Studies of atmospheric infrared emissions*, Rep. AFGL-TR-78-0251, Air Force Geophysics Lab. Bedford, Massachusetts.

Baker, D. J. & Stair, A. T. (1988), 'Rocket measurements of the altitude distributions of the hydroxyl airglow', *Physica Scripta* **37**, 611.

Balsley, B. B. & Carter, D. A. (1982), 'The spectrum of atmospheric velocity fluctuations at 8 and 86 km', *Geophys. res. Lett.* **9**, 465.

Balsley, B. B. & Garello, R. (1985), 'The effect of El Chicon on wind variability in the troposphere, stratosphere, and mesosphere over Alaska', *Geophys. Res. Lett.* **12**, 581–584.

Barnes, S. L. (1964), 'A technique for maximizing details in numerical weather map analysis', *J. App. Met.* **3**, 396–409.

Bates, D. R. (1982), 'Airglow and auroras', *Appl. Atom. Coll. Phys.* **1**, 49.

Bates, D. R. & Nicolet, M. (1950), 'The photochemistry of atmospheric water vapor', *J Geophys. Res.* **55**, 301.

Born, M. & Wolf, E. (1959), *Principles of Optics*, Pergamon, New York.

Briggs, B. (1984), The analysis of spaced sensor records by correlation techniques, *in* R. Vincent, ed., 'Ground-Based Techniques', Vol. 13 of *Handbook for MAP*, SCOSTEP, pp. 166–186.

Briggs, B. H., Phillips, G. J. & Shinn, D. H. (1950), 'The analysis of observations on spaced receivers of the fading of radio signals', *Proc. Phys. Soc.* **63**, 106.

Brown, G. M. & Chapman, J. W. (1972), 'Full correlation ionospheric drift analysis for a general observing triangle', *Ann. Geophys.* **28**, 349–356.

Chamberlain, J. W. (1961), *Physics of the Aurora and Airglow*, Academic Press.

Chapman, S. & Lindzen, R. S. (1970), *Atmospheric Tides - Thermal and Gravitational*, D. Reidel, Dordecht, Holland.

Conner, J., Smith, R. & Hernandez, G. (1993), 'Techniques for deriving Doppler temperatures from multiple-line Fabry-Perot profiles: an analysis', *Appl. Opt.* **32**, 4437.

Demtröder, W. (1991), *Laserspectroskopie*, Springer-Verlag.

Dewan, E. M. & Good, R. E. (1986), 'Saturation and the "universal" spectrum for vertical profiles of horizontal scalar winds in the atmosphere', *J. Geophys. Res.* **91**, 2742.

Fabry, C. & Perot, P. (1897), 'Sur les franges des lames minces argentees et leur application a la mesure de petites epasseurs d'air', *Ann. Chem. Phys.* **12**, 459.

Forbes, J. M. (1982), 'Atmospheric tides 2. the solar and lunar semidiurnal components', *J. Geophys. Res.* **87**, 5241.

Fraser, G. J. (1965), 'The measurement of atmospheric winds at altitudes of 64-120 km using ground-based radio equipment', *J. Atmos. Sci.* **22**, 217.

Fraser, G. J. (1968), 'Seasonal variation of southern hemisphere mid-latitude winds at altitudes of 70-100 km', *J. Atmos. Terr. Phys.* **30**, 707.

Fraser, G. J. (1984), 'Partial-reflection spaced antenna wind measurements', *MAP* **13**, 233.

Frederick, J. E. (1979), 'Influence of gravity wave activity on lower thermospheric photochemistry and composition', *Planet Space Sci.* **27**, 1469.

Freund, J. T. & Jacka, F. (1979), 'Structure in the λ 557.7 nm [OI] airglow', *J. Terr. and Atmos. Physics* **27**, 25.

Gardner, C. S. (1994), 'Diffusive filtering theory of gravity wave spectra in the atmosphere', *J. Geophys. Res.* **99**, 20601.

Gardner, C. S. (1995), Scale-independent diffusive filtering theory of gravity wave spectra in the atmosphere, *in* R. M. Johnson & T. L. Killeen, eds,

'The Upper Atmosphere and Lower Thermosphere: A Review of Experiment and Theory, Geophys. Monog. Ser.', Vol. 87, AGU, Washigton, D. C., p. 153.

Gardner, C. S. (1996), 'Testing theories of atmospheric gravity wave saturation and dissipation', *J. Atmos. Terr. Phys.* **58**, 1575.

Gardner, C. S. (1998), 'Theoretical models for gravity wave horizontal wavenumber spectra: Effects of wave field anisotropies', *J. Geophys. Res.* **103**, 6438.

Gardner, C. S. & Shelton, J. D. (1985), 'Density response of neutral atmospheric layers to gravity wave perturbation', *J. Geophys. Res.* **90**, 1745.

Gardner, C. S. & Taylor, M. J. (1998), 'Observational limits for lidar, radar, and airglow imager measurements of gravity wave parameters', *J. Geophys. Res.* **103**, 6427.

Gerbier, N. & Berenger, M. (1961), 'Experimental studies of lee waves in the french alps', *Quart. J. Roy. Met. Soc.* **87**, 13.

Giacomo, P. (1952), 'Methode directe de mesure des characteristique d'un systeme interferential de fabry-perot', *Compt. Rend.* **235**, 1627.

Gibson-Wilde, D. E., Reid, I. M., Eckermann, S. D. & Vincent, R. A. (1996), 'Simulation of lidar measurements of gravity waves in the mesosphere', *J. Geophys. Res.* **101**, 9509.

Giers, D. H., Sahai, Y., Cogger, L. L. & Ryan, E. H. (1997), 'Occurrence characteristics of mesospheric gravity waves at 51°N', *J. Atmos. Sol. Terr. Phys.* **59**, 1197.

Gradshteyn, I. S. & Ryzhik, I. M. (1965), *Tables of Integrals, Series, and Products*, Academic Press.

Hargreaves, J. K. (1992), *The Solar Terrestrical Environment*, Cambridge Atmospheric and Space Science Series 5.

Hatfield, R., Tuan, T. F. & Silverman, S. M. (1981), 'On the effects of atmospheric gravity waves on profiles of H, O_3, and OH emission', *J. Geophys. Res.* **86**, 2429.

Hays, P. & Roble, R. (1971), 'A technique for recovering Doppler line profiles from Fabry-Perot interferometer fringes of very low intensity', *Appl. Opt.* **10**, 193.

Hernandez, G. (1978*a*), 'Analytical description of a Fabry-Perot spectrometer. iv. signal noise limitations in data retrieval: winds, temperatures, and emission rate', *Appl. Opt.* **17**, 2967.

Hernandez, G. (1978*b*), 'Piezoelectric scanning of Fabry-Perot spectrometers: Nonlinearities', *Appl. Opt.* **17**, 3088.

Hernandez, G. (1980), 'Measurement of thermospheric temperature and winds by remote Fabry-Perot spectrometry', *Opt. Eng.* **19**, 518.

Hernandez, G. (1986), *Fabry-Perot Interferometers*, Cambridge University Press.

Hernandez, G. (1988), 'Optical measurements of winds and kinetic temperatures in the upper atmosphere', *COSPAR Adv. Space Res.* **8**, 149.

Hernandez, G. & Smith, R. W. (1995), 'Winds and vertical wavelength deduced from the ground-based measurement of doppler shifts of the $O_2(b^1\Sigma_g^+ - X^3\Sigma_g^-)$, OI($^1D_2 - {}^1S_0$), and the $X^2\Pi$ OH(6−2) band $P_1(2)_{c,d}$ line emissions in the midlatitude upper middle atmosphere', *Geophys. Res. Lett.* **22**, 369.

Hernandez, G., Wiens, R., Lowe, R. P., Shepherd, G. G., Fraser, G. J., Smith, R. W., LeBlanc, L. M. & Clark, M. (1995), 'Optical determination of the vertical wavelength of propagating 12-hour period upper atmosphere oscillations', *Geophys. Res. Lett.* **22**, 2389.

Hines, C. O. (1960), 'Internal atmospheric gravity waves at ionospheric heights', *Can. J. Phys.* **38**, 1441.

Hines, C. O. (1991), 'The saturation of gravity waves in the middle atmosphere. part II: Development of Doppler-Spread Theory', *J. Atmos. Sci.* **48**, 1360.

Hines, C. O. & Tarasick, D. W. (1987), 'On the detection und utilization of gravity waves in airglow studies', *Planet Space Sci.* **35**, 851.

Holton, J. (1992), *An Introduction to dynamic meteorology*, Vol. 48 of *International Geophysics Series*, 3rd edn, Academic Press.

Jacka, F. (1984), 'Application of Fabry-Perot spectrometers for measurement of the upper atmosphere temperatures and winds', *Handbook of Middle Atmosphere Program* **13**, 19.

Kaye, J. A. (1988), 'On the possible role of the reaction $O + HO_2 \rightarrow OH + O_2$ in OH airglow', *J. Geophys. Res.* **93**, 285.

Lomb, N. (1976), 'Least-squares frequency analysis of unequally spaced data', *Ap. Space. Sci.* **39**, 447–462.

Manney, G. L., Nathan, T. R. & Stanford, J. L. (1989), 'Barotropic instability of basic states with a realistic jet and a wave', *J. Atmos. Sci.* .

Manson, A. H., Meek, C. E., Massebeuf, M., Fellous, J. L., Elford, W. G., Vincent, R. A., Craig, R. L., Roper, R. G., Avery, S., Balsley, B. B., Fraser, G. J., Smith, M. J., Clark, R. R., Kato, S., Tsuda, T. & Ebel, A.

(1985), 'Mean winds of the mesosphere and lower thermosphere (60-100 km): A global distribution from radar systems (MF, meteor, VHF)', *Adv. Space Res.* **5**, 135–144.

Manson, A. H., Meek, C. E. & Stening, R. J. (1979), 'The role of atmospheric waves (1.5 h - 10 days) in the dynamics of the mesosphere and lower thermosphere at saskatoon (52° n, 107°w) during four seasons of 1976', *J. Atmos. Terr. Physics* **41**, 325.

Marquardt, D. W. (1963), 'An algorithm for least-squares estimation of non-linear parameters', *J. Soc. Indust. Appl. Math.* **11**, 431.

Marsh, S. (1999), Wind measurements using the Meteor Radar, PhD thesis, University of Canterbury, New Zealand, in preparation.

McDade, I. C. (1991), 'The altitude dependence of the oh($x^2\pi$) vibrational distribution in the nightglow: some model expectations', *Planet. Space Sci.* **39**, 1049.

McEvan, M. J. & Phillips, L. F. (1975), *Chemistry of the Atmosphere*, Edward Arnold.

Meek, C. E., Reid, I. M. & Manson, A. H. (1985), 'Observations of mesospheric wind velocities: 1. gravity wave horizontal scales and phase velocities determined from spaced wind observations', *Rad. Sci.* **20**, 1363–1382.

Meinel, B. B. (1950), 'Oh emission bands in the spectrum of the nightglow', *Planet. Space Sci.* **111**, 555.

Meriwether, J. W. (1989), 'A review of the photochemistry of selected nichtglow emission from the mesopause', *J. Geophys. Res.* **94**, 14692.

Muller, H. G. (1966), 'Atmospheric tides in the meteor zone', *Planet. Space Sci.* **14**, 1253.

Nicolet, M. (1989), 'Aeronomic chemistry of ozone', *Planet. Space Sci.* **37**, 1621.

Noxon, J. F. (1978), 'Effect of internal gravity waves upon airglow temperatures', *Geophys. Res. Lett.* **5**, 25.

O'Brien, B. J., Allum, F. R. & Goldwire, H. C. (1965), 'Rocket measurements of midlatitude airglow and particle precipitation', *J. Geophys. Res.* **70**, 161.

Peterson, A. W. & Kieffaber, L. M. (1973), 'Infrared photography of OH airglow structures', *Nature* **242**, 711.

Petitdidier, M. & Teitelbaum, H. (1979), 'O(^{1}s) excitation mechanism ans atmospheric tides', *Planet. Space Sci.* **27**, 1409.

Phillips, A., Manson, A. H., Meek, C. H. & Llewellyn, E. J. (1994), 'A long-term comparision of middle atmosphere winds measured at Saskatoon (52N 107W) by a medium-frequency radar and a Fabry-Perot interferometer', *J. Geophys. Res.* **99(D6)**, 12923.

Plagmann, M., Marsh, S., Baggaley, W., Bennett, R., Deutsch, K., Fraser, G., Hernandez, G., Lawrence, B. N., Plank, G. & Smith, R. (1998), 'Annual variation of airglow heights derived from wind measurements', *Geophys. Res. Lett.* **25**, 4457–4460.

Price, G. D., Smith, R. W. & Hernandez, G. (1995), 'Simultaneous measurements of large vertical winds in the upper and lower thermosphere', *J. Atmos. Terr. Phys.* **57**, 631.

Richter, E. S., Rowlett, J. R., Gardner, C. S. & Sechrist, C. F. (1981), 'Lidar observations of mesopheric sodium layer over urbana, illinois', *J. Atmos. Terr. Phys* **43**, 327.

Rogers, J. W., Murphy, R. E., Stair, A. T., Ulwich, J. C., Baker, D. J. & Jensen, L. L. (1973), 'Radiometric measurements of OH in the auroral zone', *J. Geophys. Res.* **78**, 7023.

Salby, M. L. (1996), *Fundamentals of Atmospheric Physics*, Academic Press Inc.

Senft, D. C., Hostetler, C. A. & Gardner, C. S. (1993), 'Characteristics of gravity wave activity and spectra in the upper stratosphere and upper mesosphere at Arecibo during early April 1989', *J. Atmos. Terr. Phys.* **55**, 425.

She, C. Y. & VonZahn, U. (1998), 'Concept of a two-level mesopause - support through new Lidar observations', *J. Geophys. Res.* **103**, 5855.

Shepherd, G. G., McLandress, C. & Solheim, B. H. (1995), 'Tidal influence on o(^{1}s) airglow emission rate distributions at the geographic equator as observed by WINDII', *Geophys. Res. Lett.* **22**, 275.

Sivjee, G. G. (1992), 'Airglow hydroxyl emissions', *Planet. Space Sci.* **40**, 235.

Smith, M. J. (1981), Upper Atmosphere Circulation and Wave Motion, PhD thesis, University of Canterbury, New Zealand.

Smith, S. A., Fritts, D. C. & VanZandt, T. E. (1987), 'Evidence for a saturated spectrum of atmospheric gravity waves', *J. Atmos. Sci.* **44**, 1404–1410.

Smith, S. M. (1996), Optical and Radar Wind Comparision in the Mesosphere and Lower Thermosphere, PhD thesis, University of Canterbury, New Zealand.

Swenson, G. R. & Gardner, C. S. (1998), 'Analytical models for the responses of mesospheric oh* and na layers to atmospheric gravity waves', *J. Geophys.Res.* **103**, 6237.

Takahashi, H., Clemesha, B. R. & Batista, P. P. (1995), 'Predominant semi-annual oscillation of the upper mesospheric airglow intensities and temperatures in the equatorial region', *J. Atmos. Terr. Phys.* **57**, 407.

Tarasick, D. W. & Hines, C. O. (1990), 'The observable effects of gravity waves on airglow emissions', *Planet. Space Sci.* **35**, 1105.

Taylor, M. J. & Garcia, F. J. (1995), 'A two-dimensional spectral analysis of short period gravity waves imaged in the OI(557.7 nm) and near infra red OH nightglow emissions over Arecibo, Puerto Rico', *Geophys. Res. Lett.* **22**, 2473.

Taylor, M. J. & Hapgood, M. A. (1988), 'Identification of a thunderstorm as a source of short period gravity waves in the upper atmospheric nightglow emissions', *Planet. Space Sci.* **36**, 975.

Texier, H. L., Solomon, S. & Garcia, R. R. (1987), 'Seasonal variability of the OH Meinel bands', *Planet. Space Sci.* **35**, 977.

Thomas, R. J. (1981), 'Analyses of atomic oxygen, the green line, and the Herzberg bands in the lower thermosphere', *J. Geophys. Res.* **86**, 206.

Thomas, R. J. & Young, R. A. (1981), 'Measurements of atomic oxygen and related airglows in the lower thermosphere', *J. Geophys. Res.* **86**, 7389.

Vincent, R. A. (1984), 'Gravity-wave motions in the mesosphere', *J. Atmos. Terr. Phys.* **46**, 119–128.

Walterscheid, R. L. & Schubert, G. (1987), 'A dynamical-chemical model of tidally driven fluctuations in the OH nightglow', *J. Geophys. Res.* **92**, 8775.

Witt, G., Stegman, J., Solheim, B. H. & Llewellyn, E. J. (1979), 'A measurement of the $O_2(b^1\Sigma^+g$ - $X^3\Sigma_g^-)$ atmospheric band and the OI(^{1}S) green line in the nightglow', *Planet. Space Sci.* **27**, 341.

Acknowledgements

There are many people who deserve my thanks for their help during this project. My sincere thanks go to my supervisors Drs Grahame Fraser and Bryan Lawrence. Without the sharing of their understanding of physics and their encouragement during the periods of disillusionment this project would have been impossible.

The data from the Fabry-Perot spectrometer at Mt. John, owned by G. Hernandez and Dr. R. W. Smith, was kindly made available in exchange for the maintenance of the instrument.

I thank my fellow PhD students, the other two residents of the "Foreign Ghetto", Andy Reisinger and John Grant for their help on numerous occasions and for the enjoyable times we spent together. I value the discussions we had on matters of science and more importantly on matters of life, and last but not least I value their manuscript reading and suggestions.

There is also Steven Marsh who deserves my thanks for his support in introducing me to the meteor radar technique and for supplying me with his meteor radar wind data. I also would not like to miss the hours, days, weeks we sat together in front of the computer monitor diving into the world of Wavelet analysis.

Steve M. Smith receives my thanks for explaining to me the Fabry-Perot spectrometer and how to maintain this sensitive instrument.

The technicians and superintendents of Mt. John must not be forgotten. I thank Mike Clark, Allan Gilmore, and Steven Barlow for looking after the Fabry-Perot spectrometer "Doris" and "Rosie" and the grating spectrometer "Ebert" during the times of my absence.

I am also indebted to my parents and my brother for their encouragement to go to New Zealand and their support during the years of this project.

I would also like to thank my partner Monika for her encouragement and support. I particularly thank her for her patience and understanding during the times of weekend and late night work. The writing of this thesis was definitely accelerated by the prospect of the arrival of our son Maurice. Therefore thanks go to him as well.